Simulations of high-order nonlinear optical spectra on polymers of three-level systems

by

Grégoire Zachary Aubert Laurier Berger-Malette

A thesis submitted in partial
fulfillment of the requirements for the
Master of Science degree in Physics

Department of Physics
Faculty of Science
University of Ottawa

Abstract

This thesis describes the computational tools that allow the simulation of polymers made up of an arbitrary number of three-level systems, the study of such systems and comparisons to experimental nonlinear optical spectra. The three-level system generator (3LSG) , is designed to automatically generate the operators that describe the system, whether it is a closed system or an open quantum system (OQS) in contact with a bath, with just a few input parameters. A user is free to specify each 3LS's energy levels and transition dipoles between said levels, site couplings between the different units of the polymer and in the case of open systems, the rates and couplings describing the different relaxation processes taking place in an OQS, using the Redfield formalism. In either cases, the 3LSG is then capable of generating the Hamiltonian H_0 describing the closed system or the Liouvillian $\mathcal{L}_0$ describing the open system from the various inputs. The Ultrafast Spectroscopy Suite (UFSS) is an open-source software suite used to perform the nonlinear optical spectroscopies simulations. It contains 4 main modules, one of which is the Hamiltonian/Liouvillian Generator (HLG), a module previously designed to model simpler two-level systems. The 3LSG is a sub-module of the HLG. The three-level system generator is used to replicate a theoretical model describing a copolymer model made of many identical pairs of squaraine monomers, where each monomer is a three-level system interacting with its neighbouring sites and a surrounding bath. The system automatically generated by the 3LSG is used, along with other spectroscopic calculation tools, to simulate high-order transient absorption (TA) spectroscopies and study the long-time behaviour of the 3^{rd}-order to 13^{th}-order excited state absorption (ESA) peaks in the TA signals. The 3LSG is used in conjunction with spectroscopic calculations tools as it was originally intented, though it may also be used by itself to study Hamiltonians and Liouvillians of electronic three-level systems.

Acknowledgements

I first thank my supervisor, Jacob Krich, for the continuous support he has provided throughout the years. Your advice and insights were always helpful, as was the feedback you constantly gave about my work. I would also like to thank Peter Rose, for your constant willingness to help, along with your invaluable knowledge of UFSS, which made this work far easier. This thesis and the work within could not have been done without both of you to assist me. I would also like to thank everyone else in the Krich group for all the support, kind words and the interesting conversations we have had in our various meetings.

Dernièrement, j'aimerais surtout remercier tous mes proches. Mes parents, pour leur support inconditionnel tout au long de mes études, pour les discussions et surtout pour leurs paroles rassurantes. Mes frères, pour leurs encouragements continus. Tous mes amis, pour m'avoir écouté (probablement trop souvent) déblatérer et partager sans cesse toutes mes frustrations de long en large. On n'accomplit rien réellement seul et je n'aurais pas pu être mieux accompagné dans cette drôle d'aventure. Merci pour tout.

Statement of Original Contributions

Chapters 1-3 are summaries of already established concepts relevant to nonlinear spectroscopies as studied in the context of this thesis, except for Sec. 3.5, which presents concepts of high-order transient absorption spectroscopies. Chapters 4 is original and not published. The project was begun in collaboration with Jacob Krich, and I performed all analytical and numerical calculations. Jacob Krich provided guidance and edited the chapter. Chapter 5 is original and not published. The project was begun in collaboration with Jacob Krich and Peter Rose, and I performed all analytical and numerical calculations. Jacob Krich provided guidance and edited the chapter.

Contents

Chapter 1

Linear and Nonlinear Optical Spectroscopies

1.1 Thesis Outline

Optical spectroscopy is the field studying the spectra emitted from and absorbed by matter as a result of its interaction with a radiation field, such as a short laser pulse or a continuous wave (CW) laser. The various techniques of optical spectroscopy can be used to understand and characterize the different physical properties of various material systems, such as atoms in the gas phase or large molecular aggregates dissolved in a solution. Optical spectroscopies can be formally separated into two main categories : linear and nonlinear.

When an electric field interacts with the system under study, the system will build-up a polarization field $\mathbf{P}(t)$ and subsequently emit a propagating electric field. Expanding this polarization field in powers of the incident fields leads to the familiar perturbation series [1–3]

$$\mathbf{P}(t) = P^{(0)}(t) + P^{(1)}(t) + P^{(2)}(t) + P^{(3)}(t) + ... \tag{1.1}$$

In this thesis, we focus on systems that are isotropic and that thus have no permanent dipole moment. This implies that even orders of the polarization in Eq. 1.1 will vanish [2] and we are then left with

$$\begin{aligned}\mathbf{P}(t) &= P^{(1)}(t) + P^{(3)}(t) + P^{(5)}(t) + P^{(7)}(t)... \\ &= P^{(1)}(t) + P_{NL}(t).\end{aligned} \tag{1.2}$$

The first-order linear polarization $P^{(1)}$ describes the linear reponse of a system subject to interaction with an incident field. It can be used to describes processes such as linear absorption or emission. The linear polarization

$P^{(1)}(t)$ contains all the information that is necessary to understand linear spectroscopy. All the additional terms contained in $P_{NL}(t)$ in Eq. 1.2 are related to the nonlinear response of the system. Those higher-order terms can be considered when the system interacts with two or more light fields, or when the linear response is not sufficient to describe the system's behaviour when interacting with a pulse, as is the case when using high-intensity radiation. Spectroscopies that rely on the measurement of a quantity directly related to the polarization field are called coherent spectroscopies and are the main spectroscopies considered in this thesis. Other examples of spectroscopies include action-detected spectroscopies, which are related to the measurement of fluorescence or photo-current [4–6] but are not covered in this work.

This thesis is divided in five chapters. Chapters 1 through 3 cover some background material on nonlinear optical spectroscopies (NLOS), while Chapters 4 and 5 represent our own contribution. The remainder of Chapter 1 covers the fundamental concepts of both linear and nonlinear spectroscopies, showing simulations of a number of popular spectroscopies. Chapter 2 provides the mathematical framework necessary to model atomic and molecular systems, using both Hamiltonian and Liouvillian formalisms, and how such models are computationally created for numerical simulations. Chapter 3 describes a general theoretical approach to calculations of spectroscopic signals, illustrating the most common approximations used within the field of NLOSs. It also describes the basic ideas of high-order spectroscopies, with the last section of Chapter 3 giving a brief overview of the Ultrafast Spectroscopy Suite (UFSS) [7], which is the open source software used to simulate all spectroscopies shown throughout this thesis. Chapter 4 describes how we can improve one of the main modules of UFSS to model and procedurally generate a larger range of molecular systems than those shown in Chapter 2, within closed and open system formalisms. Finally, Chapter 5 describes how we use this new model generator and UFSS to reproduce the theoretical model from Ref. [8], and gain insight on physical phenomena that were previously unexplained.

1.2 Linear Spectroscopies

Linear spectroscopy is the simplest coherent spectroscopy that exists. It studies the response of the system that is linearly proportional to a single incident light pulse's electric field interacting with the system, with the response being related to the linear polarization $P^{(1)}(t)$ in Eq. 1.2. Figure 1.1 shows a simplified schematic of a linear absorption spectroscopy setup using an ultrafast light pulse as a source. Linear absorption spectroscopy is one particular example of linear spectroscopy, with another example being emission spectroscopy.

Figure 1.1: Linear absorption schematic

Linear absorption spectroscopy measures the portion of the incident light that has been absorbed by a sample after passing through it. The resulting spectrum can provide information about the energy levels of the sample, whether they are electronic or vibrational in nature. Figure 1.2 shows a linear absorption spectrum obtained from a simulation of a three-level system monomer using an ultrafast pulse, where the signal is shown as both a function of time and frequency. Chapter 2 and 4 provide more details about how systems of this kind are modeled and created for computational purposes in the context of this thesis.

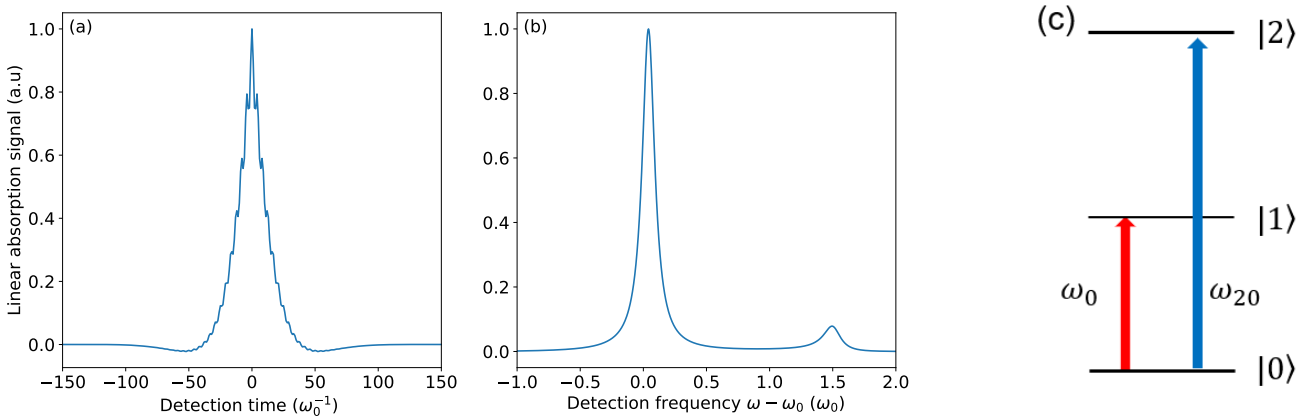

Figure 1.2: Simulated linear absorption signal of a three-level system in (a) time-domain and (b) frequency-domain. The frequency-domain signal is obtained taking the Fourier transform of the time-domain signal. Both signals are normalized such that the highest peak in each signal has unit amplitude. The system is modeled as being in contact with a bath, causing the absorption peaks in panel (b) to have a finite linewidth due to relaxation effects. Panel (c) shows an energy level diagram of the system being modeled, with the ground-state to first excited state transition frequency being ω_0, where the horizontal detection time axis on panel (a) is in units of ω_0^{-1}, and the detection frequency axis on panel (b) is in units of ω_0. Thus, the peak at $\omega - \omega_0 = 0$ on the detection frequency axis corresponds to the transition frequency precisely equal to ω_0 and we can thus attribute this peak to the $|0\rangle \rightarrow |1\rangle$ transition.

The linear absorption spectrum in Fig. 1.2 (b) above is straightforward to interpret due to the simple nature of

the system modeled in this case. Assuming, as is most often the case, that the system is initially in its ground-state, there are only two possible transitions that can occur from an interaction with a light pulse. The first transition is from the ground-state $|0\rangle$ to the singly-excited state $|1\rangle$, with a frequency $\omega_{10} = \omega_0$, which corresponds to the left peak in the absorption spectrum. The second possible transition is from $|0\rangle$ to the higher energy, doubly-excited state $|2\rangle$, with frequency ω_{20}, corresponding to the right peak in the spectrum.

In an experimental context, the samples studied either consist of a much larger number of interacting units (as opposed to the single molecule in our simulation above) or the individual units that compose the system have a more complex structure (for example, a finer electronic structure made of more levels or vibrational and rotational modes). Both of those aspects contribute to more complicated spectra. The top panel of Fig. 1.3 shows the experimental linear absorption spectrum of an $HCO_3^-(H_2O)$ compound, where multiple absorption peaks can be seen, with some of them overlapping as well.

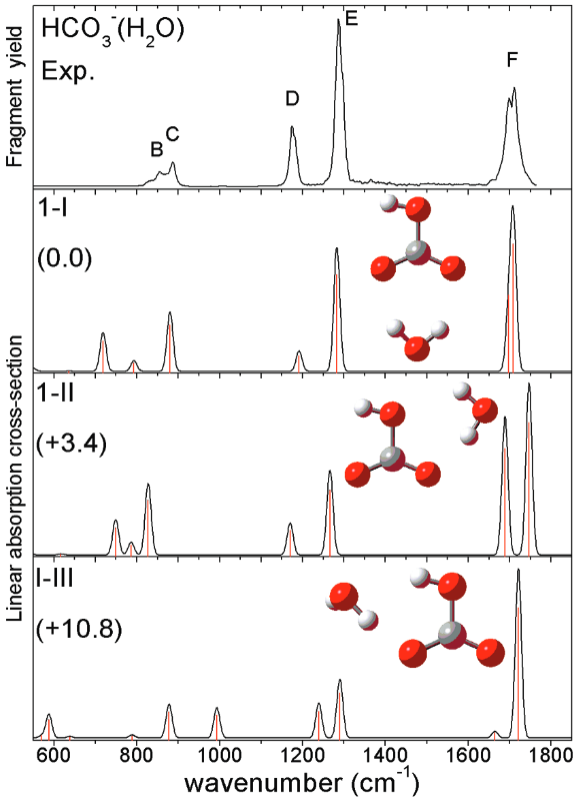

Figure 1.3: Experimental linear absorption spectrum (top panel) of $HCO_3^-(H_2O)$, and simulated linear absorption spectra of the three lowest-energy isomers making up the compound, from [9].

Linear absorption spectra, while useful for revealing the energy structure of a variety of complex systems, are ultimately only measurements of the static properties of those systems. They cannot provide any information regarding the dynamic properties of the sample, unlike nonlinear spectroscopies, which we cover in the following section.

1.3 Nonlinear Optical Spectroscopies

Ultrafast nonlinear optical spectroscopies constitute a range of techniques that allow the study of the dynamical properties of material systems. When a sample interacts with more than a single pulse, it produces a nonlinear polarization $P_{NL}(t)$. A coherently-detected NLOS using noncollinear pulses is characterized by two elements : its nonlinear order and its phase-matching condition (also called direction). The nonlinear order of a spectroscopy is defined by the nonlinear order of the polarization $P^{(n)}$ built-up by the system, which depends on the number of interactions with the incident fields. The phase-matching direction corresponds to the position of the detector with respect to the direction of propagation of the pulses.

To illustrate how we characterize a particular NLOS of our choice, let us consider an experiment with two pulses a, b, propagating in their respective directions $\mathbf{k}_a$, $\mathbf{k}_b$. The first pulse interacts twice with the sample and the second pulses interacts once and thus, the system builds a 3^{rd}-order polarization $P^{(3)}(t)$, leading to a 3^{rd}-order signal. Placing a detector in the $-\mathbf{k}_a + \mathbf{k}_a + \mathbf{k}_b$ direction leads to the measurement of the transient absorption signal (see Sec. 1.3.1). If we instead have that the first pulse interacts only once with the system and the second now interacts twice, and this time place a detector in the $+\mathbf{k}_a - 2\mathbf{k}_b$ direction, we would measure the photon-echo signal. All simulations in the following subsections below treat the incident electric field as a sum over the two different pulses a and b

$$\mathbf{E}(t) = \sum_{j=a,b} \varepsilon_j(t) + \varepsilon_j^*(t),$$

with

$$\varepsilon_j(t) = A_j(t - t_j)e^{-i(\omega_j(t-t_j)+\mathbf{k}_j\cdot\mathbf{r}+\phi_j)} \tag{1.3}$$

where $A_j(t - t_j)$ is a Gaussian envelope.

In a real spectroscopy experiment, the light pulses are in fact focused down to a particular spot size [10, 11] with a diameter of multiple wavelengths of the pulses used (usually in the 10s or 100s of μm), above the diffraction limit [3, 12]. Typically, in pump-probe experiments (such as transient absorption spectroscopy and photon-echo spectroscopy), the pump pulse has a larger focal area than the probe pulse and only the part of the system illuminated by the probe actually contributes to the measured signal that is emitted. In that overlap region between the two pulses, the pump pulse is well approximated by a plane wave. Making a similar assumption that the pump probe is well represented by a plane wave leads to the form for the light pulses in Eq. 1.3. This in turn leads us to the phase-matching condition for particular spectroscopies (see Sec. 3.1 for further details on how phase-matching conditions are obtained) of the kind shown above. If instead both pulses were focused close to the diffraction limit, the phase-matching conditions would need to be modified to incorporate the change of wavectors in each beam.

Furthermore, for all simulations, we consider this time a system made of a dimer of coupled three-level systems (3LS) of the kind described in Chapter 4, with a cartoon depiction of the dimer shown in Fig. 1.4.

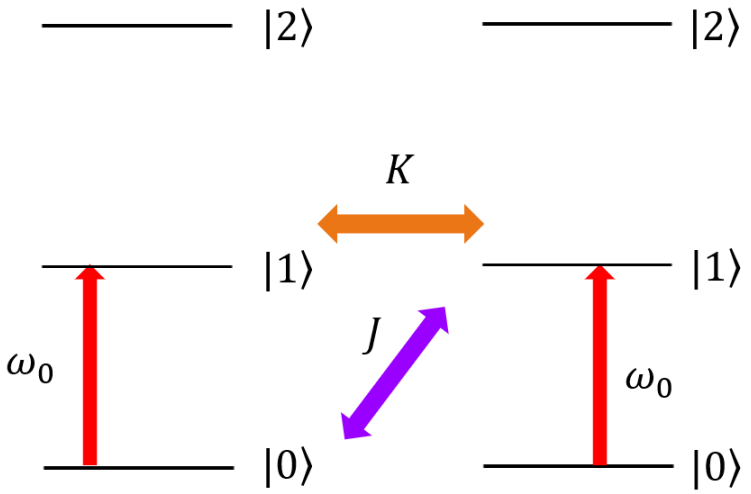

Figure 1.4: Energy-level diagram of 2 identical three-level systems, with single- and double-exciton couplings J and K respectively. For more details about single-exciton coupling and double-exciton coupling, see Sec. 2.1 and 4.1 respectively.

1.3.1 Transient Absorption Spectroscopy

Transient absorption (TA) spectroscopy is the simplest example of the pump-probe class of NLOSs. In a pump-probe experiment, a first light pulse, which we call the pump, interacts with and excites the system. After a certain delay time T, the second light pulse, the probe, arrives and interacts with the system. Figure 1.5 (a) depicts a schematic of a typical TA spectroscopy setup. In transient absorption spectroscopy, we measure the change in absorption of the probe after the system has been excited, compared to the absorption in the absence of a pump, which corresponds to the linear absorption signal. Thus, the signal we obtain is

$$S_{TA}(t,T) = S_{after\,excitation}(t,T) - S_{LA},$$

where we have substracted the linear absorption signal S_{LA} of the probe without a pump from the signal using a pump. This transient absorption signal is measured over a range of delay times.

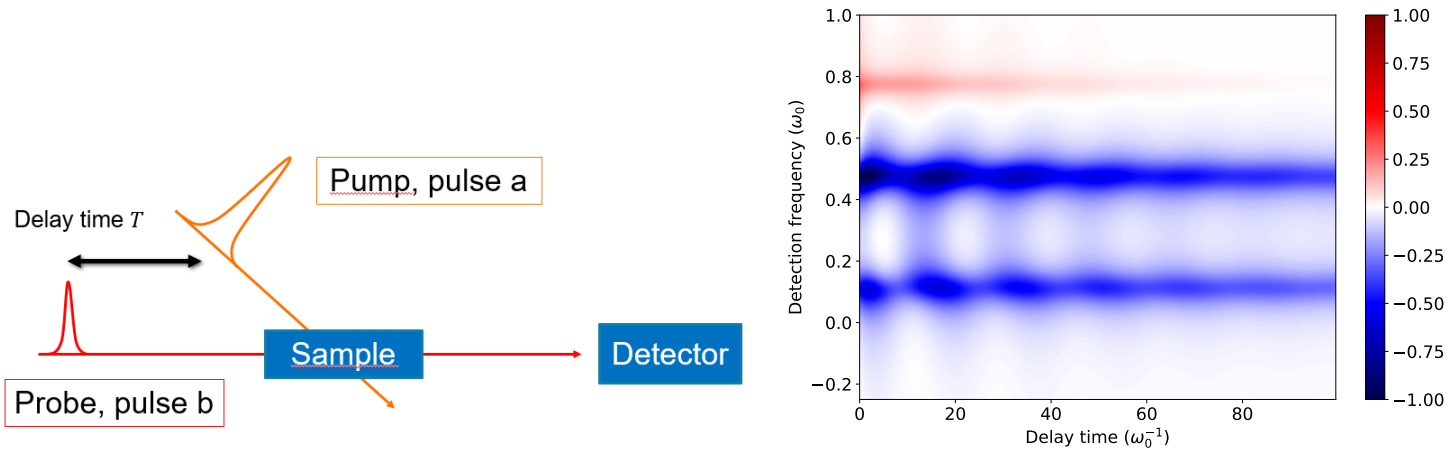

Figure 1.5: (Left) Pump-probe experiment schematic. (Right) Simulated transient absorption signal for two coupled 3LSs, where each 3LS is identical to the one shown in panel (c) of Fig. 1.2. The horizontal axis corresponds to the delay time T between the pump and probe pulses, the vertical axis represents the detection frequency ω of the signal and the colourbar corresponds to the signal amplitude, which is normalized such that the highest peak in the signal has unit amplitude. The regions of the signal in red are positive in amplitude and thus represent an increase in the probe absorption, while the regions in blue are negative in amplitude and correspond to a decrease in the probe absorption.

Figure 1.5 (b) above shows a full TA spectrum for a dimer of coupled three-level systems. Since spectra of this sort can be difficult to interpret or analyze in their colourplot forms, it is often convenient to take a linecut, either horizontally or vertically. A vertical linecut gives us the frequency spectrum at a particular delay time T. On the other hand, a horizontal linecut at a particular frequency ω on the y-axis instead allows to study the signal amplitude at a particular frequency, for all delay times T, which can show relaxation effects due to the system's coupling to the bath. Examples of vertical and horizontal linecuts are shown in Fig. 1.6 and 1.7 respectively.

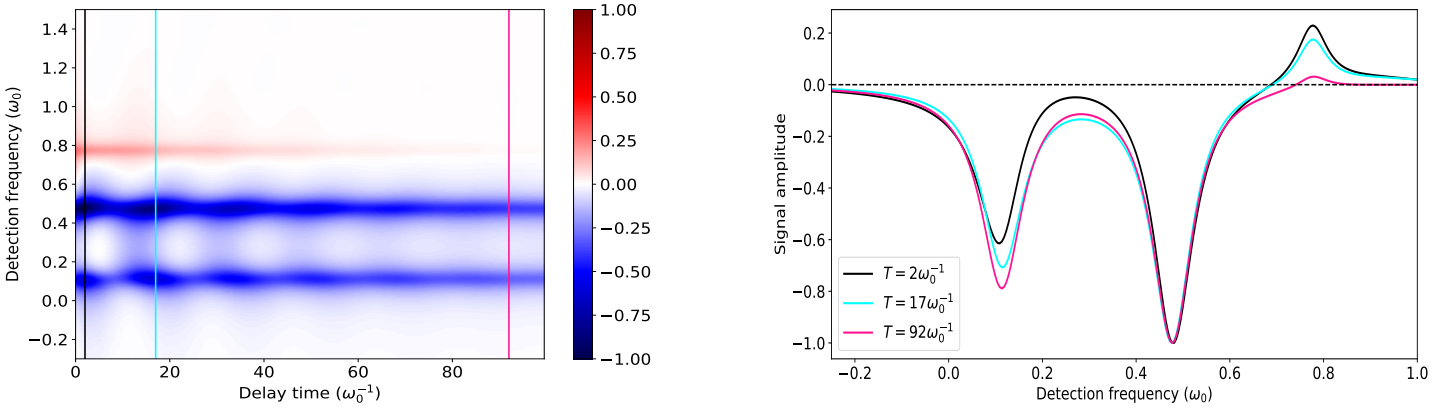

Figure 1.6: (a) Transient absorption spectrum for coupled 3LSs from Fig. 1.5(b) (b) Vertical linecuts from panel (a) at 3 different delay times : $T = 2\omega_0^{-1}$ (cyan line), $T = 17\omega_0^{-1}$ (pink line) and $T = 92\omega_0^{-1}$ (black line).

Panel (b) from Fig. 1.6 shows three distinct peaks in the signal for all chosen delay times T, two of which are negative and one of which is positive, with each peak representing one of the physical process that can be studied with TA spectroscopy. The presence of those three peaks (or sometimes two, if the two negative peaks spectrally overlap) is typical of TA spectra [13, 14]. The two negative peaks, centered around $\omega = 0.125\omega_0$ (left peak), $\omega = 0.475\omega_0$ (middle peak) represent the contribution of ground-state bleach (GSB) and stimulated emission (SE) to the total signal, while the peaked centered around $\omega = 0.77\omega_0$ (right peak) represents the excited-state absorption contribution (ESA). We go into more details about all three processes in Chapter 3 but give here a brief explanation of each.

Ground-state bleach is the process by which the pump pulse first excites the system, meaning there are now fewer molecules in the ground state; it has been bleached. There are now fewer states that can absorb light from the probe pulse and thus the overall absorption has been reduced. In stimulated emission, the probe pulse first excites the system. When the probe pulse interacts with the system, it can induce emission from some of the excited states, which return to the ground state. Stimulated emission represents an additional emission of photons and hence a negative contribution to absorption. Finally, in excited-state absorption, part of the probe pulse is instead absorbed by the molecules in the excited state, instead of causing them to emit back into the ground state as in SE. Since more light has been absorbed during the ESA process, the contribution to the signal will be positive.

If we instead choose to take horizontal linecuts of the spectrum in Fig. 1.5(b), we can for example study how the GSB, SE and ESA signals in Fig. 1.6(b), centered around different frequencies ω, evolve as a function of the delay time T. This is shown in the figure below.

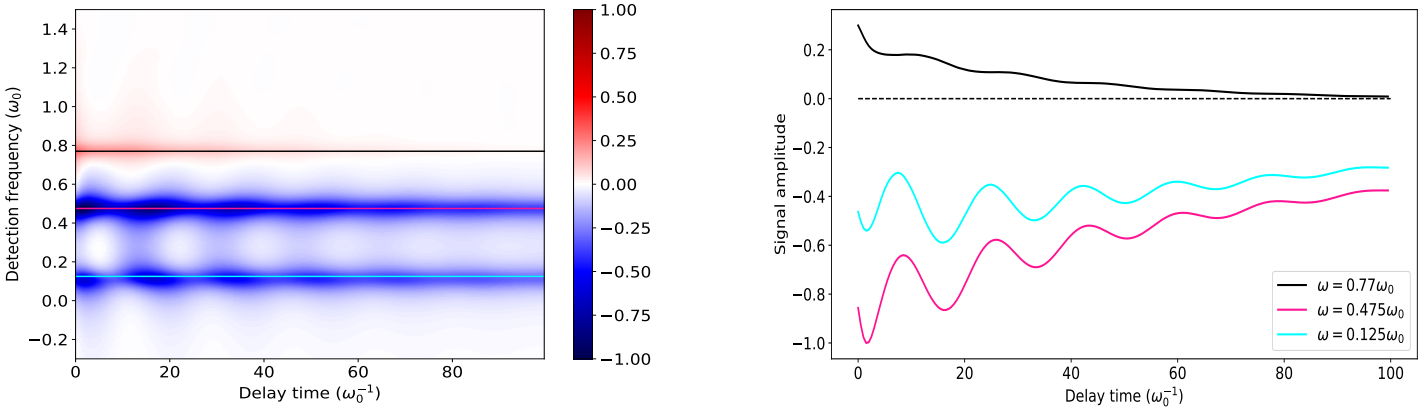

Figure 1.7: (Left) Transient absorption spectrum for coupled 3LSs from Fig. 1.5 (Right) Horizontal linecuts from panel (a) at 3 different frequencies : $\omega = 0.125\omega_0$ (cyan line), $\omega = 0.475\omega_0$ (pink line) and $\omega = 0.77\omega_0$ (black line). The dashed black line is the zero signal amplitude line serving as a reference point.

The black curve, which corresponds to the positive ESA signal, progressively decays to a steady state with zero amplitude. The relaxation time, which is the time between either two successive peaks or troughs, is around $18\omega_0^{-1}$ for this signal. The cyan and pink curves, which correspond to the GSB and ESA signals respectively, reach a steady state with nonzero amplitude, and both have a relaxation time of $17\omega_0^{-1}$. We can see that using this approach allows us to obtain for example the relaxation and dephasing times of the different contributions to the total signal.

Homogeneous broadening of the lineshapes can be seen in Fig. 1.2(b) or the right panel of Fig. 1.6, where the different absorption peaks are broadened, which is due to relaxation processes, causing the molecules to have a homogeneous linewidth; otherwise, without any broadening, the lineshapes would be in theory perfect δ-functions. If in addition each individual unit also has a slightly different surrounding environment, the lineshapes will be inhomogeneously broadened as well. If the inhomogeneous broadening is large enough, it can in some cases cause the individual peaks in a spectrum to overlap, rendering them indistinguishable, as shown in both panels of Fig.1.8.

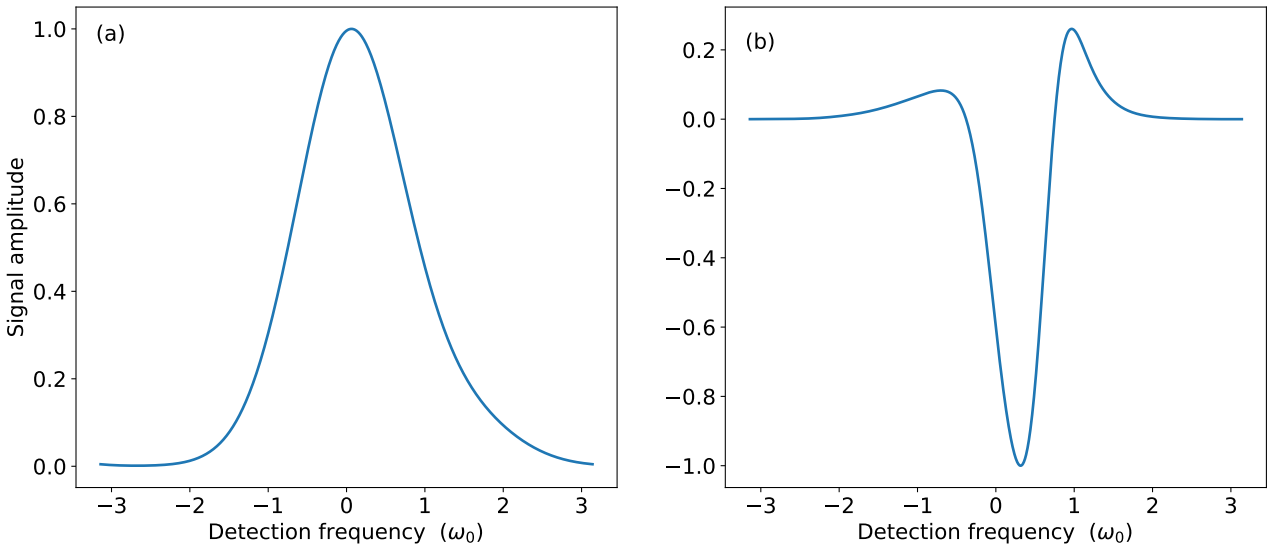

Figure 1.8: (a) Inhomogeneously broadened LA signal from Fig. 1.2(b) Inhomogeneously broadened TA signal ,at delay time $T = 0\omega_0^{-1}$, from the right panel of Fig. 1.6, shown for a broader ranger of detection frequencies.

The broadened linear absorption spectrum shows what appears to be a single peak. The asymmetry of the spectrum, which is noticeable in the shape of the tails of the peak, with the right tail being heavier than the left, could be indicative that there is in fact more than a single absorption peak in that particular region. Similarly, the previously seperated GSB and SE peaks visible in the spectrum Fig. 1.6(b) have been smeared together and become completely indinstinguishable in Fig. 1.8(b). Neither linear nor transient absorption spectroscopies can make the distinction between homogeneous and inhomogeneous broadening effects. However, a different nonlinear spectroscopy, the two-pulse photon echo spectroscopy, offers such a possibility, and is discussed in the following section.

1.3.2 Two-pulse Photon Echo Spectroscopy

We may use the setup shown in Fig.1.5 (a), this time placing a detector in the $-\mathbf{k}_a + 2\mathbf{k}_b$ direction, measuring the so-called two-pulse photon echo (2PPE) signal. The 2PPE experiment can be used to separate the homogeneous and inhomogeneous broadening of spectral lineshapes.

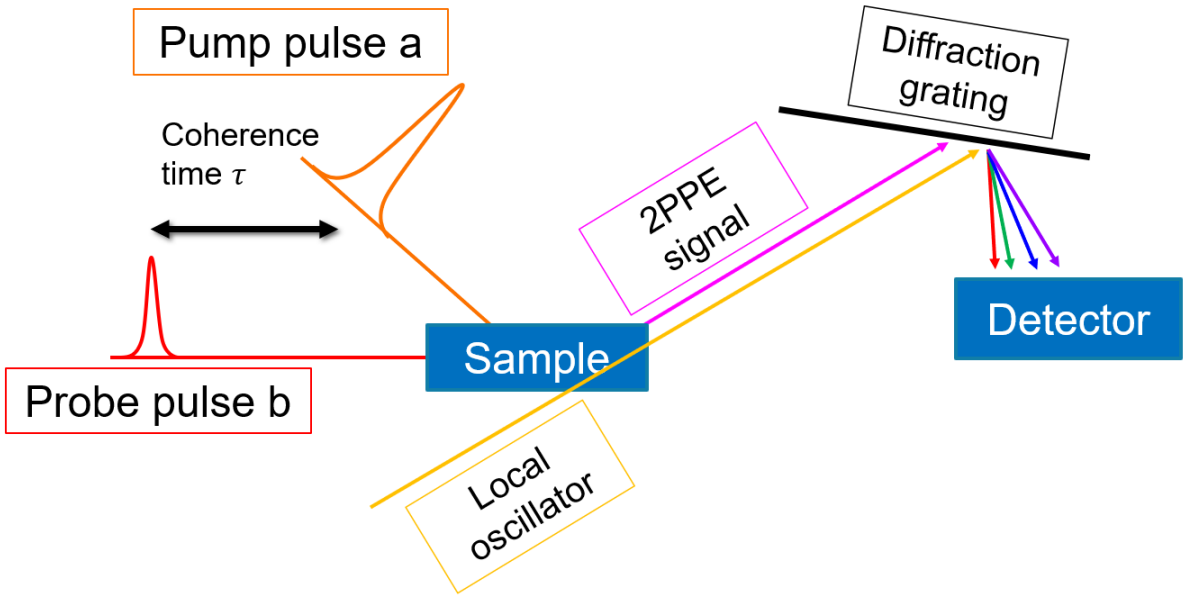

Figure 1.9: Two-pulse photon echo schematic. The emitted 2PPE signal is mixed with a third reference pulse, called the local oscillator (LO) and is measured in the $\mathbf{k}_s = -\mathbf{k}_a + 2\mathbf{k}_b$ direction. Mixing of the signal with a reference LO allows to obtain information regarding the signal's amplitude and phase, rather than simply its intensity. This is a heterodyne detection scheme, as opposed to a homodyne detection one, with both types being covered more extensively in Chapter 3. Using a diffraction grating in conjunction with, for example, a charge-coupled device as a detector, gives the signal in the frequency domain rather than the time domain, should that be desirable. The purpose of the diffraction grating is to separate out the spectral components of the signal.

In a 2PPE experiment as shown above, the delay time τ between pulse a and b is called the coherence time, while the time between the last pulse and the local oscillator is dubbed the rephasing time, denoted t. The photon-echo signal is measured for all times t, varying the coherence time τ. Figure 1.12 below shows simulated photon-echo signals spectra, excluding and including inhomogeneous broadening effects.

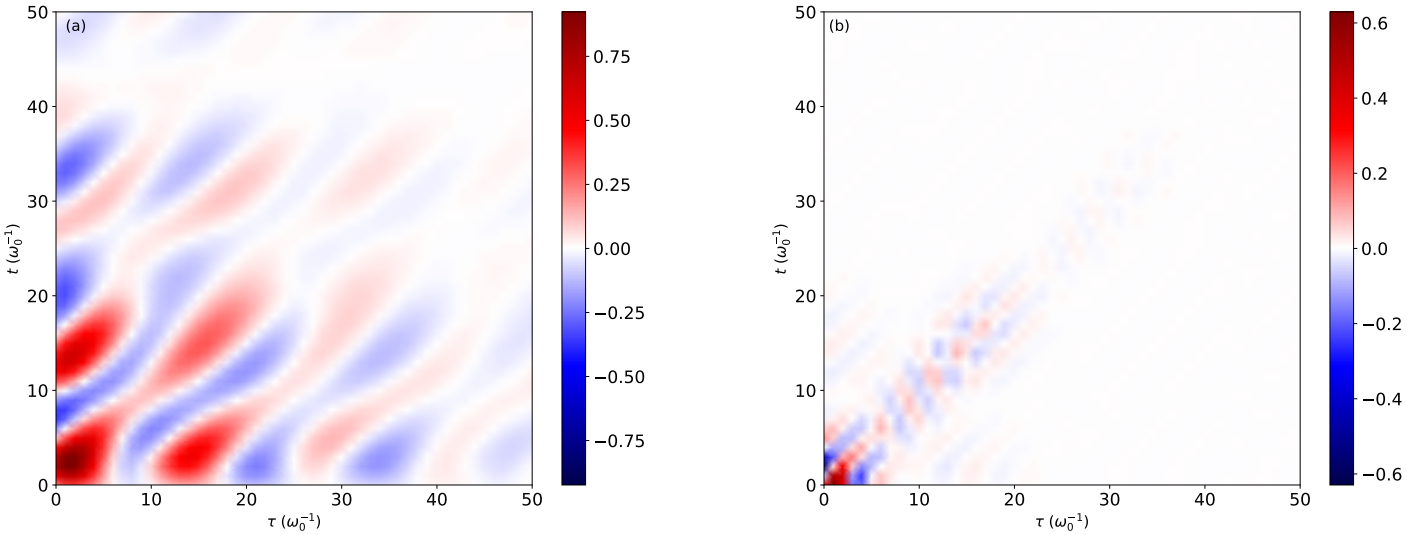

Figure 1.10: Two-pulse photon echo spectra (a) without inhomogeneous broadening and (b) with inhomogeneous broadening for a dimer of 3LS, identical to the system used in Sec. 1.3.1. Inhomogeneous broadening occurs when the atoms or molecules in a system are surrounded by (and thus interact with) different environments. This in turn causes the molecules to have different energy gaps. For example, in the presence of an inhomogeneous environment around the dimer from Fig 1.4, the $|0\rangle \rightarrow |1\rangle$ energy gap of the left molecule in the figure, ω_0, would be different from the $|0\rangle \rightarrow |1\rangle$ energy gap of the right molecule in the same figure, which would be $\omega_0 + \delta$. This causes the different molecules to interact with different frequencies of the light pulses used for a spectroscopy. This causes the emitted signals from the different molecules to oscillate at different frequencies in the spectrum. Hence, in the case of the dimer in Fig. 1.4, the time at which the emitted signal amplitude of one molecule is maximal occurs at a different time than the other molecule. The spectrum is thus an average of those signals occuring at various times and the total signal is thus smeared out, which is what is observed in panel b) of the figure above (and in panel b) of Fig. 1.12 below). Additionally, the signal decreases in amplitude with τ and t, as the different oscillations become more and more out of phase. In this simulation, inhomogeneous broadening is modeled as a Gaussian disorder of the energies of the individual monomers, with standard deviation $\sigma = 0.5\omega_0$.

The 2PPE signal, contrary to the TA signal, does not measure a change in absorption of the incident light passing through the system. As such photon-echo signals are not as straightforward to interpret as their transient absorption counterparts. As is typically the case in the study of pertubative nonlinear spectroscopies, we can gain a better understanding of what a particular signal represents by analysing the double-sided Feynman diagram, or diagrams if there are more than one, that represent a contribution to said signal. Feynman diagrams in the context of NLOS are covered more extensively in Chapter 3, though we give here a brief overview of their interpretation. In the case of the two-pulse photon echo signal, the contributing Feynman diagrams are shown in Fig. 1.11.

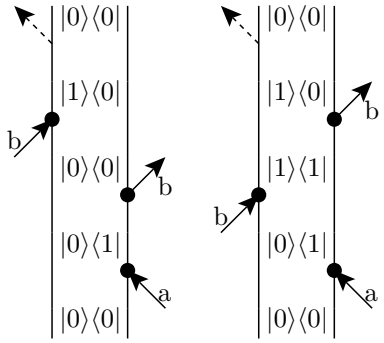

Figure 1.11: Double-sided Feynman diagrams representing a contribution to the two-pulse photon echo signal. In a diagram, time moves from bottom to top. The left and right vertical lines respectively represent the ket- and bra-side of the system's density matrix ρ. A right-pointing arrow represents a rotating term, associated with a term of phase $e^{i\mathbf{k}_j\cdot\mathbf{r}}$ in Eq. 1.3, while a left-pointing arrow represents a counter-rotating term associated with a term with phase $e^{-i\mathbf{k}_j\cdot\mathbf{r}}$. In the RWA (see Appendix A), rotating terms represent an electronic excitation of the ket-side and de-excitation of the bra-side of ρ, while counter-rotating terms represent de-excitation of the ket-side and excitation of the bra-side of ρ. We consider that between each interaction represented by arrows, the system evolves unitarily at frequency $e^{i(\omega_{bra}-\omega_{ket})t'}$, where t' is the time between two subsequent interactions (where for example in the 2PPE experiment, $t' = \tau$ between pulses a and b and $t' = t$ after pulse b has finished interacting with the system).

Looking first at the left diagram of Fig. 1.11, pulse a excites the bra-side of ρ, bringing the system in a coherence state $|0\rangle\langle 1|$. This first pulse builds a polarization field withing the system, which evolves at a frequency $e^{i(\omega_1-\omega_0)\tau} = e^{i\omega_{10}\tau}$; ω_{10} is the transition frequency from one of the two singly-excited eigenstates to the ground state of the dimer. Before the arrival of pulse b, each monomer has thus a polarization with an acquired phase of $e^{i\omega_{10}\tau}$. The interaction with pulse b causes the system to be in a coherence state $|1\rangle\langle 0|$, meaning the two sites will now have a polarization field accumulating an additional phase $e^{i(\omega_0-\omega_1)t} = e^{-i\omega_{10}t}$, with the total phase of the polarization field of each monomer being the product of the two accumulated phases, $e^{i\omega_{10}\tau}e^{-i\omega_{10}t}$. Therefore, when $\tau = t$, the individual polarizations will have a phase of $e^{i\omega_{10}\tau}e^{-i\omega_{10}\tau} = 1$, at which point the signal will have maximum amplitude. This peak in the signal, which can be seen in Fig. 1.10 (a) and in Fig 1.10 (b), is the so-called echo from which the two-pulse photon echo experiment derives its name from. The echo decays by a factor of $e^{-2\gamma\tau}$, with γ being the monomers homogeneous dephasing rate.

Obtaining the 2D Fourier transform of the photon-echo signals in the time-domain, where the signal is a function of times t and τ, yields spectra as functions of the frequencies ω_t and ω_τ, which are the frequency-frequency correlation plots shown in Fig. 1.12 below.

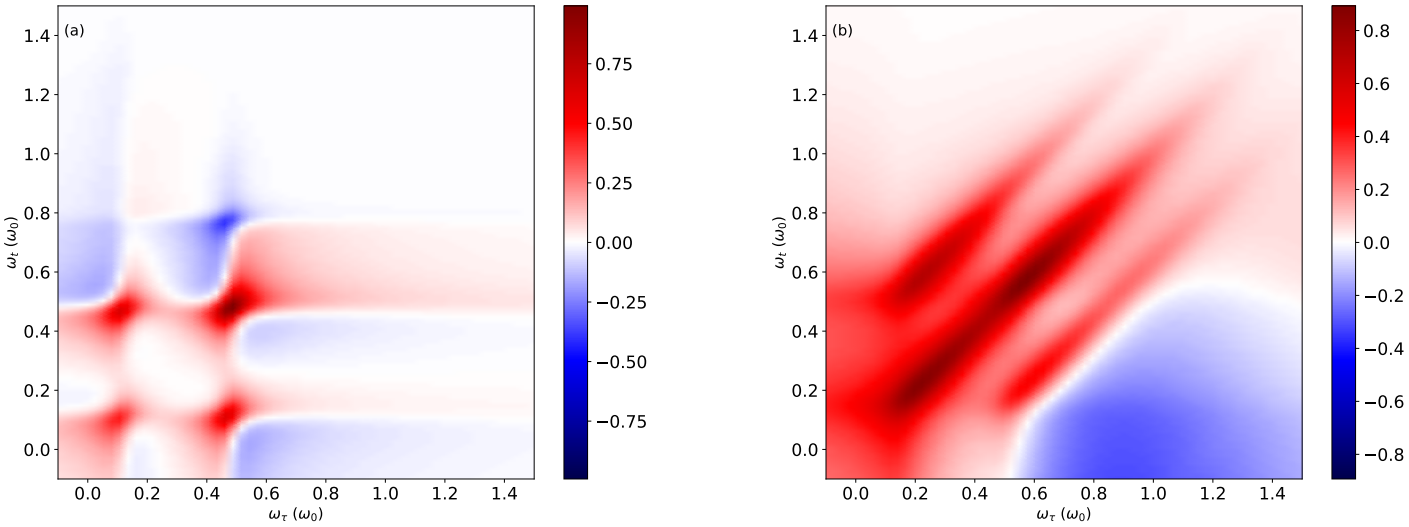

Figure 1.12: 2D Fourier transform of two-pulse photon echo spectra from Fig. 1.10 (a) without inhomogeneous broadening and (b) with inhomogeneous broadening.

The left panel of Fig. 1.12 shows the presence of four distinct peaks in the frequency-frequency correlation plot. The diagonal peaks along the line $\omega_\tau = \omega_t$ reveal that the system is first excited at a particular frequency ω_τ and subsequently emits a signal which is detected at the same frequency. The cross-peaks on the other hand represent an excitation at some frequency ω_τ and a detection at a different frequency, and their presence is indicative of a coupling between individual monomers. The right panel of Fig. 1.12 shows the 2PPE signal including inhomogeneous broadening. It reveals both the homogeneous lineshape due to homogeneous dephasing of the signal, along the anti-diagonals, while simultaneously revealing the inhomogeneous broadening of the lineshape, along the diagonals.

Chapter 2

Hamiltonians and Liouvillians of Polymers

Simulations of any kind, whether in physics or any other field of study for that matter, generally require the use of some model. In simulations of nonlinear optical spectroscopies, one approach consists of creating a model describing a molecular system's electronic and vibrational structure. These vibronic systems are the type of models used throughout this thesis. In this chapter, we will explore how an individual monomer (also referred to as a site or unit) is modeled as a two-level system (2LS, Fig. 2.1), interacting with vibrational modes and which can be electronically coupled to adjacent units via Coulomb interaction.

The first section explores the Hamiltonian structure of both single monomers and aggregates of monomers, polymers, when the whole system is isolated and no coupling to a bath is considered. The second section covers the case where the system is coupled to a surrounding environment, and the open quantum systems formalism is used to describe the model with a Liouvillian. Since the ultimate goal is to use those models for numerical simulations, we express those Hamiltonians and Liouvillians as finite matrices that can be manipulated by a computer for calculations.

These simple models of 2LS are of course crude approximations of the true electronic structures of typical monomers. They nonetheless allow the observation of some common features that are characteristic of some class of systems, where a finer description of the electronic structure may not be necessary for accurate NLOS simulations purposes.

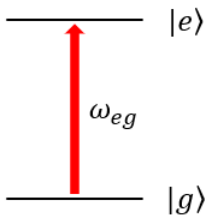

Figure 2.1: Energy diagram of a two-level system (2LS). The system is composed of an electronic ground state $|g\rangle$ and a singly-excited state $|e\rangle$. The transition frequency between either state is given by ω_{eg}.

2.1 Hamiltonians of closed systems

In this section, we focus on the mathematical structure of the Hamiltonian modeling a polymer consisting of n coupled monomers of two-level system. Each unit is made up of a ground state $|g_i\rangle$ with energy $\varepsilon_{g,i}$ and a singly-excited state $|e_i\rangle$ with energy $\varepsilon_{e,i}$. An excitation on site i is represented by the creation operator $a_i^\dagger$, such that $a_i^\dagger|g_i\rangle = |e_i\rangle$. Inversely, a de-excitation is represented by the Hermitian conjugate of $a_i^\dagger$, the annihilation operator a_i. If there are multiple sites, we can include an electronic coupling J_{ij} between excitations i and j, where J_{ij} is a matrix element of the Hermitian coupling matrix J. For a single site, the Hamiltonian and the associated operators are expressed using second quantized notation as 2×2 matrices (and states as 2×1 vectors):

$$a_i^\dagger = \begin{pmatrix} 0 & 0 \\ 1 & 0 \end{pmatrix}, \quad a_i = \begin{pmatrix} 0 & 1 \\ 0 & 0 \end{pmatrix}, \tag{2.1}$$

$$H_i = \begin{pmatrix} \varepsilon_{g,i} & 0 \\ 0 & \varepsilon_{e,i} \end{pmatrix} = \varepsilon_{g,i} a_i a_i^\dagger + \varepsilon_{e,i} a_i^\dagger a_i,$$

If we have, for example, two sites labeled 1 and 2, the total electronic Hamiltonian including inter-unit coupling is, in the Hilbert space of the full system,

$$\begin{aligned} H_{el} &= H_1 \otimes I_2 + I_1 \otimes H_2 \\ &= \left(\varepsilon_{g,1} a_1 a_1^\dagger \otimes I_2 + I_1 \otimes \varepsilon_{g,2} a_2 a_2^\dagger\right) + \left(\varepsilon_{e,1} a_1^\dagger a_1 \otimes I_2 + I_1 \otimes \varepsilon_{e,2} a_2^\dagger a_2\right) + J_{12} a_1^\dagger a_2, \end{aligned} \tag{2.2}$$

where I_1 and I_2 are the 2×2 identity matrices for the Hilbert subspace of site 1 and 2 respectively, and $\otimes$ is the Kronecker product. We note that there is no spatial dependence in the Hamiltonian above. This is since we generally assume that the size or length of the molecular systems seen in this thesis are much shorter than the wavelength of the light pulses considered for the various spectroscopies. This in turn implies that all the units in a single molecule interact identically with the pulses and experience the same phase of the light and we therefore

need not worry about the position of the individual units within the system.

Under the above assumption regarding molecular system's size, we can then simply generalize Eq. 2.2 to n sites without adding any additional mathematical structure to it, and choosing the ground-state energies $\varepsilon_{g,i}$ of each site to be 0, we have, omitting the $\otimes$ symbol for simplicity

$$H_{el} = \sum_{i=1}^{n} \varepsilon_{e,i} a_i^\dagger a_i + \sum_{j=i+1}^{n} \sum_{i=1}^{n} J_{ij} a_i^\dagger a_j. \tag{2.3}$$

We can also include m harmonic vibrational modes in the system, which can originate from the vibrations of a single site, one or more vibrations of all sites, or any combination of the two, where only some sites would have vibrational modes. The modes each have a frequency ω_k, generalized coordinate and momentum q_k and p_k respectively, with $q_k = \frac{1}{\sqrt{2}}(b_k + b_k^\dagger)$ and $p_k = \frac{i}{\sqrt{2}}(b_k - b_k^\dagger)$ and $b_k^\dagger$, b_k the ladder operators of the quantum harmonic oscillator. The total vibrational Hamiltonian for all harmonic modes is

$$H_{vib} = \frac{1}{2} \left(\sum_{k=1}^{m} \omega_k^2 q_k^2 + p_k^2 \right). \tag{2.4}$$

The oscillators also couple to the excited electronic states. The standard linear coupling of the position q_k of each vibration to an individual excitation $a_i^\dagger a_i$ on site i is given by [15]

$$H_{el-vib} = \sum_{k=1}^{m} \sum_{i=1}^{n} \omega_k^2 d_{k,i} q_k a_i^\dagger a_i. \tag{2.5}$$

where the $d_{k,i}$ are coupling constants, corresponding to the displacement between the electronic ground state and excited state, as seen in Fig. 2.2 . Briefly, we note that the Hamiltonians in Eq. 2.4 and 2.5 are formally infinite, since each vibrational mode has in theory an infinite number of exictation. In order to obtain computationally useful expressions for the Hamiltonians, we must limit the number of excitations of each oscillator to a finite number, effectively truncating the matrices that represent H_{vib} and H_{el-vib}.

Putting together Eqs. 2.3, 2.4 and 2.5, we obtain the system's full Hamiltonian,

$$H_0 = H_{el} \otimes I_{vib} + I_{el} \otimes H_{vib} + H_{el-vib}, \tag{2.6}$$

where I_{el} and I_{vib} are the identity operators of the electronic and vibrational Hilbert space respectively.

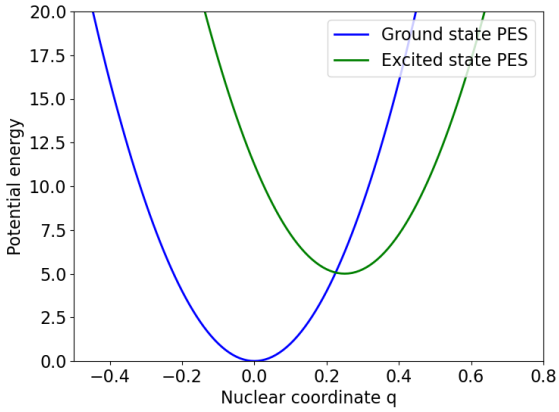

Figure 2.2: Potential energy surfaces of the ground and excited states of an electronic two-level system.

Since the goal is to use this model to simulate spectroscopic signals which arise from an interaction between a system and light, we must also define an operator modelling this light-matter interaction. If we work within the electric dipole approximation, this operator is the transition dipole operator $\boldsymbol{\mu}$, where bold symbols indicates that an operator is a Cartesian vector. In practice, we first define a transition dipole for each site i,

$$\boldsymbol{\mu}_{eg,i} = (\mu_{x,i}, \mu_{y,i}, \mu_{z,i}), \tag{2.7}$$

with the different components of this vector representing a different polarization for each x, y, z direction. The components systems have the form

$$\mu_{\alpha,i} = f_{\alpha,i}(a_i^\dagger + a_i); \;\; \alpha = x, y, z, \; f_i \in \mathbb{R}$$

This form of transition dipoles describes both the transition from an electronic ground state $|g_i\rangle$ to singly-excited state $|e_i\rangle$ and the reverse transition, hence the eg subscript. The factor f_i is a real factor characterizing the magnitude of this transition. The dipole operator for the full system with n sites is

$$\boldsymbol{\mu} = \boldsymbol{\mu}_{eg} = \boldsymbol{\mu}_{eg,1} \otimes I_2 \otimes ... \otimes I_n + I_1 \otimes \boldsymbol{\mu}_{eg,2} \otimes ... \otimes I_n + I_1 \otimes I_2 \otimes ... \otimes \boldsymbol{\mu}_{eg,n}.$$

If we have an interaction with the system with L light pulses, described by their electric fields

$$\mathbf{E}(t) = \sum_{j=1}^{L} \mathbf{E}_i(t),$$

we have the interaction Hamiltonian in the dipole approximation that is given by

$$H'(t) = -\boldsymbol{\mu} \cdot \mathbf{E}(t), \tag{2.8}$$

and the full time-dependent Hamiltonian consisting of the system's Hamiltonian from Eq. 2.6 and the interaction

$$H(t) = H_0 + H'(t).$$

The time-dependent Schrödinger equation then becomes

$$\frac{d|\psi(t)\rangle}{dt} = -\frac{i}{\hbar} H_0 |\psi(t)\rangle - \frac{i}{\hbar} H'(t) |\psi(t)\rangle \tag{2.9}$$

2.2 Liouvillians of open systems

Hamiltonians, including those seen in Sec. 2.1, are sufficient to describe the dynamics of an isolated system without any contact to a surrounding environment. Realistically however, most physical systems do interact with an external environment, also called a bath, and we must treat the system as being open. The total Hamiltonian in this case will be partitioned as

$$H = H_S \otimes I_B + I_S \otimes H_B + H_{SB}, \tag{2.10}$$

where H_S (H_B) and I_S (I_B) are the Hamiltonian and identity operator of the system (bath) Hilbert space $\mathcal{H}_S$ ($\mathcal{H}_B$) and H_{SB} is the system-bath interaction Hamiltonian. Assuming all vibrational modes not explicitly written in 2.4 are part of the bath and following Ref. [16], a linear coupling of the system to the bath is obtained by expanding H_{SB} to lowest order in the bath degrees of freedom, yielding

$$H_{SB} \approx \sum_p O_{p,S} \otimes \sum_{k'} \lambda_{p,k'} q_{k'} \tag{2.11}$$

$$= \sum_p O_{p,S} \otimes O_{p,B} \tag{2.12}$$

where $O_{p,S}$ and $O_{p,B}$ are operators defined in $\mathcal{H}_S$ and $\mathcal{H}_B$ respectively. The $\lambda_{p,k'}$ are linear coupling constants of the vibrational modes of the baths and the $q_{k'}$ are their vibrational coordinates. The index p corresponds to either a site index i or a vibrational index k such as the indices in Eq. 2.3 or 2.4.

This system-bath coupling leads to dephasing and dissipation processes which cannot be treated with the wavefunction description of a system and the Hamiltonian formalism. Instead, we represent the system using a density matrix ρ, which is defined as

$$\rho = \sum_i c_i |i\rangle\langle i|, \quad c_i \in [0, 1], \tag{2.13}$$

where $|i\rangle$ are the wavefunctions of the system. The density matrix has the following properties:

- Hermiticity : $\rho_{ij} = \rho^*_{ji}$;
- Its diagonal elements ρ_{ii} are non-negative; ρ_{ii} can thus be interpreted as the probability of the system to be in state $|i\rangle$;
- As a consequence of the last property, $Tr\{\rho\} = 1$ since the sum of all probabilites cannot exceed 1;
- For any density matrix $Tr\{\rho^2\} \leq 1$.

Deriving Eq. 2.13 with respect to time and using the definition of $\dot{\psi}(t)$ from Eq. 2.9 (ignoring for now the perturbation $H'(t)$) yields the Liouville-von Neumann equation for the density matrix

$$\frac{d\rho(t)}{dt} = -\frac{i}{\hbar}\left[H_0, \rho(t)\right], \tag{2.14}$$

with $[A, B] = AB - BA$ the commutator operator.

Compared to Eq. 2.9, Eq. 2.14 adds no new physics to the model and its solutions are therefore the same as the solutions to Eq. 2.9, meaning we are better off using wavefunctions instead of density matrices. However, including a coupling between the system and bath in our model requires the use of density matrices. Mathematically, this system-bath coupling represents the addition of an extra term D in Eq. 2.14, yielding the following equation,

$$\frac{d\rho(t)}{dt} = -\frac{i}{\hbar}\left[H_0, \rho(t)\right] + D\rho(t). \tag{2.15}$$

The D term in the equation above is called the dissipation superoperator. It models the system-bath coupling leading to dephasing and relaxation phenomena and its specific form will depend upon which formalism is used to treat the bath.

Defining the Liouvillian $\mathcal{L}_0$ as

$$\mathcal{L}_0 = -\frac{i}{\hbar}H_0 \otimes I_S + \frac{i}{\hbar}I_S \otimes H_0^T + i\hbar D, \tag{2.16}$$

for a general dissipation term D, we arrive at

$$\frac{d\rho(t)}{dt} = \mathcal{L}_0\rho(t). \tag{2.17}$$

The Liouvillian $\mathcal{L}_0$ is a superoperator acting on the vector space $\mathcal{V}$ of linear operators acting on the Hilbert space $\mathcal{H}$ of H_0, with $\rho \in \mathcal{V}$. The formulation of Eq. 2.17 in terms of superoperators leads to two possible representations for ρ and $\mathcal{L}_0$. If the dimension of $\mathcal{H}$ is N, then the density matrix can be written as an $N \times N$ matrix and the Liouvillian as an $N \times N \times N \times N$ tensor; this is the Hilbert space representation. We can instead choose to write

ρ as a Liouville space vector $|\rho\rangle\rangle$, in which case it will be a vector of length N^2 and $\mathcal{L}_0$ will be an $N^2 \times N^2$ matrix; this is the Liouville representation.

If the dissipative part of the Liouvillian D is zero, then we are left with Eq. 2.14 describing a closed system. Otherwise, if $D \neq 0$, we must obtain an expression for it. We focus solely on expressions for D that arise from Redfield theory [17], since they are the form used in all our simulations of NLOSs with open systems.

Redfield theory was initially conceived to derive an equation of motion for the density matrix of a system in contact with a thermal bath, allowing the study of relaxation processes in the field of NMR spectroscopy[18]. It has since been used more broadly as a general method of treating system-bath interactions. Redfield formalism is based on a microscopic treatment of the bath and system-bath coupling and as such, is based on physical grounds. In Redfield theory, the bath is conceived as being an infinite set of harmonic oscillators weakly interacting with the system. Any vibrational mode not explicitly included in the system's vibrational Hamiltonian of Eq. 2.4 is relegated to the bath.

Given the system-bath coupling Hamiltonian of Eq. 2.12, the dissipation tensor Y_{ijkl} is defined, for an operator $O_{p,S}$ on the system's Hilbert space, as

$$Y_{ijkl}(O_{p,S}) = \sum_{p,p'} \langle i|O_{p,S}|k\rangle\langle l|O_{p',S}|j\rangle C_{pp'}(\omega_{ki}). \tag{2.18}$$

The states $|i\rangle$ correspond to the eigenvectors of H_0, ω_{ki} are the transition frequency $\omega_k - \omega_i$ between the states $|i\rangle$ and $|k\rangle$ and $C_{pp'}$ are the two-point correlation functions of the vibrational modes of the bath, given in the time-domain by

$$C_{pp'}(t) = \langle O_{p,B}(t)O_{p',B}(0)\rangle, \tag{2.19}$$

where here we assume $C_{pp'}(t) = \delta_{pp'}C_{pp'}(t)$, meaning the cross-correlations are always zero. The frequency-domain correlation functions $C_{pp'}(\omega)$ in Eq. 2.18 are the Fourier transform of $C_{pp}(t)$ and are characterized by a spectral density $J(\omega)$, such that their real part is

$$\mathcal{R}e\left\{C_{pp'}(\omega)\right\} = \frac{1}{2}\hbar J(\omega) coth\left(\frac{\hbar\omega}{2k_BT}\right).$$

The spectral density $J(\omega)$ characterizes the coupling between the bath's vibrational modes at frequency ω and the system. At each frequency, the spectral density describes how many bath modes have that frequency, weighted by how strong their coupling to the system is. A large peak (or peaks if there are many separate ones) in $J(\omega)$ around a particular frequency ω can then either be due to 1) a large number of vibrational modes oscillating at frequencies close to ω or 2) a few strongly coupled modes. The spectral density contains both types of information. Common forms of the spectral density include Ohmic, sub-Ohmic and super-Ohmic. For example, an Ohmic spectral density

can be written as

$$J_{ohmic}(\omega) = 2\lambda\omega, \tag{2.20}$$

where λ is the coupling strength between the system and the bath.

This form of the spectral density ensures that we obtain irreversible dynamics due to relaxation effects. It can be shown [16] that this $J_{ohmic}(\omega)$ yields frequency-independent damping with rate λ for small ω. The presence of the high-frequency vibrational modes of the environment interacting with the system leads to a renormalization of the physical parameters of the system's Hamiltonian. Renormalization in open quantum systems is the effective change, in the sense of perturbation theory, of the energy parameters of the system due to the higher bath frequencies. As an example, the measured $|0\rangle \rightarrow 1$ energy gap in a 2LS includes the effects of the coupling to high-frequency bath modes. To avoid including this change in energy parameters twice (once in the system's Hamiltonian and once in the inclusion of the higher frequencies in the spectral density), we introduce a cut-off function in the spectral density for the higher frequencies ω. This cut-off function ensures that for large values of ω, which can technically be infinite, the spectral density $J(\omega)$ has finite values. In the absence of a cut-off function, the divergent nature of $J(\omega)$ would lead to an infinite system-bath coupling, which is physically unrealistic. Simple analytical forms of these cut-offs are most often considered for convenience [16]. We can take as an example the spectral density in Eq. 2.20 above, including a Lorentz-Drude cut-off,

$$J(\omega) = 2\lambda\omega\frac{\omega_c}{\omega^2 + \omega_c^2}, \tag{2.21}$$

with ω_c the cut-off frequency of the bath. Another example of a cut-off is the exponential one, given by

$$J(\omega) = 2\lambda\omega e^{-\frac{\omega}{\omega_c}}. \tag{2.22}$$

Spectral densities including both types of cut-off are shown in Fig. 2.3. The Ohmic in Ohmic spectral density is not directly related to Ohm's law in electricity but rather to the fact that $J(\omega)$ increases linearly in the low-frequency regime (where $\omega < \omega_C$), similarly to how the voltage V across a resistance increases linearly with the current I in Ohm's law. This linear increase can be seen in Fig. 2.3. More generally, we may write spectral densities as

$$J(\omega) = 2\lambda\frac{\omega^a}{\omega_c^{a-1}} \cdot U(\omega, \omega_c),$$

where $U(\omega, \omega_c)$ is a cut-off function and $a \in \mathbb{R}^+$. The case $a = 1$ corresponds to the Ohmic case, whereas $a < 1$ and $a > 1$ are the sub-Ohmic and super-Ohmic cases respectively.

One of the assumption when generating the Liouvillian for polymers of 2LS is that the spectral density is the same for each site. In certain cases however, a more accurate modeling of the system may require each site to have a different coupling to the bath, meaning that for n units, there are potentially n different spectral densities $J_i(\omega)$

From the dissipation tensor, we have the Redfield tensor R_{ijkl} defined for an operator O,

$$R_{ijkl}(O) = -Y_{ijkl}(O) - Y^*_{jilk}(O) + \delta_{jl}\sum_\alpha Y_{\alpha ik\alpha}(O) + \delta_{ik}\sum_\alpha Y^*_{\alpha jl\alpha}(O). \tag{2.23}$$

Here, we treat two types of relaxation processes : intra-manifold and inter-manifold relaxation. A manifold $\mathcal{M}$ is a subspace of the Hilbert space of H_0, which contains all the states with M electronic excitations. For example, the ground-state manifold (GSM) contains all states of the form $|g_1 g_2 ... g_n, v_1 v_2 ... v_k\rangle$ and superpositions of such states, where all sites are in their electronic ground eigenstate. The singly-excited manifold (SEM) contains states of the form $|e_1 g_2 ... g_n, v_1 v_2 ... v_k\rangle$ (and again superpositions of those states), where a single site is in its first excited state. Thus, intra-manifold relaxation is the process by which higher-energy states within a manifold $\mathcal{M}$ relax to the lower-energy states in the same manifold. On the other hand, inter-manifold relaxation describes states in manifold $\mathcal{M}$ relaxing to states in the lower manifold $\mathcal{M} - 1$.

Intra-manifold relaxation is described by the coupling between the bath and each site i, described by the Redfield tensor,

$$R_{el} = R(a_i^\dagger a_i), \tag{2.24}$$

and by the coupling to each vibrational mode k of the system,

$$R_{vib} = R(q_k). \tag{2.25}$$

Inter-manifold relaxation is treated differently from intra-manifold relaxation and requires a different form of $C_{pp'}(t)$ in Eq. 2.19, involving nonadiabatic coupling terms [19, 20] . Since this form of $C_{pp'}(t)$ with nonadiabatic couplings is more complex, in this thesis, we describe inter-manifold relaxation processes using a simpler flat spectral density, such that the two-point correlation function in frequency is

$$C(\omega) = \begin{cases} \gamma_r e^{\frac{\hbar\omega}{k_B T}} & \omega < 0 \\ \gamma_r & \omega > 0 \end{cases}.$$

The constant γ_r has units of inverse-time and is a phenomelogical inter-manifold relaxation rate at which electronic excitations relax to the ground state. The Redfield tensor describing this inter-manifold relaxation on site i is

$$R_{rel} = R(a_i^\dagger + a_i).$$

Adding all couplings, we arrive at the following definition of the dissipation superoperator D in Eq. 2.15

$$D = -R(a_i^\dagger a_i) - R(q_k) - R(a_i^\dagger + a_i). \tag{2.26}$$

The equation of motion for the density matrix, Eq. 2.15, becomes

$$\frac{d\rho(t)}{dt} = -\frac{i}{\hbar}\left[H_0, \rho(t)\right] - \left(\sum_{i=1}^{n}\left[R(a_i^\dagger a_i) + R(a_i^\dagger + a_i)\right] + \sum_{k=1}^{m} R(q_k)\right)\rho(t). \tag{2.27}$$

We may look at one of the components of D to gain a better understanding of what this operator can physically represent. Taking for example $D_{ii,kk}(a^\dagger + a)$, assuming we have a single, vibrationless two-level system with eigenstates $|0\rangle$ and $|1\rangle$, we have

$$\begin{aligned} D_{ii,kk}(a^\dagger + a) &= -R_{ii,kk}(a^\dagger + a) \\ &= -\left(-Y_{iikk}(a^\dagger + a) - Y^*_{iikk}(a^\dagger + a) + \delta_{ik}\sum_\alpha Y_{\alpha ik\alpha}(a^\dagger + a) + \delta_{ik}\sum_\alpha Y^*_{\alpha ik\alpha}(a^\dagger + a)\right) \\ & Y_{iikk}(a^\dagger + a) + Y^*_{iikk}(a^\dagger + a) - \delta_{ik}\sum_\alpha Y_{\alpha ik\alpha}(a^\dagger + a) - \delta_{ik}\sum_\alpha Y^*_{\alpha ik\alpha}(a^\dagger + a). \end{aligned} \tag{2.28}$$

We have from Eq. 2.18, where for a single site we have $p = p'$ and thus

$$Y_{iikk}(a^\dagger + a) = \langle i|a^\dagger + a|k\rangle\langle k|a^\dagger + a|i\rangle C_{pp'}(\omega_{ki}).$$

Since $i, k = |0\rangle, |1\rangle$, the sole non-zero terms of Y_{iikk} are Y_{1100} and Y_{0011}, and similarly for $Y^*_{iikk}(a^\dagger + a)$ where the only non-zero terms are $Y^*_{1100}$and Y^*_{0011}. Since we have $i \neq k$, the last two sum terms in Eq. 2.28 are zero and we are thus left with the following

$$D_{1100}(a^\dagger + a) = Y_{1100}(a^\dagger + a) + Y^*_{1100}(a^\dagger + a);$$

$$D_{0011}(a^\dagger + a) = Y_{0011}(a^\dagger + a) + Y^*_{0011}(a^\dagger + a).$$

We have for an inter-manifold process

$$Y_{1100} = Y^*_{1100} = C(\omega_{01}) = \gamma_r e^{\frac{\hbar\omega}{k_B T}};$$

$$Y_{0011} = Y^*_{1100} = C(\omega_{10}) = \gamma_r,$$

leading to

$$D_{1100} = 2\gamma_r e^{\frac{\hbar\omega_{01}}{k_B T}},$$

and

$$D_{0011} = 2\gamma_r.$$

The dissipation $D_{iikk}(a^\dagger + a)$ represents a transfer of population from a state k to a state i. The transition from the

state $|1\rangle$ in the SEM to state $|0\rangle$ in the GSM is mediated by the coupling described by the spectral density in D_{0011}, which is simply a constant, while the transition from state $|0\rangle$ to state $|1\rangle$ is mediated by the spectral density in D_{1100}. The farther apart in energy the $|0\rangle$ and $|1\rangle$states are (in other words, how large the negative ω_{01} transition frequency is), the smaller the coupling between the lower-energy state and the higher-energy state is, meaning this particular inter-manifold relaxation transition is energetically unfavorable.

The operator D can also be treated using a completely different formalism, should that be desirable. For example, Lindblad formalism provides a description of inter- and intra-manifold relaxation and dephasing processes using a purely phenomenological approach [21], as opposed to the microscopic approach of Redfield formalism. Lindblad formalism as used in the context of NLOSs is briefly covered in [22].

Introducing a light-matter interaction of the form of Eq. 3.3, we have the interaction Liouvillian

$$\mathcal{L}'(t) = -\frac{i}{\hbar}\boldsymbol{\mu}^K \cdot \mathbf{E}(t) + \frac{i}{\hbar}\boldsymbol{\mu}^B \cdot \mathbf{E}(t),$$

with

$$\boldsymbol{\mu}^K = \boldsymbol{\mu} \otimes I_S,$$

and

$$\boldsymbol{\mu}^B = I_S \otimes \boldsymbol{\mu}^T.$$

Equation 2.17 including this interaction becomes

$$\frac{d\rho(t)}{dt} = \mathcal{L}_0\rho(t) + \mathcal{L}'\rho(t). \tag{2.29}$$

The details of how we use time-dependent perturbation theory to solve both Eq. 2.9 for closed systems and Eq. 2.29 for open systems to obtain a spectroscopic signal are covered in more depth in Chapter 3.

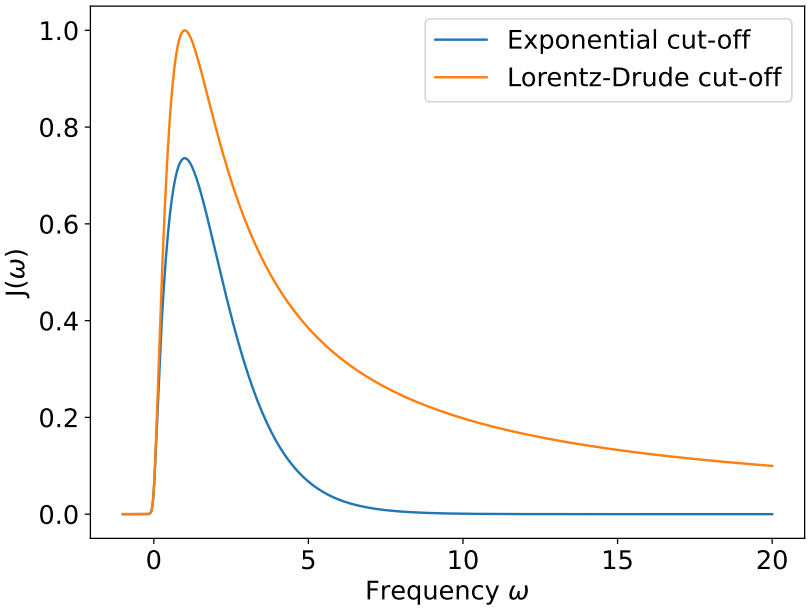

Figure 2.3: Spectral densities with Lorentz-Drude cut-off and exponential cut-off, with parameters for both spectral densities (SD) being identical. The coupling is $\lambda = 1$, the cut-off frequency is $\omega_c = 1$ and the temperature was taken to be room temperature, such that $k_B T = 0.025$. We note that for the same choice of the parameters, the two different cut-offs give rise to significantly different spectral densities $J(\omega)$. The SD with Lorentz-Drude cut-off shows that a much broader range of the phonon modes of the bath have a frequency ω that couples to the system. The SD with exponential cut-off is narrower, with bath modes of frequency $\omega \approx 10$ and above having no coupling at all, in contrast to the SD with Lorentz-Drude cut-off showing significant coupling even at frequencies above $\omega = 20$.

Chapter 3

Calculations of spectroscopic signals

3.1 Nonlinear signals

In this chapter, we discuss how, using a particular model of a system interest, calculations of spectroscopic signals resulting from a light-matter interaction are carried out in theory, using standard and well-known approximations. In general, nonlinear optical spectroscopies make use of an arbitrary number N of optical pulses, which we treat classically as a sum of individual electric fields, given by

$$\mathbf{E}(t) = \sum_{j=1}^{N} \mathbf{e}_j \varepsilon_j(t) + \mathbf{e}_j^* \varepsilon_j^*(t). \tag{3.1}$$

The bold symbols in equation 3.1 represent Cartesian vectors. $\mathbf{e}_j$ is the j-th pulse's polarization vector, which can be any linear combination of Cartesian basis vectors and is of the form $\mathbf{e}_j = x_j\mathbf{x} + y_j\mathbf{y} + z_j\mathbf{z}$, with the coefficients being real or possibly complex numbers (such as in the case of circular polarization). Each pulse is also characterized by its complex amplitude $\varepsilon_i(t)$, written as

$$\varepsilon_j(t) = A_j(t - t_j)e^{-i(\omega_j(t-t_j)+\mathbf{k}_j\cdot\mathbf{r}_j+\phi_j)} \tag{3.2}$$

where $A_j(t - t_j)$ is the envelope function of the pulse, t_j its arrival time, ω_j its carrier frequency, $\mathbf{k}_j$ is the wavevector and ϕ_j the phase of the pulse. As is often done in the context of spectroscopies, we use the electric dipole approximation to represent the interaction of the optical pulses with the system, leading to a time-dependent interaction Hamiltonian of the form

$$H'(t) = -\boldsymbol{\mu} \cdot \mathbf{E}(t), \tag{3.3}$$

with $\boldsymbol{\mu}$ the electric dipole operator of the system.

We wish to obtain an expression for the system in the presence of the interaction from Eq. 3.3. We first start

with a closed system, containing an arbitrary number of molecules, which we assume to all be identical and where each molecule is indexed i, spread over a cube of volume L^3. In order to derive the interaction of the opitcal pulses with the ensemble of molecules, we describe the ensemble using wavefunction formalism, rather than a density matrix, for convenience. Before any interaction with the light pulses, the equation of motion describing the time evolution of the whole system's wavefunction $|\psi\rangle$ is given by the Schrödinger equation,

$$\frac{d\,|\psi(t)\rangle}{dt} = -\frac{i}{\hbar} H_0\,|\psi(t)\rangle \tag{3.4}$$

where H_0 is the system's Hamiltonian. After the system has interacted with the pulses, the full Hamiltonian is given by

$$H(t) = H_0(t) + H'(t), \tag{3.5}$$

leading to the time-dependent Schrödinger equation,

$$\frac{d\,|\psi(t)\rangle}{dt} = -\frac{i}{\hbar} H_0\,|\psi(t)\rangle - \frac{i}{\hbar} H'\,|\psi(t)\rangle\,. \tag{3.6}$$

After all the interactions of the electric fields with the system are over, the sytem is in a state $|\psi(t)\rangle$, which can be determined by finding the solution to Eq. 3.6. Each molecule i composing the system has a microscopic dipole moment, resulting in a total polarization $\mathbf{P}(\mathbf{r},t)$ for the entire sample. This macroscopic dipole moment can be calculated by summing over each molecule's dipole expectation value $\langle \boldsymbol{\mu}_i \rangle$, which yields

$$\mathbf{P}(\mathbf{r},t) = \sum_i \langle \boldsymbol{\mu}_i \rangle = \sum_i \langle \psi_i(t)|\,\boldsymbol{\mu}_i\,|\psi_i(t)\rangle\,, \tag{3.7}$$

where $|\psi_i(t)\rangle$ is the i-th molecule's wavefunction at the position r_i, assuming that $|\psi(t)\rangle$ can be written as product of the $|\psi_i(t)\rangle$. This polarization is the source term in Maxwell's equation, the wave equation,

$$\nabla \times \nabla \times \mathbf{E}_s(\mathbf{r},t) + \frac{1}{c^2}\frac{\partial^2 \mathbf{E}_s(\mathbf{r},t)}{\partial t^2} = -\frac{4\pi}{c^2}\frac{\partial^2 \mathbf{P}(\mathbf{r},t)}{\partial t^2}, \tag{3.8}$$

which emits the far-field radiation $\mathbf{E}_s(\mathbf{r},t)$. For polarization-detected spectroscopies (also known as coherent spectroscopies), this far-field radiation $\mathbf{E}_s(\mathbf{r},t)$ is the signal ultimately detected in an experiment or calculated in simulations. Action-detected spectroscopies on the other hand measure a signal proportional to the fluorescence or photocurrent of the system rather than its polarization [23–26]. In this thesis, we consider only polarization-detected (or coherent-detected) spectroscopies.

We assume that only a small fraction of the incoming light is absorbed by the sample and thus the generated signals are far weaker than the incoming fields. We also assume that the length of the system is large when compared to the wavelength of the incident light pulses in Eq. 3.2. The molecules themselves are small compared

to the wavelength of light, meaning all subunits of each molecule experience only a time-varying field, without a spatial variation. However, the phases of the response of the molecules vary through the position in the sample and the signal is emitted only in phase-matched directions [1, 2]. The $\mathbf{r}$ dependence of $\mathbf{P}(\mathbf{r},t)$ in Eq. 3.7 then comes solely from the $\mathbf{r}$ dependence of the optical fields in Eq. 3.2. We may then solve Eq. 3.8 and, by extension, solve Eq. 3.7 for the system. If the incoming fields have different wavevectors $\mathbf{k}_j$ (or in other words, if we have a noncollinear beam geometry), the macroscopic dipole is proportional to the sum of the signal polarization in all the possible directions $\mathbf{k}_s$ [2],

$$\mathbf{P}(\mathbf{r},t) \propto \sum_s \mathbf{P}_s e^{i(\mathbf{k}_s\cdot\mathbf{r})},$$

where the signal wavector is defined as

$$\mathbf{k}_s = \sum_j n_j \mathbf{k}_j, \quad n_j \in \mathbb{Z}. \tag{3.9}$$

The signal wavector $\mathbf{k}_s$ is any wavevector from the infinite set spanned by the integers n_j. For a particular choice of n_j, Eq. 3.9 is known as the phase-matching condition or phase-matching direction of the signal propagating in direction $\mathbf{k}_s$. Furthermore, if we also assume that the wavelength of the emitted field is much smaller than the dimensions of the system (in other words, if the relation $\frac{1}{k_s} \ll L$ holds), there will be constructive interference in the phase-matching direction $\mathbf{k}_s$ of the signal field E_s. This constructive interference allows one to, in an experimental setting, place a detector along a particular direction of interest $\mathbf{k}_s$ and effectively measure only a single component $\mathbf{P}_s$ of the bulk polarization [2]. From a theoretical perspective, it allows us to choose which signal we are interested in, as a function of the phase-matching direction, which corresponds to a specific choice of the integers n_j. The emitted signal $\mathbf{E}_s$ is proportional to the polarization $\mathbf{P}_s$, following the relation

$$\mathbf{E}_s \propto i\mathbf{P}_s,$$

This result comes directly from the solving the wave equation, Eq. 3.8 [2].

There are two ways of detecting a signal field, one being heterodyne detection and the second being homodyne detection. In a heterodyne detection experiment, a local oscillator (LO) with electric field

$$\mathbf{E}_{LO} = \mathbf{e}_{LO}\varepsilon_{LO}(t) + \mathbf{e}^*_{LO}\varepsilon^*_{LO}(t) \tag{3.10}$$

travels along the $\mathbf{k}_s$ direction and serves as a reference pulse, where we are interested in the LO's interference with the signal field. In most cases, experimentally, the emitted radiation is detected as a function of frequency rather than time, using a diffraction grating to separate out the spectral components of the signal, and a charge-coupled device. From a theoretical approach, this separation of the signal in various spectral components involves taking the Fourier transform of the signal as a function of time, where we use the so-called non-unitary definition of the

Fourier transform of a function $f(t)$,

$$\tilde{f}(\omega) = \int_{-\infty}^{\infty} f(t) e^{i\omega t} dt. \tag{3.11}$$

Heterodyne detection results in a total signal

$$\begin{aligned} S_{total}(\omega) &= \left|\mathbf{e}_{LO}\tilde{\varepsilon}_{LO}(\omega) + i\mathbf{P}_s(\omega)\right|^2 \\ &\propto \left|\mathbf{e}_{LO}\tilde{\varepsilon}_{LO}(\omega) + \mathbf{E}_s(\omega)\right|^2 \\ &= \left(\mathbf{e}_{LO}\tilde{\varepsilon}_{LO}(\omega) + \mathbf{E}_s(\omega)\right)\left(\mathbf{e}^*_{LO}\tilde{\varepsilon}^*_{LO}(\omega) + \mathbf{E}^*_s(\omega)\right) \\ S_{total}(\omega) &= \left|\tilde{\varepsilon}_{LO}(\omega)\right|^2 + i\tilde{\varepsilon}_{LO}\mathbf{e}_{LO}\cdot\mathbf{E}^*_s(\omega) + \tilde{\varepsilon}(\omega)\mathbf{e}^*_{LO}\cdot\mathbf{E}_s(\omega) + \left|E_s(\omega)\right|^2 \end{aligned} \tag{3.12}$$

Working in the pertubative regime, where, as stated before, the emitted signals are much weaker than LO, we can safely ignore the last term in the equation above, $|E_s(\omega)|^2$, which is negligible when compared to $|\tilde{\varepsilon}_{LO}(\omega)|^2$. Since we are only interested in the part of the signal resulting from the interaction between the light pulses and the system response, we subtract the $|\tilde{\varepsilon}_{LO}(\omega)|^2$ term due to the local oscillator, which can be measured independently from the system response, from the total signal in Eq. 3.12. We are thus left with the desired spectroscopic signal to be calculated from the polarization,

$$S_s(\omega) \propto Im\left[\tilde{\varepsilon}^*_{LO}(\omega)\mathbf{e}^*_{LO}\cdot\mathbf{E}_s(\omega)\right]. \tag{3.13}$$

In addition, having full control over the phase of the local oscillator allows phase-sensitive detection of $\mathbf{E}_s$.

By contrast, in a homodyne detection experiment, the spectroscopic signal measured is the intensity I_s, which is proportional to E_s^2. We thus lose any of the information related to the phase of the polarization $\mathbf{P}_s$ in a homodyne detection scheme.

We have thus shown how, given a known system's Hamiltonian H_0, dipole operator $\boldsymbol{\mu}$ and light pulses $\mathbf{E}(t)$, we can in theory compute a desired signal, using the system's macroscopic polarization $\mathbf{P}$. From a theoretical approach, we first need to obtain an expression for $\mathbf{P}$, which is given by calculating the expectation value of the dipole operator,

$$\mathbf{P}(\mathbf{r},t) = \langle\boldsymbol{\mu}\rangle \equiv \langle\psi(t)|\,\boldsymbol{\mu}\,|\psi(t)\rangle \tag{3.14}$$

In order to get $\mathbf{P}(\mathbf{r},t)$, we must first solve Eq. 3.6 to get an expression for the system's wavefunction after its interaction with the electric fields, $|\psi(t)\rangle$. Solving for the full wavefunction often being prohibitive, we instead do a standard perturbative expansion of the wavefunction in powers of the electric field $E(t)$, which will be elaborated in Sec. 3.2.1 below,

$$|\psi(t)\rangle = \left|\psi^{(0)}(t)\right\rangle + \left|\psi^{(1)}(t)\right\rangle + \left|\psi^{(2)}(t)\right\rangle ... \tag{3.15}$$

Inserting Eq. 3.15 into Eq. 3.14, we obtain

$$\begin{aligned}\mathbf{P}(\mathbf{r},t) &= \left\langle \psi^{(0)}(t)+\psi^{(1)}(t)+\psi^{(2)}(t)... \right| \boldsymbol{\mu} \left| \psi^{(0)}(t)+\psi^{(1)}(t)+\psi^{(2)}(t)... \right\rangle \\ &= \left\langle \psi^{(0)}(t) \right| \boldsymbol{\mu} \left| \psi^{(0)}(t) \right\rangle + \left\langle \psi^{(0)}(t) \right| \boldsymbol{\mu} \left| \psi^{(1)}(t) \right\rangle + \left\langle \psi^{(1)}(t) \right| \boldsymbol{\mu} \left| \psi^{(0)}(t) \right\rangle + \left\langle \psi^{(0)}(t) \right| \boldsymbol{\mu} \left| \psi^{(2)}(t) \right\rangle + \left\langle \psi^{(2)}(t) \right| \boldsymbol{\mu} \left| \psi^{(0)}(t) \right\rangle + ...\end{aligned}$$

Regrouping terms of equal order together yields the familiar perturbative expansion of the polarization as powers of the electric field amplitudes

$$\mathbf{P}(\mathbf{r},t) = \mathbf{P}^{(0)}(t) + \mathbf{P}^{(1)}(t) + \mathbf{P}^{(2)}(t) + \mathbf{P}^{(3)}(t) + ... \tag{3.16}$$

So far, our discussion has been focused on closed systems. However, a general equation of the form of Eq. 3.16 can be obtained for open systems as well, from a perturbative expansion of the system's density matrix rather than its wavefunction, in much the same way as for a closed system. In the case of open systems, the system's density matrix evolves in time according to the quantum Liouville equation (see Sec. 2.2),

$$\frac{d\rho(t)}{dt} = \mathcal{L}_0\rho(t),$$

where we assume that the system's Liouvillian can contain a dissipative part, absent from a closed system treatment; otherwise, the use of density matrix formalism is unnecessary and we can use wavefunctions. The interaction of the system with the electric fields is again taken to be within the electric dipole approximation, $H'(t) = -\boldsymbol{\mu}\cdot\mathbf{E}(t)$, leading to the interaction Liouvillian

$$-\frac{i}{\hbar}[H'(t),\rho(t)] = \mathcal{L}'(t)\rho(t),$$

The equation of motion then becomes

$$\frac{d\rho(t)}{dt} = \mathcal{L}\rho(t) + \mathcal{L}'\rho(t). \tag{3.17}$$

Using the same assumption that the light emitted from the sample after the interaction with the incident fields is weak, we can calculate the bulk polarization $\mathbf{P}$ of the sytem from the expectation value of the dipole operator, which is defined for open systems as

$$\mathbf{P}(\mathbf{r},t) = \langle\boldsymbol{\mu}\rho(t)\rangle \equiv \mathrm{Tr}\{\boldsymbol{\mu}\rho(t)\}. \tag{3.18}$$

A perturbative expansion of the density matrix of the form

$$\rho(t) = \rho^{(0)}(t) + \rho^{(1)}(t) + \rho^{(2)}(t)... \tag{3.19}$$

leads to the same expansion of the polarization in powers of the incident electric fields, Eq. 3.16.

Substituting an n^{th}-order wavefunction (closed system) or n^{th}-order density matrix (open system) in the defi-

nition of $\mathbf{P}(\mathbf{r},t)$ (Eq. 3.14 for the wavefunction and Eq. 3.18 for the density matrix) therefore allows one to obtain the n^{th}-order polarization, $\mathbf{P}^{(n)}(t)$. This $\mathbf{P}^{(n)}(t)$ in turn allows us to calculate any n^{th} order spectroscopic signal.

This chapter will first describe how to obtain useful, computationally tractable expressions for both $\left|\psi^{(n)}(t)\right\rangle$ and $\rho^{(n)}(t)$, using time-dependent perturbation theory. We then apply these results to 1^{st}-order and 3^{rd}-order signals example and show commonly used approximations within the field of nonlinear optical spectroscopies. Lastly, we introduce Feynman diagrams in the context of NLOSs.

3.2 Perturbative expansion of the wavefunction and density matrix

3.2.1 Wavefunction expansion

The first step of the perturbative expansion for wavefunctions of Eq. 3.15 begins with the Schrödinger equation, Eq. 3.4, before any interaction with light:

$$\frac{d\left|\psi(t)\right\rangle}{dt} = -\frac{i}{\hbar}H_0\left|\psi(t)\right\rangle .$$

We define the time-evolution operator $U_0(t,t_0) = U_0(t-t_0)$, the operator bringing the state $|\psi\rangle$ from a time t_0 to time t,

$$\left|\psi(t)\right\rangle = U_0(t,t_0)\left|\psi(t_0)\right\rangle . \tag{3.20}$$

This operator also has the useful two properties of time-reversal and composition respectively:

$$U_0^{-1}(t,t_0) = U_0(t_0,t)\ ; \tag{3.21}$$

$$U_0(t_2,t_1)U_0(t_1,t_0) = U_0(t_2,t_1). \tag{3.22}$$

We also define the state $|\psi_I(t)\rangle$ in the interaction picture (as opposed to the Schrödinger picture) such that

$$\left|\psi(t)\right\rangle = U_0(t,t_0)\left|\psi_I(t)\right\rangle . \tag{3.23}$$

Substituting the term on the left-hand side of Eq. 3.20 into the Schrödinger equation above, we obtain

$$\frac{\partial\left(U_0(t,t_0)\left|\psi(t_0)\right\rangle\right)}{\partial t} = -\frac{i}{\hbar}H_0(t)\left(U_0(t,t_0)\left|\psi(t_0)\right\rangle\right) .$$

Since the initial state $|\psi(t_0)\rangle$ is an arbitrary state independent of the time variable t, we then have

$$\left(\frac{\partial U_0(t,t_0)}{\partial t}\right)\left|\psi(t_0)\right\rangle = \left(-\frac{i}{\hbar}H_0(t)U_0(t,t_0)\right)\left|\psi(t_0)\right\rangle .$$

This then implies the following

$$\frac{\partial U_0(t,t_0)}{\partial t} = -\frac{i}{\hbar} H_0(t) U_0(t,t_0). \tag{3.24}$$

Inserting Eq. 3.23 into Eq. 3.6, we have

$$\frac{\partial (U_0(t,t_0)\,|\psi_I(t)\rangle)}{\partial t} = -\frac{i}{\hbar} H_0(t)\,(U_0(t,t_0)\,|\psi_I(t)\rangle) - \frac{i}{\hbar} H'(t)\,(U_0(t,t_0)\,|\psi_I(t)\rangle)\,,$$

thus implying

$$\left(\frac{\partial U_0(t,t_0)}{\partial t}\right)|\psi_I(t)\rangle + U_0(t,t_0)\left(\frac{\partial\,|\psi_I(t)\rangle}{\partial t}\right) = -\frac{i}{\hbar}\,(H_0(t)U_0(t,t_0))\,|\psi_I(t)\rangle - \frac{i}{\hbar}\,(H'(t)U_0(t,t_0))\,|\psi_I(t)\rangle\,.$$

Putting Eq. 3.24 into the LHS of the above equation, we now get

$$\cancel{-\frac{i}{\hbar} H_0(t)U_0(t,t_0)\,|\psi_I(t)\rangle} + U_0(t,t_0)\left(\frac{\partial\,|\psi_I(t)\rangle}{\partial t}\right) = \cancel{-\frac{i}{\hbar} H_0(t)U_0(t,t_0)\,|\psi_I(t)\rangle} - \frac{i}{\hbar}\,(H'(t)U_0(t,t_0))\,|\psi_I(t)\rangle\,,$$

leading to

$$U_0(t,t_0)\left(\frac{\partial\,|\psi_I(t)\rangle}{\partial t}\right) = -\frac{i}{\hbar}\,(H'(t)U_0(t,t_0))\,|\psi_I(t)\rangle\,.$$

Multiplying both sides of the equation by the inverse time-evolution operator $U_0^{-1}(t,t_0)$,

$$\frac{\partial\,|\psi_I(t)\rangle}{\partial t} = -\frac{i}{\hbar}\left(U_0^{-1}(t,t_0)H'(t)U_0(t,t_0)\right)|\psi_I(t)\rangle\,.$$

We now integrate on both sides, from t_0 to t:

$$\int_{t_0}^{t} \frac{\partial\,|\psi_I(\tau)\rangle}{\partial \tau} d\tau = \int_{t_0}^{t} -\frac{i}{\hbar} U_0^{-1}(\tau,t_0)H'(\tau)U_0(\tau,t_0)\,|\psi_I(\tau)\rangle\,d\tau.$$

Using Leibniz's integral formula for the LHS, we have

$$|\psi_I(t)\rangle - |\psi_I(t_0)\rangle = \int_{t_0}^{t} -\frac{i}{\hbar} U_0^{-1}(\tau,t_0)H'(\tau)U_0(\tau,t_0)\,|\psi_I(\tau)\rangle\,d\tau,$$

and thus

$$|\psi_I(t)\rangle = |\psi_I(t_0)\rangle + \int_{t_0}^{t} -\frac{i}{\hbar} U_0^{-1}(\tau,t_0)H'(\tau)U_0(\tau,t_0)\,|\psi_I(\tau)\rangle\,d\tau. \tag{3.25}$$

Substituting the expression $|\psi_I(t)\rangle$ for $|\psi_I(\tau)\rangle$ in the integral on the right-hand side of Eq. 3.25 iteratively, we obtain a solution of the form

$$|\psi_I(t)\rangle = |\psi_I(t_0)\rangle + \sum_{n=1}^{\infty} \left(-\frac{i}{\hbar}\right)^n \int_{t_0}^{t} d\tau_n \int_{t_0}^{\tau_n} d\tau_{n-1} ... \int_{t_0}^{\tau_2} d\tau_1 U_0^{-1}(\tau_n, t_0) H'(\tau_n) U_0(\tau_n, t_0) ... U_0^{-1}(\tau_1, t_0) H'(\tau_1) U_0(\tau_1, t_0) |\psi_I(t_0)\rangle .$$

This solution can be readily expressed as a perturbation series

$$|\psi_I(t)\rangle = \left|\psi_I^{(0)}(t)\right\rangle + \left|\psi_I^{(1)}(t)\right\rangle + \left|\psi_I^{(2)}(t)\right\rangle + ...$$

where the n^{th}-order term can be expressed as a function of the $(n-1)^{\text{th}}$ order term,

$$\left|\psi_I^{(n)}(t)\right\rangle = -\frac{i}{\hbar} \int_{t_0}^{t} \left(U_0^{-1}(\tau, t_0) H'(\tau) U_0(\tau, t_0) \left|\psi_I^{(n-1)}(\tau)\right\rangle \right) d\tau.$$

We can make use of Eq. 3.23 (which implies $U_0^{-1}(t, t_0)|\psi(t)\rangle = |\psi_I(t)\rangle$) to obtain the wavefunctions in the Schrödinger picture,

$$U_0^{-1}(t, t_0) \left|\psi^{(n)}(t)\right\rangle = -\frac{i}{\hbar} \int_{t_0}^{t} \left(U_0^{-1}(\tau, t_0) H'(\tau) \left|\psi^{(n-1)}(\tau)\right\rangle \right) d\tau,$$

and multiply both sides by $U_0(t, t_0)$ to get

$$\left|\psi^{(n)}(t)\right\rangle = -\frac{i}{\hbar} U_0(t, t_0) \int_{t_0}^{t} U_0^{-1}(\tau, t_0) H'(\tau) \left|\psi^{(n-1)}(\tau)\right\rangle d\tau.$$

Defining the integration variable τ as $t - t'$ yields

$$\begin{aligned} \left|\psi^{(n)}(t)\right\rangle &= \frac{i}{\hbar} U_0(t, t_0) \int_{t-t_0}^{0} U_0^{-1}(t - t', t_0) H'(t - t') \left|\psi^{(n-1)}(t - t')\right\rangle dt' \\ &= -\frac{i}{\hbar} U_0(t, t_0) \int_{0}^{t-t_0} U_0^{-1}(t - t', t_0) H'(t - t') \left|\psi^{(n-1)}(t - t')\right\rangle dt'. \end{aligned}$$

Using the decompostion $U_0(t, t_0) = U_0(t, 0) U_0(0, t_0)$ and the time-reversal property $U_0^{-1}(t - t', t_0) = U_0(t_0, t - t')$, we arrive at

$$\begin{aligned} \left|\psi^{(n)}(t)\right\rangle &= -\frac{i}{\hbar} U_0(t, 0) \int_{0}^{t-t_0} U_0(0, t - t') H'(t - t') \left|\psi^{(n-1)}(t - t')\right\rangle dt' \\ &= -\frac{i}{\hbar} U_0(t, 0) \int_{0}^{t-t_0} U_0^{-1}(t - t', 0) H'(t - t') \left|\psi^{(n-1)}(t - t')\right\rangle dt'. \end{aligned}$$

Finally, we assume that the 0^{th}-order unperturbed state $\left|\psi^{(0)}(t_0)\right\rangle$ is a stationary state of Eq. 3.4, meaning it does not evolve in time when subject to H_0. This assumption implies that $\psi^{(0)}(t_0) = \psi^{(0)}(-\infty)$, which in turn allows to

send $t_0 \to -\infty$ and finally obtain

$$\left|\psi^{(n)}(t)\right\rangle = -\frac{i}{\hbar}U_0(t,0)\int_0^\infty U_0^{-1}(t-t',0)H'(t-t')\left|\psi^{(n-1)}(t-t')\right\rangle dt'. \tag{3.26}$$

3.2.2 Density matrix expansion

The perturbative expansion derivation of the density matrix for open systems follows the same steps as the derivation for the wavefunction for closed systems, and so we only cover it in broad strokes. We start with the Liouville equation

$$\frac{d\rho(t)}{dt} = -\frac{i}{\hbar}[H_0(t),\rho(t)] + D\rho(t) - \frac{i}{\hbar}[H'(t),\rho(t)], \tag{3.27}$$

where D is the dissipation superoperator, modelling dephasing and relaxation processes. Its specific form is covered in Chapter 2, using Redfield theory. We respectively define the system and interaction Liouvillian superoperators acting on the density matrix as

$$\mathcal{L}_0\rho(t) = -\frac{i}{\hbar}[H_0(t),\rho(t)] + D\rho(t)\ ;$$

$$\mathcal{L}'\rho(t) = -\frac{i}{\hbar}[H'(t),\rho(t)],$$

and obtain the following compact version of Eq. 3.27

$$\frac{d\rho}{dt} = \mathcal{L}_0\rho(t) + \mathcal{L}'\rho(t). \tag{3.28}$$

We again define a time-evolution operator acting on the density matrix, denoted $\mathcal{T}_0(t,t_0)$ such that

$$\rho(t) = \mathcal{T}_0(t,t_0)\rho(t_0), \tag{3.29}$$

with the same properties of time-reversal and composition as that of Eqs. 3.21 and 3.22. Once again, inserting Eq. 3.29 into Eq. 3.28 and following the same procedure as for the wavefunction, we arrive at

$$\frac{\partial\mathcal{T}_0(t,t_0)}{\partial t} = \mathcal{L}_0(t)\mathcal{T}_0(t,t_0). \tag{3.30}$$

Defining the interaction picture density matrix $\rho_I(t)$ such that

$$\rho(t) = \mathcal{T}_0(t,t_0)\rho_I(t), \tag{3.31}$$

and following the same steps as in Sec. 3.2.1, we obtain the analogue of Eq. 3.25 for the density matrix in the interaction picture :

$$\rho_I(t) = \rho_I(t_0) + \int_{t_0}^{t} \mathcal{T}_0^{-1}(\tau, t_0)\mathcal{L}'(\tau)\mathcal{T}_0(t, t_0)\rho_I(\tau)d\tau, \tag{3.32}$$

where again, iteratively inserting the integral definition of $\rho_I(t)$ into the term $\rho_I(\tau)$ in Eq. 3.32, we have the infinite sum

$$\rho_I(t) = \rho_I(t_0) + \sum_{n=1}^{\infty} \int d\tau_n \int_{t_0}^{\tau_n} d\tau_{n-1} ... \int_{t_0}^{\tau_1} d\tau_1 \left(\mathcal{T}_0^{-1}(\tau_n, t_0)\mathcal{L}'(\tau_n)\mathcal{T}_0(\tau_n, t_0)\right) ... \left(\mathcal{T}_0^{-1}(\tau_1, t_0)\mathcal{L}'(\tau_1)\mathcal{T}_0(\tau_1, t_0)\right),$$

which we express as the desired perturbation series

$$\rho_I(t) = \rho_I^{(0)}(t) + \rho_I^{(1)}(t) + \rho_I^{(2)}(t) + ...$$

We then have the n^{th}-order density matrix given by

$$\rho_I^{(n)}(t) = \int_{t_0}^{t} \mathcal{T}_0^{-1}(\tau, t_0)\mathcal{L}'(\tau_n)\mathcal{T}_0(\tau, t_0)\rho_I^{(n)}(t)d\tau,$$

where, multiplying both sides of the above equation by $\mathcal{T}_0(t, t_0)$, defining $\tau = t - t'$ and using the time-reversal and composition properties of $\mathcal{T}_0(t, t_0)$, we obtain the density matrix in the Schrödinger picture,

$$\rho^{(n)}(t) = \mathcal{T}_0(t, 0) \int_0^{t-t_0} \mathcal{T}_0^{-1}(t - t', 0)\mathcal{L}'(t - t')\rho^{(n-1)}(t - t')dt'.$$

Assuming that $\rho(t_0)$ is an equilibrium density matrix, meaning $\rho(-\infty) = \rho(t_0)$, we are free to impose $t_0 \to -\infty$ and arrive at the final form

$$\rho^{(n)}(t) = \mathcal{T}_0(t, 0) \int_0^{\infty} \mathcal{T}_0^{-1}(t - t', 0)\mathcal{L}'(t - t')\rho^{(n-1)}(t - t')dt'. \tag{3.33}$$

3.3 Application to first and third order polarizations

Using Eqs. 3.26 or 3.33, we can now use those expressions to show how the perturbative approach allows us to calculate the simplest signal in absorption spectroscopy, linear absorption. Linear absorption is proportional to the 1^{st} order polarization $\mathbf{P}^{(1)}(t)$, which, for a closed system, is

$$\mathbf{P}^{(1)}(t) = \left\langle \psi^{(1)}(t) \right| \boldsymbol{\mu} \left| \psi^{(0)}(t) \right\rangle + c.c. \tag{3.34}$$

The interaction with the system in this case comes from a single pulse, which for simplicity we assume to be linearly polarized along the x-axis only, such that its electric field can be written as

$$\mathbf{E}(t) = \mathbf{e}_x \varepsilon_p(t-t') + \mathbf{e}_x^* \varepsilon_p^*(t-t'), \tag{3.35}$$

with the pulse amplitude $\varepsilon_p(t-t')$ being

$$\varepsilon_p(t-t') = A_p(t-t') e^{-i(\omega_p(t-t') - \mathbf{k}_p \cdot \mathbf{r} + \phi_p)}, \tag{3.36}$$

with $\mathbf{k}_p = \mathbf{k}_x$, and the interaction Hamiltonian $H'(t)$ is, given $\boldsymbol{\mu} = \mu_x = \mu$ (since the dot product in Eq. 3.37 would yield 0 otherwise given the polarization of $\mathbf{E}(t)$ in Eq. 3.35) ,

$$\begin{aligned} H'(t) &= -\boldsymbol{\mu} \cdot \mathbf{E}(t) \\ &= -\mu \varepsilon_p(t-t') - \mu \varepsilon_p^*(t-t'). \end{aligned} \tag{3.37}$$

Using Eq. 3.26, we have that the first order wavefunction is, with the explicit form of Eq. 3.37 for $H'(t)$,

$$\begin{aligned} \left|\psi^{(1)}(t)\right\rangle &= -\frac{i}{\hbar} U_0(t,0) \int_0^\infty U_0^{-1}(t-t',0)(-\mu\varepsilon_p(t-t') - \mu\varepsilon_p^*(t-t')) \left|\psi^{(0)}(t-t')\right\rangle dt' \\ &= \frac{i}{\hbar} U_0(t,0) \int_0^\infty \varepsilon_p(t-t') U_0^{-1}(t-t',0)\mu \left|\psi^{(0)}(t-t')\right\rangle dt' + \frac{i}{\hbar} U_0(t,0) \int_0^\infty \varepsilon_p^*(t-t') U_0^{-1}(t-t',0)\mu \left|\psi^{(0)}(t-t')\right\rangle dt'. \end{aligned}$$

Inserting the definition of the pulse amplitude Eq. 3.36 into the equation yields, after factorization,

$$\begin{aligned} \left|\psi^{(1)}(t)\right\rangle = \frac{i}{\hbar} U_0(t,0) e^{i(\mathbf{k}_p \cdot \mathbf{r} + \phi_p)} \left(\int_0^\infty A_p(t-t') e^{-i\omega_p(t-t')} U_0^{-1}(t-t',0)\mu \left|\psi^{(0)}(t-t')\right\rangle dt' \right) \\ + \frac{i}{\hbar} U_0(t,0) e^{i(\mathbf{k}_p \cdot \mathbf{r} + \phi_p)} \left(\int_0^\infty A_p(t-t') e^{i\omega_p(t-t')} U_0^{-1}(t-t',0)\mu \left|\psi^{(0)}(t-t')\right\rangle dt' \right). \end{aligned} \tag{3.38}$$

The two integrals above are nearly identical, save for the sign of the phase factor $e^{i\omega_p(t-t')}$. Making use of the rotating-wave approximation (RWA, see Appendix **??** for its derivation for both closed and open systems), the second term can be safely neglected, further simplifying our calculations.

We are thus left with a single remaining term from Eq. 3.38,

$$\begin{aligned} \left|\psi^{(1)}(t)\right\rangle &\approx \frac{i}{\hbar} U_0(t,0) e^{i(\mathbf{k}_p \cdot \mathbf{r} + \phi_p)} \left(\int_0^\infty A_p(t-t') e^{-i\omega_p(t-t')} U_0^{-1}(t-t',0)\mu \left|\psi^{(0)}(t-t')\right\rangle dt' \right), \\ &= e^{i(\mathbf{k}_p \cdot \mathbf{r} + \phi_p)} \int_0^\infty A_p(t-t') e^{-i\omega_p(t-t')} \frac{i}{\hbar} U_0(t',0)\mu \left|\psi^{(0)}(t-t')\right\rangle dt' \end{aligned}$$

from which we compute the linear polarization using Eq. 3.34,

$$P^{(1)}(t) = e^{i(\mathbf{k}_p\cdot\mathbf{r}+\phi_p)}\int_0^\infty A_p(t-t')e^{i(\mathbf{k}_p\cdot\mathbf{r}+\phi_p)}e^{-i\omega_p(t-t')}\left(\frac{i}{\hbar}\left\langle\mu\right|U_0(t',0)\mu\left|\psi^{(0)}\right\rangle\right)dt' + c.c.$$

The polarization must only depend on the electric field of the pulse at times earlier than t. Were the integration bounds in the equation above different, it would imply that the polarization, which is induced by the interaction with the pulse, could be present even before the light-matter interaction, which is of course impossible according to the causality principle. By inserting $\theta(t')$, the Heaviside step function, in the integral, we are free to take the limit as $t' \to -\infty$ for the lower bound of the integral, leading to

$$P^{(1)}(t) = e^{i(\mathbf{k}_p\cdot\mathbf{r}+\phi_p)}\int_{-\infty}^\infty A_p(t-t')e^{-i\omega_p(t-t')}\left(\frac{i}{\hbar}\theta(t')\left\langle\mu\right|U_0(t',0)\mu\left|\psi^{(0)}\right\rangle\right)dt' + c.c. \tag{3.39}$$

The factor $e^{i(\mathbf{k}_p\cdot\mathbf{r}+\phi_p)}$ in the equation above encodes all the relevant information about the direction of the emitted signal; it is the phase-matching direction of the linear signal. Thus, the linear absorption signal $E_s^{(1)}(t) \propto iP^{(1)}(t)$ will be emitted in the $\mathbf{k}_p$ direction, the same direction of propagation as that of the light pulse, which is precisely what we would expect in an experiment of that nature.

In Eq. 3.39, the separation of the terms related to the material ($\mu, U_0(t',0)$) from the terms related to the optical pulse ($\mathbf{k}_p$,A_p, ω_p, ϕ_p) leads to the optical response function $S(t)$, where in 1$^{\text{st}}$-order it is defined as

$$S^{(1)}(t) = \frac{i}{\hbar}\theta(t)\langle\mu|U_0(t',0)\mu|\psi^{(0)}\rangle \tag{3.40}$$

$S^{(1)}(t)$ is the linear response function of the system, characterizing its physical properties and is independent of any interactions with incident fields. Substituting $S^{(1)}$ in Eq. 3.39, we obtain

$$P^{(1)}(t) = e^{i(\mathbf{k}_p\cdot\mathbf{r}+\phi_p)}\int_{-\infty}^\infty A_p(t-t')e^{-i\omega_p(t-t')}S^{(1)}(t)dt' + c.c.$$

Taking the Fourier transform of $P^{(1)}$, we have

$$P^{(1)}(\omega) = \int_{-\infty}^\infty P^{(1)}(t)e^{i\omega t}dt.$$

The emitted radiation $E_s^{(1)}(t)$ is, as stated before, proportional to $iP^{(1)}(t)$, and thus the signal we obtain from Eq. 3.13 is

$$S_s(\omega) \propto Im\left[\tilde{\varepsilon}_{LO}^*(\omega)\mathbf{e}_{LO}^*\cdot E_s^{(1)}(\omega)\right].$$

Since $E_s^{(1)}(\omega)$ is related to $P^{(1)}(\omega)$ and thus to $S^{(1)}(t)$, we have that the linear absorption signal is, as expected,

related to the linear response properties of the system contained in Eq. 3.40.

For open systems, the procedure is largely the same as for closed systems, with a few differences in notation. Once again using linear absorption as an example with the same electric field described by Eqs. 3.35 and 3.36, we have the 1st-order polarization,

$$\mathbf{P}^{(1)}(t) = \mathrm{Tr}[\mu\rho^{(1)}(t)] \tag{3.41}$$

with

$$|\rho^{(1)}(t)\rangle\rangle = \mathcal{T}_0(t,0)\int_0^\infty \mathcal{T}_0^{-1}(t-t',0)\mathcal{L}'(t-t')|\rho^{(0)}\rangle\rangle dt',$$

where $|\rho\rangle\rangle$ is a Liouville-space vector. Writing out the interaction Liouvillian, remembering that the electric field of the pulse is linearly polarized in a single direction, we have

$$\mathcal{L}'(t) = -\frac{i}{\hbar}\left(\mu^K E(t) - \frac{i}{\hbar}\mu^B E(t)\right), \tag{3.42}$$

with the dipole superoperators denoting either an action on the ket side ($\mu^K|\rho\rangle\rangle = \mu\rho$) or the bra side ($\mu^B|\rho\rangle\rangle = \rho\mu$) of the density matrix. We obtain the 1st-order density matrix

$$\begin{aligned}
|\rho^{(1)}(t)\rangle\rangle &= \mathcal{T}_0(t,0)\int_0^\infty \mathcal{T}_0^{-1}(t-t',0)\left(-\frac{i}{\hbar}\mu^K E(t) + \frac{i}{\hbar}\mu^B E(t)\right)|\rho^{(0)}\rangle\rangle dt' \\
&= \mathcal{T}_0(t,0)\int_0^\infty \mathcal{T}_0^{-1}(t-t',0)\left(-\frac{i}{\hbar}\mu^K(\varepsilon_p(t-t') + \varepsilon_p^*(t-t')) + \frac{i}{\hbar}\mu^B(\varepsilon_p(t-t') + \varepsilon_p^*(t-t'))\right)|\rho^{(0)}\rangle\rangle dt'
\end{aligned}$$

Regrouping terms by pulse amplitudes, we get

$$|\rho^1(t)\rangle\rangle = \frac{i}{\hbar}\mathcal{T}_0(t,0)\int_0^\infty \mathcal{T}_0^{-1}(t-t',0)\left(\varepsilon_p(t-t')\left(\mu^K|\rho^{(0)}(t)\rangle\rangle - \mu^B|\rho^{(0)}\rangle\rangle\right)dt' - \varepsilon_p^*(t-t')\left(\mu^K|\rho^{(0)}(t)\rangle\rangle - \mu^B|\rho^{(0)}\rangle\rangle\right)\right)dt'$$

Making use of the RWA, we can ignore two terms : $\varepsilon_p(t-t')\mu^B|\rho^{(0)}(t)\rangle\rangle$, the de-excitation of the ground state bra, and $\varepsilon_p^*(t-t')\mu^K|\rho^{(0)}\rangle\rangle$, the de-excitation of the ground state ket. We are then left with

$$\begin{aligned}
|\rho^{(1)}(t)\rangle\rangle &\approx \frac{i}{\hbar}\mathcal{T}_0(t,0)\int_0^\infty \mathcal{T}_0^{-1}(t-t',0)\left(\varepsilon_p(t-t')\left(\mu^K|\rho^{(0)}\rangle\rangle\right)dt' + \varepsilon_p^*(t-t')\left(\mu^B|\rho^{(0)}\rangle\rangle\right)\right)dt' \\
&= \frac{i}{\hbar}\mathcal{T}_0(t,0)\int_0^\infty \mathcal{T}_0^{-1}(t-t',0)\varepsilon_p(t-t')\mu^K|\rho^{(0)}\rangle\rangle dt' + h.c. \\
&= \int_0^\infty \varepsilon_p(t-t')\left(\frac{i}{\hbar}\mathcal{T}_0(t',0)\mu^K|\rho^{(0)}\rangle\rangle\right)dt' + h.c.
\end{aligned}$$

Finally, the polarization is

$$\begin{aligned} P^{(1)}(t) &= \langle \mu \rho^{(1)}(t) \rangle \\ &= \int_0^\infty \varepsilon_p(t-t') \left(\frac{i}{\hbar} \theta(t') \langle\langle \mu | \mathcal{T}_0(t',0) \mu^K | \rho^{(0)} \rangle\rangle \right) dt' + h.c. \qquad (3.43) \\ &= e^{i(\mathbf{k}_p \cdot \mathbf{r} + \phi_p)} \int_{-\infty}^\infty A_p(t-t') e^{-i\omega_p(t-t')} \left(\frac{i}{\hbar} \theta(t') \langle\langle \mu | \mathcal{T}_0(t',0) \mu^K | \rho^{(0)} \rangle\rangle \right) dt' + c.c \\ &= e^{i(\mathbf{k}_p \cdot \mathbf{r} + \phi_p)} \int_{-\infty}^\infty A_p(t-t') e^{-i\omega_p(t-t')} S^{(1)}(t) dt' + c.c \qquad (3.44) \end{aligned}$$

The result in Eq. 3.44 is essentially the same as that for a closed system, Eq. 3.39, save for the different expressions for the linear optical response function $S^{(1)}(t)$. Taking the Fourier transform of Eq. 3.44 and using Eq. 3.13, we would once again obtain the linear absorption spectrum of the system.

We now look at at a general 3$^{\text{rd}}$-order example applied to an open system, where the incident electric field $E(t)$ is now the sum of 3 different pulses E_1, E_2, E_3, whose arrival times t_1, t_2, t_3 are for now assumed to be all different. The resulting polarization $P^{(3)}(t)$ is then, not expanding the electric field

$$P^{(3)}(t) = \int dt_3 \int dt_2 \int dt_1 E_1(t - t_3 - t_2 - t_1) E_2(t - t_3 - t_2) E_3(t - t_3) S^{(3)}(t_1, t_2, t_3). \qquad (3.45)$$

The third-order optical response function $S^{(3)}$ is defined as

$$S^{(3)}(t_1, t_2, t_3) = \left(\frac{i}{\hbar} \right)^3 \theta(t_3)\theta(t_2)\theta(t_1) \sum_{\alpha, \alpha', \alpha'' = K, B} \langle\langle \mu | \mathcal{T}_0(t_3, t_2) \mu^{\alpha''} \mathcal{T}_0(t_2, t_1) \mu^{\alpha'} \mathcal{T}_0(t_1, 0) \mu^{\alpha} | \rho^{(0)} \rangle\rangle \qquad (3.46)$$

There are $2^3 = 8$ terms in the sum of Eq. 3.46, since either $\mu^\alpha = \mu^K$ or $\mu^\alpha = \mu^B$ for each $\alpha, \alpha', \alpha''$. Half of those terms are complex conjugates of the others. Four of those terms are [2]

$$S_1^{(3)}(t_1, t_2, t_3) = \left(\frac{i}{\hbar} \right)^3 \theta(t_3)\theta(t_2)\theta(t_1) \langle\langle \mu | \mathcal{T}_0(t_3, t_2) \mu^K \mathcal{T}_0(t_2, t_1) \mu^K \mathcal{T}_0(t_1, 0) \mu^K | \rho^{(0)} \rangle\rangle,$$

$$S_2^{(3)}(t_1, t_2, t_3) = \left(\frac{i}{\hbar} \right)^3 \theta(t_3)\theta(t_2)\theta(t_1) \langle\langle \mu | \mathcal{T}_0(t_3, t_2) \mu^B \mathcal{T}_0(t_2, t_1) \mu^B \mathcal{T}_0(t_1, 0) \mu^K | \rho^{(0)} \rangle\rangle,$$

$$S_3^{(3)}(t_1, t_2, t_3) = \left(\frac{i}{\hbar} \right)^3 \theta(t_3)\theta(t_2)\theta(t_1) \langle\langle \mu | \mathcal{T}_0(t_3, t_2) \mu^K \mathcal{T}_0(t_2, t_1) \mu^B \mathcal{T}_0(t_1, 0) \mu^B | \rho^{(0)} \rangle\rangle,$$

$$S_4^{(3)}(t_1, t_2, t_3) = \left(\frac{i}{\hbar} \right)^3 \theta(t_3)\theta(t_2)\theta(t_1) \langle\langle \mu | \mathcal{T}_0(t_3, t_2) \mu^B \mathcal{T}_0(t_2, t_1) \mu^K \mathcal{T}_0(t_1, 0) \mu^B | \rho^{(0)} \rangle\rangle,$$

with the complex conjugate of S_4 being for example

$$S_4^{*(3)}(t_1, t_2, t_3) = \left(\frac{i}{\hbar} \right)^3 \theta(t_3)\theta(t_2)\theta(t_1) \langle\langle \mu | \mathcal{T}_0(t_3, t_2) \mu^K \mathcal{T}_0(t_2, t_1) \mu^B \mathcal{T}_0(t_1, 0) \mu^K | \rho^{(0)} \rangle\rangle.$$

The 3rd-order polarization in Eq. 3.45 contains all the information necessary for the calculation of any 3rd-order signal. There are 6 electric field terms (one rotating ε_j and one counter-rotating term ε_j^* for each pulse E_1, E_2, E_3) in Eq. 3.45. Combining this with the 8 possible optical response functions leads to a total of $6^3 \cdot 8 = 1728$ different terms to calculate to obtain the full $P^{(3)}$. However, we are generally interested in only a subset of all the possible polarizations in $P^{(3)}$. If, for example, we wish to obtain only the signal radiated in the $\mathbf{k}_s = \mathbf{k}_1 - \mathbf{k}_2 + \mathbf{k}_3$ direction, then we must only concern ourselves with the terms in $P^{(3)}$ which contain the prefactors of form $e^{i((\mathbf{k}_1-\mathbf{k}_2+\mathbf{k}_3)\cdot\mathbf{r}+\phi_1-\phi_2+\phi_3)}$. Each ε_j carries a wavevector $+\mathbf{k}_j$ while the ε_j^* carry a $-\mathbf{k}_j$ wavevector, meaning we are only calculating the contributions of $P^{(3)}$ with the product $\varepsilon_1\varepsilon_2^*\varepsilon_3$ and can for example neglect contributions with the product $\varepsilon_1\varepsilon_2\varepsilon_3$. We are left in this case with any term in Eq. 3.45 that corresponds to the phase-matching condition $\mathbf{k}_s = \mathbf{k}_1 - \mathbf{k}_2 + \mathbf{k}_3$, leading to

$$P^{(3)}_{\mathbf{k}_s} = \int dt_3 \int dt_2 \int dt_1 \varepsilon_3(t-t_3)\varepsilon_2^*(t-t_3-t_2)\varepsilon_1(t-t_3-t_2-t_1)S^{(3)}(t_1,t_2,t_3). \tag{3.47}$$

Furthermore, within the RWA, some additional terms may be neglected. We can take as an example the contributions to $P^{(3)}_{\mathbf{k}_s}$ originating from S_4 and its complex conjugate S_4^* ,

$$\begin{aligned} S_4 = &\int dt_3 \int dt_2 \int dt_1 \varepsilon_3(t-t_3)\varepsilon_2^*(t-t_3-t_2)\varepsilon_1(t-t_3-t_2-t_1) \\ &\left(\frac{i}{\hbar}\right)^3 \theta(t_3)\theta(t_2)\theta(t_1)\langle\langle \mu|\mathcal{T}_0(t_3,t_2)\mu^B\mathcal{T}_0(t_2,t_1)\mu^K\mathcal{T}_0(t_1,0)\mu^B|\rho^{(0)}\rangle\rangle, \end{aligned}$$

and

$$\begin{aligned} S_4^* = &\int dt_3 \int dt_2 \int dt_1 \varepsilon_3(t-t_3)\varepsilon_2^*(t-t_3-t_2)\varepsilon_1(t-t_3-t_2-t_1) \\ &\left(\frac{i}{\hbar}\right)^3 \theta(t_3)\theta(t_2)\theta(t_1)\langle\langle \mu|\mathcal{T}_0(t_3,t_2)\mu^K\mathcal{T}_0(t_2,t_1)\mu^B\mathcal{T}_0(t_1,0)\mu^K|\rho^{(0)}\rangle\rangle. \end{aligned}$$

The first contribution contains the product $\varepsilon_1(t-t_3-t_2-t_1)\mu^B|\rho^{(0)}\rangle\rangle$, representing a de-excitation of the bra side of the density matrix, coming from the interaction with the first pulse. However, since we generally assume that the unperturbed $|\rho^{(0)}\rangle\rangle$ is initially a ground-state density matrix $|0\rangle\langle 0|$, there are no states that can be de-excited under this assumption and thus the integral for this contribution is zero within the RWA. On the other hand, the second contribution has for its first interaction $\varepsilon_1(t-t_3-t_2-t_1)\mu^K|\rho^{(0)}\rangle\rangle$, representing an excitation of the ket side of the density matrix, a second interaction $\varepsilon_2^*(t-t_3-t_2)\mu^B|\rho^{(1)}\rangle\rangle$ (noting that after the first interaction, the density matrix is now perturbed to 1st-order), an excitation of the bra side of $\rho^{(1)}$, and its last interaction $\varepsilon_3(t-t_3)\mu^K|\rho^{(2)}\rangle\rangle$ being similar to the first interaction. Overall, these three interactions combined represent a non-zero contribution to $P^{(3)}_{\mathbf{k}_s}$. A visual representation of this contribution in the form of a double-sided Feynma diagrams (introduced in Sec.3.4) can be seen in the bottom left panel of Fig. 3.3.

Despite using the phase-matching condition to obtain only the $P^{(3)}_{\mathbf{k}_s}$ contribution to $P^{(3)}$, Eq. 3.47 still represents 48 possible different terms that each need to be computed. Using the RWA, this number of terms is now reduced to 16. While computationally calculating each of the 16 convolutions from Eq. 3.47 is not unimaginable, it is still costly. Considering that varying the delay time between each pulse involves in practice calculating each of 16 terms again (if the pulses still overlap), and that that time varying is often done multiple times, the total number of calculations to be carried out rapidly becomes prohibitive. It is thus often convenient to do calculations of 3$^{\text{rd}}$-order and higher nonlinear order polarizations in what is called the *impulsive limit*. In this limit, we assume that all the pulses used are shorter in time than any relevant system dynamics, in which case we can approximate the pulse envelopes A_p in ε_p as delta functions, $A_p(t-t') \approx \delta(t-t')$. Using this approximation, Eq. 3.47 for example becomes

$$\begin{aligned} P^{(3)}_{\mathbf{k}_s} &\approx \int dt_3 \int dt_2 \int dt_1 \delta(t-t_3-t_2-t_1)\delta(t-t_3-t_2)\delta(t-t_3)S^{(3)}(t_1,t_2,t_3) \\ &= e^{i(\mathbf{k}_s\cdot\mathbf{r}+\phi_s)}S^{(3)}(t-t_3-t_2-t_1, t-t_3-t_2, t-t_3) \end{aligned}$$

Hence, ignoring the pulse shape allows us to obtain the nonlinear polarization $P^{(3)}$ of our sample directly from its 3$^{\text{rd}}$-order response function $S^{(3)}$, since both are identical up to a phase. It has been previously demonstrated [27] that ignoring pulse shapes, and additionally, pulse overlaps, where the tail-end of an early pulse overlaps with the front-end of a later pulse, in calculations of NLOSs can lead to significant changes in the computed signals. Whether either impulsive or finite pulse is the right choice for nonlinear spectra calculations depends in part on the system being studied. If the pulses' durations are shorter than all system dynamics, involking the impulsive limit is justified and in addition, makes calculations faster. However, if the pulses are on the same or even longer time scale than some dynamics, the impulsive limit does not hold and the calculated signals are not well approximated [27] using impulsive pulses.

3.4 Feynman diagrams in NLOS

Although the integrals in Eqs. 3.39 and 3.44 (or their higher-order equivalent) ultimately have to be carried out to obtain an n^{th}-order polarization and from there, an n^{th}-order signal with a certain phase-discrimination condition, they are rarely intuitive or easy to read on their own. To get a better sense of what calculations of this sort represent in terms of spectroscopic signals, and perhaps also to organize said calculations, a more visual, diagrammatric approach is desirable. The idea of representing complicated, often notation-heavy integrals graphically naturally leads to the use of Feynman diagrams (FD), which are now ubiquitous in the context of NLOSs. The version of Feynman diagrams as they are used in nonlinear spectroscopy are somewhat different from the diagrams most often seen in the context of particle physics. For NLOSs, Feynman diagrams are either single-sided (SS-FD) for closed systems or double-sided (DS-FD) for open systems. We only cover double-sided diagrams since they are the most

widely used in the field. Below is an example of a DS-FD generated by the Diagram Generator [27] of the Ultrafast Spectroscopy Suite (see Sec. 3.6 below for more details), representing linear absorption.

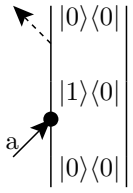

Figure 3.1: Double-sided Feynman diagram for linear absorption

In a diagram, time runs from bottom to top. The left vertical line represents the time evolution of the ket of the density matrix, while the right vertical line represents the evolution of the bra side of the density matrix (and thus, a single vertical line would be used to represent the time evolution of a closed system's wavefunction). Each interaction with a light pulse is represented by an arrow. The RWA leads to a convenient way to interpret each pulse interaction with the system in the diagrams: an up and right pointing arrow represents an interaction with a ε_p term in Eq. 3.1, going in the $+\mathbf{k}_p$ direction, and is called a rotating term. An up and left pointing arrow represents an interaction with a ε_p^* term, going in the $-\mathbf{k}_p$ direction, and is identified as a counter-rotating term. Phrased differently, this means that a rotating term containing ε will excite the ket and de-excite the bra, and a counter-rotating term containing ε^* will de-excite the ket and excite the bra. Each of these arrows is reponsible for the perturbation of the density matrix of the system, leading to a $\rho^{(n)}(t)$ term, given n interactions. Each interaction carries a factor of $\frac{i}{\hbar}$; additionally, each interaction on the bra side carries a minus sign, which can be seen from the negative sign of μ^B in Eq. 3.42. The total sign of a diagram indicates whether it represents a positive or a negative contribution to the overall signal. The last arrow in a diagram, usually represented as a dashed or squiggly arrow, is different in nature from straight arrows, representing an emission of light from the system rather than a light-matter interaction, and thus always points outwards. It represents the emitted polarization $P^{(n)}(t) = \langle \mu \rho^{(n)}(t) \rangle$, from which we calculate the signal corresponding to that particular diagram. By convention, this last arrow is placed on the ket side of the diagram, removing the need to calculate the complex conjugate diagrams where the dashed arrow is on the bra side.

The diagram in Fig. 3.1 represents mathematically the contribution of the term

$$\int_{-\infty}^{\infty} \varepsilon_a \left(\frac{i}{\hbar} \theta(t') \langle\langle \boldsymbol{\mu} | \mathcal{T}_0^{-1}(t', 0) \mu^K | \rho^{(0)} \rangle\rangle \right) dt', \tag{3.48}$$

to the linear polarization $P^{(1)}$ from Eq. 3.44. The first interaction of pulse a with the system corresponds to

$$\varepsilon_a \mu^K | \rho^{(0)} \rangle\rangle$$

where we see that the pulse travelling in the direction $+\mathbf{k}_a$ excites the ket side of the density matrix, yielding the 1^{st}-order perturbed density matrix $\rho^{(1)}$. The outgoing dashed arrow in Fig. 3.1 represents the emitted polarization, which corresponds to $\langle \mu\rho^{(1)}(t)\rangle$, and is precisely the integral in Eq. 3.48. This first example illustrates the procedure of using the Feynman diagram in Fig. 3.1 to represent the hard-to-read expression of Eq. 3.48.

As a second example, we look at the case of transient absorption (TA) spectroscopy. In this setup, we wish to measure the absorption of a probe pulse, labeled b, similarily to linear absorption, with the key difference that the system has first interacted with a pump pulse labeled a. Since we measure the absorption signal in the same direction as the probe pulse $\mathbf{k}_b$, we must have that the signal's wavevector obeys $\mathbf{k}_s = \mathbf{k}_b$. This means that the pulse a must have an equal number of rotating and counter rotating interactions with the system. These interactions will give rise to, in the lowest-order, a 3^{rd}-order polarization (there are in fact 5^{th}-, 7^{th}- and higher-order contributions to the the TA signal and we cover this subject in Sec. 3.5),

$$P^{(3)}(t) = \int dt_b \int dt_a E_a(t - t_b - t_a) E_b(t - t_b) S^{(3)}(t_a, t_b). \tag{3.49}$$

Equation 3.49 is similar to Eq. 3.45, except we now only have two light pulses instead of three.

Assuming the second pulse arrives a long delay time $T = t_b - t_a$ after the first pulse (long when compared to the system's dynamics), two of the possible diagrams representing this scenario are :

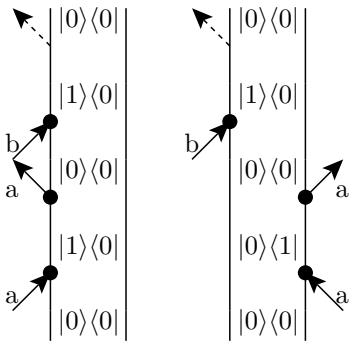

Figure 3.2: Example double-sided Feynman diagrams for transient absorption, under the rotating-wave approximation and obeying the phase matching condition $\mathbf{k}_s = \mathbf{k}_b$. Both diagrams represent the ground state bleach (GSB) contribution to the 3^{rd}-order TA signal.

We see that for the left diagram in Fig. 3.2 that the first interaction with pulse a has a wavevector $-\mathbf{k}_a$, the second interaction a wavevector $+\mathbf{k}_a$ and the final interaction with pulse b has a wavevector $+\mathbf{k}_b$. Thus, we have $\mathbf{k}_s = -\mathbf{k}_a + \mathbf{k}_a + \mathbf{k}_b = \mathbf{k}_b$, which obeys the phase-matching condition previously mentioned. The other possible Feynman diagrams are

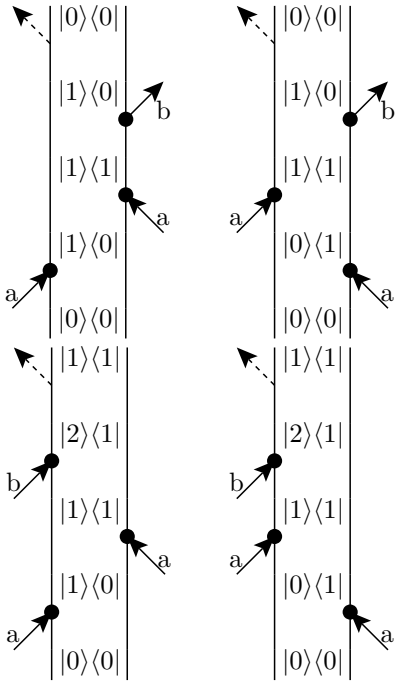

Figure 3.3: Other examples of possible Feynman diagrams for transient absorption spectroscopy. The upper diagrams represent the stimulated emission (SE) contribution to the TA, while the lower diagrams represent the excited state absorption (ESA) contribution.

To further illustrate the RWA, let us imagine we have a simple three-level system, made up of a ground state $|0\rangle$, a singly-excited state $|1\rangle$ and a doubly-excited state $|2\rangle$(see Fig. 3.4 below for an energy level diagram of the system) and let us consider two different DS-FD : the right top and bottom diagrams of Fig. 3.3. In both cases, we assume that the system is initially in the ground state $\rho^{(0)} = |0\rangle\langle 0|$.

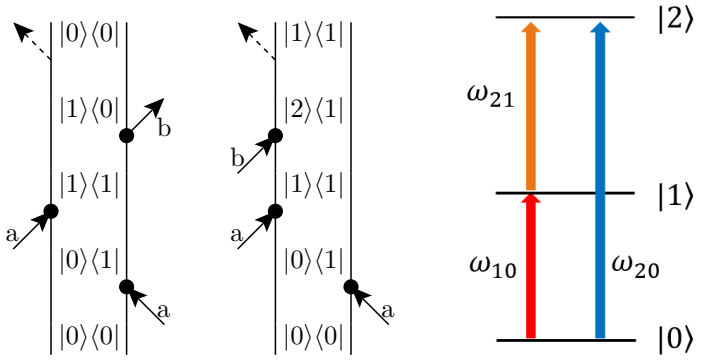

Figure 3.4: SE (left) and ESA (middle) Feynman diagrams representing two contributions to the overall signal in a transient absorption spectroscopy. The energy-level diagram on the right is that of a three-level system with energy eigenstates $|0\rangle, |1\rangle$ and $|2\rangle$, with the different coloured arrows representing the transition frequencies between states. The general mathematical structure describing three-level systems in the context of NLOSs can be found in Chapter 4.

We see in the right diagram in Fig. 3.4 that the first two interactions of pulse a with the system bring it to an excited population state ρ_{11}. The second probe pulse b will then be absorbed, bringing the system in a coherence ρ_{21}. Since we measure the absorption of the probe by the system only after it has been excited by the pump, this diagram's contribution to the overall signal is called excited-state absorption (ESA). The ρ_{21} coherence radiates at frequency $\omega_{21} = \omega_2 - \omega_1$ and, keeping track of the signs, we find that in a TA spectrum, this signal is positive; the absorption of the system has increased due to ESA.

Looking now at the left diagram of Fig. 3.4, the first and second interactions are the same as those for the ESA diagram. However, the last interaction with the probe de-excites the bra, having stimulated the system to a lower-energy coherence ρ_{10}, which radiates at frequency $\omega_{10} = \omega_1 - \omega_0$. This process is therefore known as stimulated emission (SE), which translates to an increase in photon emission from the sample and thus a decrease in its absorption. In a TA spectrum where the signal is the absorption, this diagram represents a negative contribution.

Each diagram from either Fig. 3.2 or Fig. 3.3 represents a contribution to the 3$^{\text{rd}}$-order polarization $P^{(3)}$ in Eq. 3.49. For example, the ESA diagram in Fig. 3.3 corresponds to the term (including the emission of light from the system)

$$P^{(3)}_{ESA} = \int dt_b \int dt_a \varepsilon_b(t-t_b)\varepsilon^*_a(t-t_b-t_a)\varepsilon_a(t-t_b-t_a) \left(\frac{i}{\hbar}\right)^3 \theta(t_b)\theta(t_a)\theta(t_a)\langle\langle \boldsymbol{\mu}|\mathcal{T}_0(t_b,t_a)\mu^K\mathcal{T}_0(t_a,t_a)\mu^B\mathcal{T}_0(t_a,0)\mu^K|\rho^{(0)}\rangle\rangle,$$

while the SE diagram of the same figure represents the term

$$P^{(3)}_{SE} = \int dt_b \int dt_a \varepsilon_b(t-t_b)\varepsilon_a(t-t_b-t_a)\varepsilon^*_a(t-t_b-t_a) \left(\frac{i}{\hbar}\right)^3 \theta(t_b)\theta(t_a)\theta(t_a)\langle\langle \boldsymbol{\mu}|\mathcal{T}_0(t_b,t_a)\mu^B\mathcal{T}_0(t_a,t_a)\mu^K\mathcal{T}_0(t_a,0)\mu^B|\rho^{(0)}\rangle\rangle.$$

It is thus intuitive, using the formalism of optical response functions developped in Sec. 3.3, to read expressions such as those for $P^{(3)}_{ESA}$ and $P^{(3)}_{SE}$ above and directly translate them into Feynman diagrams. This process can be applied to higher-order expressions in a straightforward manner, which we explore in Sec. 3.5 below.

It is important to note that all 6 diagrams from Fig. 3.2 and 3.3 are the time-ordered diagrams for TA. Since we have assumed that the delay time T between pulses a and b is long, the last interaction coming from b will always occur after the two interactions from a. However, if both pulses do overlap, the interaction from the b pulse can take place before one or both of the interactions from pulse a, meaning there are extra permutations of all three interactions in TA and thus more diagrams to consider. For TA, including pulse overlap diagrams leads to a total of 16 Feynman diagrams, with one such example of an overlap diagram shown in Fig. 3.5. For higher-order spectroscopy, the total number of diagrams contributing to a signal increases even more dramatically when including pulse overlap diagrams rather than only time-ordered ones.

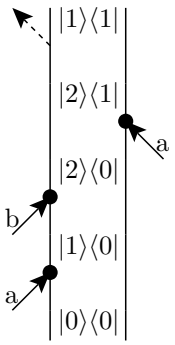

Figure 3.5: ESA overlap diagram. Note that while the final state $|2\rangle\langle 1|$ before the emission of light from the dashed arrow is the same as that of the right ESA diagram of Fig. 3.4, the second interactions differs. In the overlap diagram, rather than the system being brought to a population state ρ_{11} after the first 2 interactions, it is instead in a ρ_{20} coherence, which radiates at a frequency $\omega_{20} = \omega_2 - \omega_0$. This particular diagram represents a different contribution to the total TA signal.

3.5 High-order transient absorption spectroscopy

High-order transient absorption (HOTA) spectroscopy is a very recent technique in nonlinear spectroscopy, with its first experimental demonstration in [28]. HOTA gives a new way to understand and study physical systems; the goal of this section is to provide background on HOTA, namely how to theoretically calculate those signals and what sort of information can be gathered from spectra. Chapter 5 discusses some unexplained results arising from HOTA obtained using squaraine polymers.

The most common coherent nonlinear spectroscopies, including transient absorption spectroscopy, two-pulse and three-pulse photon echo spectroscopy (also called 2D photon echo, 2DPE) and two-dimensional electronic spectroscopy (2DES) measure signals emitted in a particular phase-matching direction $\mathbf{k}_s$, which varies between experiments whose lowest order contributions arise form the 3^{rd}-order polarization. For TA spectroscopy, we have seen that the phase-matching condition is $\mathbf{k}_s = +\mathbf{k}_a - \mathbf{k}_a + \mathbf{k}_b = \mathbf{k}_b$, where in the leading order the system interacts twice with the first pulse and once with the second pulse, and the signal is detected in the same direction as the probe pulse. In two-pulse photon echo, the signal is instead coherently detected in the $\mathbf{k}_s = -\mathbf{k}_a + 2\mathbf{k}_b$ direction, where now the lowest-order signal has is only one interaction with pulse a and two interactions with pulse b. In a 2DPE experiment, the rephasing part of the signal is emitted in the $\mathbf{k}_s = -\mathbf{k}_a + \mathbf{k}_b + \mathbf{k}_c$ direction and the non-rephasing signal is emitted in the $\mathbf{k}_s = +\mathbf{k}_a - \mathbf{k}_b + \mathbf{k}_c$ direction. In all of the cases above, three successive interactions of the system with light lead to a 3^{rd}-order perturbed density matrix $\rho^{(3)}$ (or wavefunction $\left|\psi^{(3)}\right\rangle$ for a closed system) and consequently to a 3^{rd}-order nonlinear polarization $P^{(3)}$and signal. The 2DES signal, which is simply the sum of the rephasing and non-rephasing signals of 2DPE, also has a leading-order contribution that is of 3^{rd}-order.

Using higher intensity pulses can result in more interactions between the system and light, which in turn leads to higher-order signals. More generally, a system interacting $2n+1$ times with a radiation field will result in signals of order $2n+1$. We recall that in the context of this thesis, we focus solely on odd-order spectroscopic signals under the assumption that there are no $2n^{\text{th}}$-order polarization fields, since the systems considered are isotropic and thus the even-order responses and signals vanish by symmetry [2]. For example, in the study of exciton-exciton annihilation (EEA), an experiment must lead to a 5^{th}-order response of the system, with the EEA signal (also called a 2-quantum or 2Q signal) being detected in the $\mathbf{k}_s = -2\mathbf{k}_a + 2\mathbf{k}_b + \mathbf{k}_c$ direction using three pulses a, b, c. In this case, the leading order signal is formed from two interactions with each of the first two pulses and one interaction with the third pulse, this time leading to a 5^{th}-order perturbed density matrix $\rho^{(5)}$ and thus to a 5^{th}-order nonlinear polarization $P^{(5)}$ and signal. Studies of high-order coherent spectroscopies have been recently achieved in an experimental setting [28], though they are less common than their 3^{rd}-order counterparts. This section covers the concepts of high-order TA spectroscopy, though the principles can be applied to any high-order spectroscopic signal.

The core concept of a high-order transient absorption spectroscopy remains to measure the change in a probe pulse's absorption, after the system under study has first been excited by the pump pulse. The key difference between the 3^{rd}-order and HOTA lies in the ability to measure the higher-order TA signals and separate them by orders.

In a TA experiment, if the intensity of the pump pulse is strong enough, the measured signal includes contributions from processes with more interactions between the pump and the system. This increased number of interactions leads to higher-order contributions (5^{th}, 7^{th} and so on coming from the high-order terms in Eq. 3.16) being mixed in the total signal being measured. Experimental observation of this phenomenon of higher-order contaminations to the TA signal is shown in Fig. 3.6.

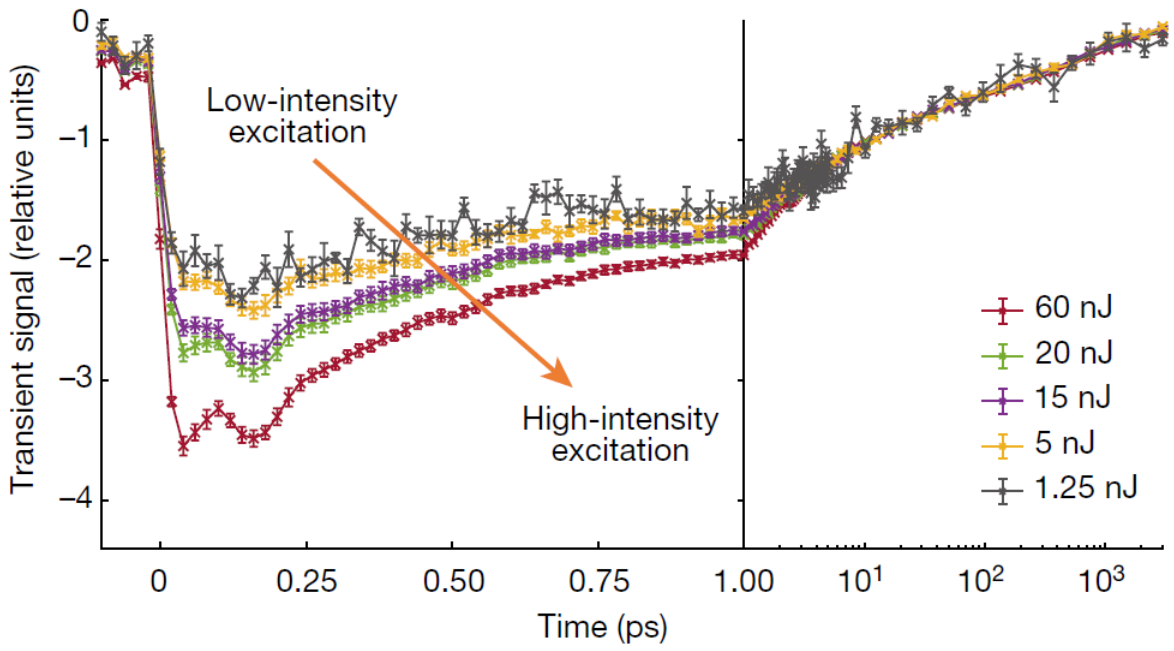

Figure 3.6: Transient signals of squaraine polymers, at a probe wavenumber of 12,650 cm^{-1}, from [28], for different pump pulse energies. As the pump pulse's energy (and thus its intensity) progressively increases, the higher-order signals become non-negligible and start contributing significantly with the total signal, leading to different transients at different pump intensity. The signals are normalized such that their long-time tails (after 1 ps) overlap.

Since the higher-order terms have to be considered, the full TA signal obtained is in fact a mixture of the different n^{th}-order signals, which all contribute simultaneously and have only recently been shown to be separable [28]. In an experiment, the usual procedure is to decrease the pump power until higher-order contributions can be safely neglected. For example, if one wishes to obtain exciton-exciton interaction information from the 5^{th}-order TA signal, the pump power must be low enough to avoid contaminations from 7^{th}-order and above contributions. There are still however contributions to the measured signal that are due to the 3^{rd}-order signal being mixed in with the 5^{th}-order one and which cannot be neglected. Similarly, if we instead want to obtain a TA signal such that highest contributing order signal is the 7^{th}, there will also be non-negligible contributions from the lower 5^{th}- and 3^{rd}-order signals. The same logic applies for higher-order cases, where in general a $(2n+1)^{\text{th}}$-order signal is mixed with all lower-order signals. However, it has recently been experimentally demonstrated that the different contributions to the TA signal can be isolated by nonlinear order by performing intensity-dependent TA [28]. This separation of the TA signals by order, where one obtains a purely $(2n+1)^{\text{th}}$-order signal without the presence of lower-order contributions, is HOTA spectroscopy.

We give here a brief explanation of how signal separation is achieved experimentally by intensity-dependent TA, with the finer details about the procedure and its experimental validation being available in Ref. [28].

To understand how we can obtain separated TA signals by order, we must first turn to the concept of phase

cycling often used in 2D electronic spectroscopy. Phase cycling is a technique that makes possible the extraction of 2DES signals using phase-stable pulse sequences [29]. In the pump-probe geometry, phase cycling allows the gathering of 2DES signals using two collinear pump pulses a and b with the same pulse shape, given by

$$E_{pump}(t) = e^{i(\omega_0 t - \mathbf{k}_{pump}\cdot\mathbf{r})}\left(E_0(t) + E_0(t+\tau)e^{i(\omega_0\tau+\phi_p)}\right) + c.c., \tag{3.50}$$

where $E_0(t)$ is the electric field's amplitude, ω_0 is the carrier frequency, $\mathbf{k}_{pump}$ is the wavevector, which is the same for both pulses since they are collinear, $\mathbf{r}$ is the position, τ is the delay time between the two pump pulses and $\phi_p = \frac{\pi(p-1)}{N}, p = 1, ..., 2N$ is the relative phase between the two pulses. For each time τ, the change in absorption of the probe pulse, pulse c, is measured for the $2N$ values of ϕ_p. Taking the discrete Fourier transform over ϕ_p of the $2N$ data sets $S(\tau, \phi_p)$, all the nQ signals for $n = 1, ..., N$ can be obtained, accurate up to $O(E_0^{2N+1})$ in perturbation theory [29]. Those nQ signals, denoted $S^{(nQ)}(\tau)$ are the signals detected in the phase-matching direction $-n\mathbf{k}_a + n\mathbf{k}_b + \mathbf{k}_c$ when performing a phase-matching experiment. That Fourier transform giving the nQ signals is [29]

$$S^{(nQ)}(\tau) = \frac{1}{2N(1+\delta_{n,N})}\sum_{p=1}^{2N} e^{-in\phi_p}S(\tau, \phi_p). \tag{3.51}$$

In the pump-probe geometry of a TA experiment, we are considering only the time $\tau = 0$ in Eq. 3.51, in which case we effectively have a single pump pulse rather than two of them (since they are collinear), and only its intensity I_p must be controlled. From Eq. 3.50, we have that in this case, I_p is

$$I_p = 4I_0\cos^2\left(\frac{\phi_p}{2}\right),$$

where ϕ_p is now a variable parameter needed to define I_p. This new technique of varying the intensity as a function of ϕ_p is called intensity cycling. We have [28]

$$\cos^2\left(\frac{\pi(2N-p)}{2N}\right) = \cos^2\left(\frac{\pi p}{2N}\right),\ p = 1, ..., N-1,$$

which allows to rewrite Eq. 3.51 as

$$S^{(nQ)}(\tau = 0) = \sum_{p=1}^{N}\frac{2-\delta_{p,1}}{2N(1+\delta_{n,N})}\cos\left(\frac{2\pi n(p-1)}{2N}\right)e^{-in\phi_p}S(\tau = 0, \phi_p). \tag{3.52}$$

With the idea of intensity cycling in mind, we now do a perturbative expansion of the TA pump-probe signal $PP(I_p)$ as a function of excitation intensity I_p [2],

$$PP(I_p) = PP^{(3)}I_p + PP^{(5)}I_p^2 + PP^{(7)}I_p^3 + ... = \sum_{r=1}^{\infty} PP^{(2r+1)}I_p^r, \tag{3.53}$$

where $PP^{(2r+1)}$ is the $(2r+1)$ th-order response. At a given pump intensity I_p, there exists an integer N for which the series in Eq. 3.53 may be truncated at N terms. We can measure $PP(I_p)$ at N values of I_p, with $p = 1, ..., N$, where the choices for I_p are dictated by the intensity cycling procedure discussed above. The different pump intensities I_p are then

$$I_p = 4I_0 \cos^2\left(\frac{\pi(p-1)}{2N}\right),\ p = 1, ..., N, \tag{3.54}$$

where I_0 is the base pump power. The choices for I_p then allow one to add together the N signals $PP(I_p)$ as

$$PP^{(nQ)}(I_0) = \sum_{p=1}^{N} \frac{1}{2N} \frac{2-\delta_{p,1}}{1+\delta_{n,N}} \cos\left(\frac{2\pi n(p-1)}{2N}\right) PP(I_p). \tag{3.55}$$

The $PP^{(nQ)}$ are the n-quantum (nQ) signals from multidimensional spectroscopy at $\tau = 0$ [8]. The leading order contribution to $PP^{(nQ)}$ is $2n+1$, though higher-order contaminations are still present in this signal. The contribution of the nonlinear orders to the n-quantum signals is evaluated quantitatively

$$PP^{(nQ)}(I_0) = \sum_{r=n}^{N} \Lambda_r^{nQ} PP^{(2r+1)} I_0^r, \tag{3.56}$$

using the derivation in Ref. [28], where combining Eqs. 3.54 and 3.51 yields

$$PP^{(nQ)} = \sum_{r=1}^{\infty} PP^{(2r+1)} I_0^r 4^r \frac{1}{2N} \frac{1}{1+\delta_{n,N}} \left(\sum_{p=1}^{2N} e^{-i\pi n(p-1)/N} (\cos(\pi(p-1)/2N))^{2r}\right),$$

where we have

$$\Lambda_r^{nQ} = 4^r \frac{1}{2N} \frac{1}{1+\delta_{n,N}} \left(\sum_{p=1}^{2N} e^{-i\pi n(p-1)/N} (\cos(\pi(p-1)/2N))^{2r}\right).$$

The Λ_r^{nQ} terms are the coefficients of the upper-unitriangular matrix Λ and it can be shown (see Methods section of Ref. [28]) that

$$\Lambda_r^{nQ} = \begin{pmatrix} 2r \\ r-n \end{pmatrix}.$$

The matrix Λ is invertible, and have the form [28]

$$\Lambda^{-1} = \sum_{a=0}^{N-1} (\mathbb{I} - \Lambda)^a.$$

Finally, the nonlinear signals are then isolated by orders and we obtain [28]

$$PP^{(2r+1)} I_0^r = \sum_{n=r}^{N} \left(\Lambda^{-1}\right)_{nQ}^{r} PP^{(nQ)}(I_0). \tag{3.57}$$

Now that we know how to separate the HOTA signals using intensity-dependent TA, we discuss how to char-

acterize the various orders of high-order signals and what they can tell us. A simple and straightforward way to characterize a HOTA signal is through its phase-matching condition, which is given by

$$\mathbf{k}_s = +n\mathbf{k}_a - n\mathbf{k}_a + \mathbf{k}_b \tag{3.58}$$

where n is an integer. Since the number of interactions with the rotating terms of pulse a, in direction $+\mathbf{k}_a$, is the same as the number of interactions with the counter-rotating terms of the same pulse in direction $-\mathbf{k}_a$, the vector sum in 3.58 still yields $\mathbf{k}_s = \mathbf{k}_b$. The case $n = 1$ corresponds to the standard weak-pump TA experiment, while HOTA corresponds to any other case where $n \geq 2$ and the different n's have been separated as in the procedure outlined above. For example, for $n = 2$ corresponds to the 5^{th}-order TA signal, which has the phase-matching condition $\mathbf{k}_s = 2\mathbf{k}_a - 2\mathbf{k}_a + \mathbf{k}_b$. The 5^{th}-order polarization $P^{(5)}$ emitted in this case is of the form

$$P^{(5)}_{TA}(t) = \int dt_b \int dt_a E_a(t - t_b - t_a)E_a(t - t_b - t_a)E_a(t - t_b - t_a)E_a(t - t_b - t_a)E_b(t - t_b)S^{(5)}(t_a,t_b), \tag{3.59}$$

with the fifth-order response function $S^{(5)}$ given by

$$S^{(5)}(t_a, t_b) = \left(\frac{i}{\hbar}\right)^5 \theta(t_a)\theta(t_b) \sum_{\alpha,\ldots,\alpha''''=K,B} \langle\langle \mu|\mathcal{T}_0(t_b, t_a)\mu^{\alpha''''}\mathcal{T}_0(t_a, t_a)\mu^{\alpha'''}\mathcal{T}_0(t_a, t_a)\mu^{\alpha''}\mathcal{T}_0(t_a, t_a)\mu^{\alpha'}\mathcal{T}_0(t_a, 0)\mu^{\alpha}|\rho^{(0)}\rangle\rangle$$

Using the fact that $\mathcal{T}_0(t_a, t_a)$ is simply the identity, we can simplify the expression for $S^{(5)}$, yielding

$$S^{(5)}(t_a, t_b) = \left(\frac{i}{\hbar}\right)^5 \theta(t_a)\theta(t_b) \sum_{\alpha,\ldots,\alpha''''=K,B} \langle\langle \mu|\mathcal{T}_0(t_b, t_a)\mu^{\alpha''''}\mu^{\alpha'''}\mu^{\alpha''}\mu^{\alpha'}\mathcal{T}_0(t_a, 0)\mu^{\alpha}|\rho^{(0)}\rangle\rangle. \tag{3.60}$$

We can pick one of the terms in Eq. 3.60 and translate it to a Feynman diagram. Choosing the case $\alpha = B, \alpha' = B, \alpha'' = K, \alpha''' = K, \alpha'''' = K$, we have that, suppressing the time interval of the electric fields for conciseness, the contribution to the polarization $P^{(5)}$ in Eq. 3.59 is proportional to

$$\int dt_b \int dt_a \varepsilon_b\varepsilon_a\varepsilon_a\varepsilon_a\varepsilon^*_a\varepsilon^*_a \left(\frac{i}{\hbar}\right)^5 \theta(t_a)\theta(t_b)\langle\langle \mu|\mathcal{T}_0(t_b, t_a)\mu^K\mu^K\mu^K\mu^B\mathcal{T}_0(t_a, 0)\mu^B|\rho^{(0)}\rangle\rangle. \tag{3.61}$$

As in Sec. 3.4, we can analyze Eq. 3.61 and construct the Feynman diagram associated with it. The first two interactions contain the terms $\varepsilon_a\mu^K$, which means the diagram first has two right-pointing arrows on the ket side of the density matrix. The next two interactions are of the form $\varepsilon^*_a\mu^B$, meaning the diagram then has two left-pointing arrows on the bra side of the density matrix. Finally, the last interaction has the product $\varepsilon_b\mu^K$, meaning the last arrow is on the ket side of ρ, pointing to the right. The corresponding diagram for this contribution to the polarization is shown in Fig. 3.7 below.

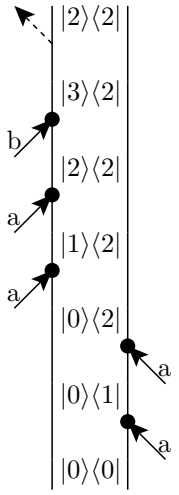

Figure 3.7: Fifth-order double-sided Feynman diagram for a fifth-order contribution to transient absorption spectroscopy, corresponding to the phase-matching condition $\mathbf{k}_s = 2\mathbf{k}_a - 2\mathbf{k}_a + \mathbf{k}_b$.

We can compare the 5$^{\text{th}}$-order diagram of Fig. 3.7 to the 3$^{\text{rd}}$-order ESA diagram of Fig. 3.4 and look at their respective signs. In the 5$^{\text{th}}$-order diagram, there is one extra interaction from pulse a on the bra side of ρ, carrying a factor of -1 and another interaction from the same pulse on the ket side. Since both interactions also come with a factor of $\frac{i}{\hbar}$ (for a total factor of $\frac{-1}{\hbar^2}$), the sign of the diagram does not differ from the 3$^{\text{rd}}$-order diagram and is therefore positive. Thus, the diagram in Fig. 3.7 represents one of the ESA contribution to the TA signal. We may also note that in 3$^{\text{rd}}$-order ESA, the system has a population after the pump pulse in the state $|1\rangle\langle 1|$ whereas the 5$^{\text{th}}$-order ESA has a population after the pump pulse in the state $|2\rangle\langle 2|$. Hence, the probe pulse b will in the first case report on the absorption of singly-excited states and in the second case, the absorption of doubly-excited states, yielding different signals.

If we instead consider that the last interaction from pulse b occurs on the bra side, shown in Fig. 3.8 (and therefore carrying a factor of -1), the sign of the diagram below is negative. This diagram represents stimulated emission, since the action of the probe pulse b stimulates the doubly-excited state $|2\rangle\langle 2|$ to a coherence state $|2\rangle\langle 1|$. This increased emission represents a decrease in the probe's absorption and thus is a negative contribution to the 5$^{\text{th}}$-order TA signal. If pulses a and b do not overlap in time and therefore only time-ordered diagrams are taken into account for the fifth-order case, there are 54 Feynman diagrams (according to the Diagram Generator of Ref. [27]) contributing to the signal, compared to the 6 time-ordered diagrams of the third-order case. If the pulses do overlap, there are 240 5$^{\text{th}}$-order diagrams (again according to the DG) to consider instead of the 16 3$^{\text{rd}}$-order diagrams.

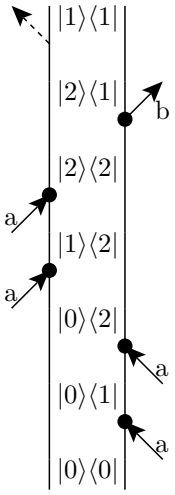

Figure 3.8: Fifth-order Feynman diagram for TA spectroscopy for a stimulated emission process.

We may now repeat a similar analysis for the cases of 7$^{\text{th}}$-order TA signals. These cases correspond to having $n = 3$ in Eq. 3.58, where the electric field a contains one extra rotating (ε_a) and counter-rotating (ε_a^*) term, we now have a 7$^{\text{th}}$-order polarization field given by

$$P_{TA}^{(7)}(t) = \int dt_b \int dt_a E_a E_a E_a E_a E_a E_a E_b S^{(7)}(t_a, t_b),$$

with

$$S^{(7)}(t_a, t_b) = \left(\frac{i}{\hbar}\right)^7 \theta(t_a)\theta(t_b) \sum_{\alpha,\ldots,\alpha''''''} \langle\langle \mu | \mathcal{T}_0(t_b, t_a) \mu^{\alpha''''''} \mu^{\alpha''''} \mu^{\alpha''''} \mu^{\alpha'''} \mu^{\alpha''} \mu^{\alpha'} \mathcal{T}_0(t_a, 0) \mu^{\alpha} | \rho^{(0)} \rangle\rangle.$$

Choosing $\alpha = B, \alpha' = B, \alpha'' = B, \alpha''' = K, \alpha'''' = K, \alpha''''' = K, \alpha'''''' = K$ (adding one interaction on each side of the density matrix from pulse a), we have that with this choice of α's, the contribution to $P_{TA}^{(7)}$ is proportional to

$$\int dt_b \int dt_a \varepsilon_b \varepsilon_a \varepsilon_a \varepsilon_a \varepsilon_a^* \varepsilon_a^* \varepsilon_a^* \left(\frac{i}{\hbar}\right)^7 \theta(t_a)\theta(t_b) \langle\langle \mu | \mathcal{T}_0(t_b, t_a) \mu^K \mu^K \mu^K \mu^K \mu^B \mu^B \mathcal{T}_0(t_a, 0) \mu^B | \rho^{(0)} \rangle\rangle.$$

Performing the same analysis as for the $n = 2$ case, the Feynman diagram for this contribution to the overall $P_{TA}^{(7)}$ has 3 right-pointing arrows on the ket side of the system's density matrix, 3 left-pointing arrows on the bra side of ρ and finally one right-pointing arrow, again on the ket side of ρ. This diagram is shown in Fig. 3.9 below.

We can briefly compare this 7$^{\text{th}}$-order diagram to both the 3$^{\text{rd}}$-order ESA diagram of Fig. 3.4 and 5$^{\text{th}}$-order ESA diagram of Fig. 3.7. All three diagrams have a positive sign, although the 7$^{\text{th}}$-order now has, after the pump's interaction, a population in the triply-excited state $|3\rangle\langle 3|$ rather than in the singly-excited state or doubly-excited state. When pulses a and b overlap, there are, according to the Diagram Generator, 3584 diagrams for the 7$^{\text{th}}$-order case and 570 time-ordered diagrams.

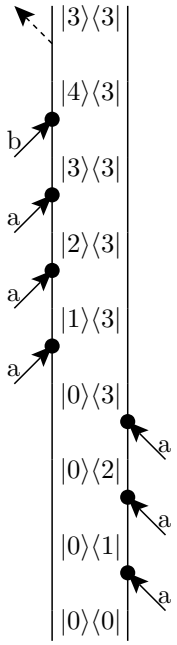

Figure 3.9: Example seventh-order double-sided Feynman diagram for TA spectroscopy, corresponding to the phase-matching condition $\mathbf{k}_s = 3\mathbf{k}_a - 3\mathbf{k}_a + \mathbf{k}_b$. This diagram represents a positive contribution to the 7^{th}-order signal due to ESA.

The cases of $n = 4$ and above follow the same line of reasoning, leading to 9^{th}-order ($n = 4$), 11^{th}-order ($n = 5$),13^{th}-order ($n = 6$) polarization and signals and so on.

We have shown here the cases of high-order TA signals obtained using only two pulses. Though we will not apply this concept in Chapter 5, it is interesting to note that the same logic can be applied to a $(2n+1)^{\text{th}}$-order signal generated using instead a larger number of pulses, with each interacting fewer times with the sample. If we consider for example the fifth-order polarization $P^{(5)}_{EEA}$ arising from exciton-exciton annihilation, using 3 pulses E_a, E_b, E_c, with the phase-matching condition $\mathbf{k}_s = -2\mathbf{k}_a + 2\mathbf{k}_b + \mathbf{k}_c$. The nonlinear polarization in this case will be

$$P^{(5)}_{EEA}(t) = \int dt_c \int dt_b \int dt_a E_a(t-t_c-t_b-t_a)E_a(t-t_c-t_b-t_a)E_b(t-t_c-t_b)E_b(t-t_c-t_b)E_c(t-t_c)S^{(5)}(t_a,t_b,t_c). \tag{3.62}$$

The expression in Eq. 3.62 is similar to the expression for $P^{(5)}_{TA}$, except there is now a delay between the second interaction with pulse a, and the third and fourth interactions with pulse b. The response function in this case is

$$S^{(5)}(t_a,t_b,t_c) = \left(\frac{i}{\hbar}\right)^5 \theta(t_c)\theta(t_b)\theta(t_b)\theta(t_a)\theta(t_a) \sum_{\alpha,\ldots,\alpha''''} \langle\langle \mu|\mathcal{T}_0(t_c,t_b)\mu^{\alpha''''}\mathcal{T}_0(t_b,t_b)\mu^{\alpha'''}\mathcal{T}_0(t_b,t_a)\mu^{\alpha''}\mathcal{T}_0(t_a,t_a)\mu^{\alpha'}\mathcal{T}_0(t_a,0)\mu^{\alpha}|\rho^{(0)}\rangle\rangle.$$

Choosing $\alpha = B, \alpha' = B, \alpha'' = K, \alpha''' = K, \alpha'''' = K$, the contribution of this term to Eq. 3.62 is proportional to

$$\int dt_c \int dt_b \int dt_a \varepsilon_c \varepsilon_b \varepsilon_b \varepsilon_a^* \varepsilon_a^* \left(\frac{i}{\hbar}\right)^5 \theta(t_a)\theta(t_a)\theta(t_b)\theta(t_b)\theta(t_c) \tag{3.63}$$

$$\langle\langle \mu | \mathcal{T}_0(t_c, t_b) \mu^K \mathcal{T}_0(t_b, t_b) \mu^K \mathcal{T}_0(t_b, t_a) \mu^K \mathcal{T}_0(t_a, t_a) \mu^B \mathcal{T}_0(t_a, 0) \mu^B | \rho^{(0)} \rangle\rangle, \tag{3.64}$$

and the Feynman diagram in this case is

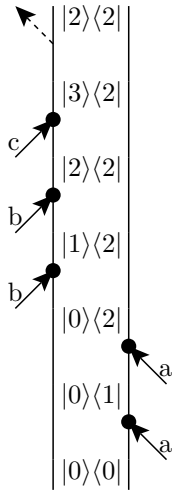

Figure 3.10: Fifth-order Feynman diagram of exciton-exciton annihilation, using three pulses a, b, c with phase-matching conditon $\mathbf{k}_s = -2\mathbf{k}_a + 2\mathbf{k}_b + \mathbf{k}_c$. In the case where all three pulses overlap with each other in time, this diagram is only one of the 240 diagrams contributing to the overall EEA signal.

We note that the diagram in Fig. 3.10 is almost identical to the 5^{th}-order TA diagram of Fig. 3.7. If the delay time $(t_b - t_a)_{EEA}$ between pulse b and a is zero, and the delay time $(t_c - t_b)_{EEA}$ for the EEA diagram is the same delay time as $(t_b - t_a)_{TA}$ for the TA diagram, and assuming that for both experiments the pulses all have the same shape A_j, central frequencies ω_j and polarizations, we would obtain the same contribution to the fifth-order polarization $P^{(5)}$ from either diagram, where the only difference would lie in the direction of propagation of the polarization. The advantage of using 3 pulses instead of 2 is in the control of the time delay τ between pulses a and b and the time delay T between b and c. If either $\tau = (t_b - t_a)_{EEA}$ is non-zero or $T = (t_c - t_b)_{EEA} \neq (t_b - t_a)_{TA}$, the contribution of 3.63 (represented by the diagram in Fig. 3.10) to $P^{(5)}$ has a different form compared to the contribution of 3.61 (represented by the diagram in Fig. 3.7) to $P^{(5)}$.

3.6 Ultrafast Spectroscopy Suite

The content of Chapters 1 through 3 cover the fundamental ideas of nonlinear optical spectroscopies, mostly focusing on a theoretical approach to the subject. We explored how, given a simple model for the system's Hamiltonian

or Liouvillian and a model for interaction between the system and optical fields, we can use time-dependent perturbation theory to compute a spectroscopic signal of our choice. In (theoretical) practice however, even when modelling small systems interacting with a low number of pulses, and despite using the plethora of assumptions and approximations previously discussed, the option of carrying out the analytical calculations by hand, going from a perturbed density matrix Eq. 3.33 to the desired signal, 3.13, is generally a tedious task. Going to larger systems and higher-order spectroscopy would be both near impossible and largely inefficient. We are thus in need of a set of computational tools that are capable of generating molecular system models, organize spectroscopic calculations with Feynman diagrams and carrying out calculations corresponding to those Feynman diagrams to arrive at a signal spectrum. This is where the Ultrafast Spectroscopy Suite (UFSS) comes into play.

UFSS is an open source software suite written in Python, specifically designed to rapidly simulate nonlinear optical spectroscopies automatically from simple user-provided parameter inputs, and is comprised of 4 main modules that can all work independently from each other: the Diagram Generator (DG), the Ultrafast Ultrafast Spectroscopy (UF^2) algorithm, the Runge-Kutta-Euler (RKE) algorithm and the Hamiltonian/Liouvillian Generator (HLG), with each module's function briefly explained below. An in-depth overview of UFSS as a whole and the inner workings of its major components are all freely available [7, 22, 27, 30].

Briefly, the procedure of using UFSS to calculate a spectroscopic signal is as follows : a user first specifies the Hamiltonian or Liouvillian of the system to study, which can be done using the HLG, though it can be done without using it as well. Then, the user inputs information about the pulses, which are defined by their intervals, and a phase-matching condition (PMC). Information about the pulses and the PMC are then sent to the Diagram Generator, which will generate a list of all the Feynman diagrams that represent a contribution to the signal. The list of diagrams and the Hamiltonian or Liouvillian are given as inputs to either UF^2 or RKE, calculating the contribution of each diagram in the list to the total signal.

The Hamiltonian/Liouvillian Generator is the tool capable of producing the Hamiltonian or Liouvillian of vibronic systems of the form seen in Chapter 2. The HLG also creates all the other relevant operators necessary for calculations, such as the transition dipole of the system, $\boldsymbol{\mu}$. We start by giving the HLG three separate lists that describe the electronic properties of each molecule (internally referred to as sites) i: the first list contains the singly-excited state energies E_i, the second list the electronic couplings J_{ij} and the last list specifies the transition dipole $\boldsymbol{\mu}_{10,i}$. From these three inputs, the HLG generates the electronic Hamitonian of the system H_e. In addition, we can include (although it is not necessary), for each site, one or more vibrational mode, each with an electronic coupling $d_{k,i}$ and vibrational frequency ω_k. We must also specify a maximum number n of vibrational energy levels for all modes. When including vibrations, the HLG then also builds the vibrational and the electronic-vibrational coupling Hamiltonians, H_{vib} and H_{el-vib}. Combined together, the three separate Hamiltonians give the full system's Hamiltonian H_0. If we only wish to study the closed version of our model, we may stop the model generation and the matrices representing H_0 and $\boldsymbol{\mu}$ necessary for calculations are given to UF^2 or RKE, along with the pulses

and phase-matching condition (giving a list of diagrams), and perform a simulation of our choice. Otherwise, if we wish to include open system effects, we must also specify the bath parameters to include inter- and intra-manifold relaxation processes and vibrational-bath couplings. The specific parameters will depend upon which formalism available in UFSS is chosen to treat the bath, Redfield or Lindblad (the former being covered in Chapter 2) and so we omit the specifics for brevity. With these bath parameters, the HLG will construct the dissipation operator D and with that, the system's Liouvillian $\mathcal{L}_0$, along with the transition dipoles $\boldsymbol{\mu}^K, \boldsymbol{\mu}^B$. Again, as for closed systems, the matrices representing $\mathcal{L}_0$ and $\boldsymbol{\mu}^K, \boldsymbol{\mu}^B$ are sent to either calculation algorithm available.

The Diagram Generator (DG) is capable of generating single- or double-sided Feynman diagrams to any order of perturbation, given an arbitrary number of pulses (each being defined by its duration and arrival time), the interval between successive pulses and a phase-matching or phase-cycling condition. Under the hood, the DG determines which Feynman diagrams contribute to the signal. For each diagram, it produces a list of commands, denoted $(Ku, j), (Kd, j), (Bu, j), (Bd, j)$ in the UFSS syntax, which correspond to the operators [22, 27]

$$O_{j(*)} = \eta_O \frac{i}{\hbar} \int_0^\infty dt' \mathcal{T}_0(t', 0) \left(\boldsymbol{\mu}^O \cdot \mathbf{e}_j^{(*)} \varepsilon_j^{(*)}(t - t') \right) ; \tag{3.65}$$

$$O = K, B ;$$

$$\eta_K = 1 ; \eta_B = -1$$

acting on the sytem's density matrix $|\rho\rangle\rangle$ and where j specifies the pulse. Eq. 3.65 has a closed system equivalent, in which case the DG only produces $(Ku, j), (Kd, j)$. We note that $O_{j(*)}|\rho^{(n-1)}(t - t')\rangle\rangle$ is simply Eq. 3.33 with the interaction Liouvillian $\mathcal{L}'$ written explicitly. We can illustrate what this list of command represents by taking for example the diagrams in Fig. 3.11 contributing to the rephasing 2D photon echo (2DPE) signal.

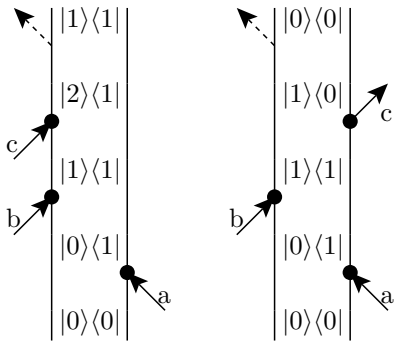

Figure 3.11: Feynman diagram representing two different contributions to the rephasing 2DPE signal, with the phase-matching condition $\mathbf{k}_s = -\mathbf{k}_a + \mathbf{k}_b + \mathbf{k}_c$.

For the left diagram, the DG will give the list $(Bu, a), (Ku, b), (Ku, c)$. Given a starting density matrix $|\rho^{(0)}\rangle\rangle = |0\rangle\langle 0|$, this diagram corresponds to first calculating $B_{a*}|\rho^{(0)}\rangle\rangle$, then $K_b \left(B_{a*}|\rho^{(0)}\rangle\rangle \right)$ and finally $K_c \left[K_b \left(B_{a*}|\rho^{(0)}\rangle\rangle \right) \right]$.

For the right diagram, the DG will instead produce the list $(Bu, a), (Ku, b), (Bd, c)$, which corresponds to calculating $K_{c*}\left[K_b\left(B_{a*}|\rho^{(0)}\rangle\rangle\right)\right]$. Both diagrams represent a different contribution to the density matrix $\rho^{(n)}$ producing the desired signal.

Both the UF^2 and RKE modules are algorithms to calculate the actions of the $O_{j(*)}$ operators on an intial wavefunction $\left|\psi^{(0)}\right\rangle$ or density matrix $\rho^{(0)}$, and obtain a perturbed wavefunction $\left|\psi^{(n)}(t)\right\rangle$ or density matrix $\rho^{(n)}(t)$. The RKE module is a direct-propagation method, using the Runge-Kutta $4-5^{th}$ order solver (commonly referred to as RK45) with adaptative step size to propagate the evolution of the system due to H_0 or $\mathcal{L}_0$, and the Euler method for the propagation due to H' or $\mathcal{L}'$. UF^2 on the other hand is a Fast-Fourier Transform (FFT) and convolution based method. Depending in part on the size of the system under study, one of these methods might be more suitable than the other to simulate a spectroscopy, with for example UF^2 having a computational advantage over RKE for systems requiring less than 20 GB to store $\mathcal{L}_0$, if the bath is treated using Redfield theory, and an advantage for all system sizes if using secular Redfield theory [22].

As previously mentioned, all 4 mains modules can work seperately. If, for example, we only wish to study the Feynman diagrams relevant to a particular spectroscopy without being concerned about any specific model, we are free to do so without using any other module. Conversely, if we would like to generate the Hamiltonian or Liouvillian (and other useful operators) for some system without the goal of spectroscopy in mind, we can. If we are interested in using the UF^2 or RKE propagators but our model cannot be easily produced by the HLG, we can instead give UFSS our own model, in a form that can be handled, meaning the Hamiltonian/Liouvillian ($H_0/\mathcal{L}_0$) and the transition dipole ($\boldsymbol{\mu}$) of the sytem are represented as finite matrices that are given as inputs to UF^2 or RKE.

The next two chapters will dive deeper into how we can first modify the HLG in UFSS to generate more complicated electronic systems than what was previously possible with the original version of the software [7], and afterwards make use of the UF^2 algorithm to simulate high-order spectroscopy.

Chapter 4

Three-level System Generator

The models for Hamiltonians or Liouvillians of polymers of two-level systems (2LSs) described in Chapter 2 are capable of modeling a range of common features of molecular systems, such as electronic coupling of individual sites or the dephasing and relaxation effects caused by interactions of those systems with a bath, to name a few. Such polymers of 2LSs, along with the relevant operators necessary to model the light-matter interaction described in Chapter 3, can be generated using the Hamiltonian/Liouvillian Generator (HLG) module of UFSS, described in Sec. 3.6. The HLG has been previously used to model systems whose Hamiltonians are of dimension $\sim 10^3$ (and thus Liouvillians of dimension $\sim 10^6$)[22].

While such models have been used to describe a variety of systems and to study for example, energy transfer in photosynthetic complexes [ref], the simple two-level electronic structure of the individual units naturally leads to certain limitations in what sort of phenomena can be studied. One such example is exciton-exciton interaction 2D (EEI2D) spectroscopy [8, 11, 31], which can be used to study exciton-exciton annihilation (EEA). If two single excitons, which are initially spatially separated on different molecules of a system, reach the same molecule, they may recombine, creating a doubly-excited excitation on that site. This doubly-excited state on one site can then either separate back into two spatially separated exctions on different sites, or alternatively, relax to a single excitation on the same site. The latter process of two single excitons combining to create a biexciton on one site, which subsequently relaxes to a single exciton is exciton-exciton annihilation. Such a phenomenon cannot be modeled using 2LSs, since each site can only have a single excitation. We thus need a model for a site that can be doubly-excited, the simplest of which is a three-level system (3LS). We can then make a polymer of such sites, enabling the study of EEA and modelling of EEI2D spectra.

The three-level systems studied in this thesis are the natural extension of the two-level systems covered in Chapter 2, where each site is composed of electronic ground state and singly-excited state, just as a two-level system, but now also includes a doubly-excited state, with the energy-level diagram of such a system shown in Fig. 4.1. Transitions between ground and doubly-excited states and between singly-excited and doubly-excited

states can also be included, as well as inter-unit couplings of the same kind seen in Chapter 2 for 2LS. System-bath coupling is also included to describe open system dynamics, with inter- and intra-manifold relaxation processes described using once again Redfield theory.

A dimer of 3LS of the kind described above has previously been created and, in conjunction with the UF^2 algorithm, used to simulate EEI2D spectroscopy [27]. Even simulating such a rather simple system can be tedious; it first requires creating the system's Hamiltonian by manually defining the individual monomer's Hamiltonian, as well as their transition dipoles, with all operators then defined in the full dimer's Hilbert space $\mathcal{H}$. Additionally, in order to obtain the dimer's Liouvillian $\mathcal{L}_0$ modelling the open system dynamics, relaxation rates must be defined for each state in the energy eigenbasis, and the dipoles have to be redefined in the Liouville space $\mathscr{L}$ of the system. While an arbitrary Hamiltonian or Liouvillian can be used with UFSS, before this thesis work there were no tools in UFSS to make polymers of 3LSs, rendering the task of manually creating those Hamiltonians and Liouvillians tedious. A manual method also scales poorly with increasing system sizes as it is prone to suffering from human error, which is often the case when defining and manipulating a large number of variables by hand.

The objective of this chapter is to describe the modifications made to the already available tools of the HLG that allow a user to procedurally generate Hamiltonians and Liouvillians of polymers consisting of an arbitrary number of 3LS. The next two sections detail the mathematical structure of three-level systems and how we can create all outputs necessary for numerical calculations as finite matrices, for both closed and open systems.

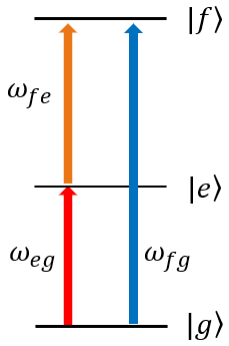

Figure 4.1: Energy diagram of a three-level system (3LS). The system is composed of an electronic ground state $|g\rangle$,a singly-excited state $|e\rangle$and a doubly-excited state $|f\rangle$. The different transition frequencies are : ω_{eg} from ground to singly-excited state (red arrow), ω_{fg} from ground to doubly-excited state (blue arrow) and ω_{fe} from singly- to doubly-excited state (orange arrow). The ω_{eg} and ω_{fe} need not be the same, though they are usually on the same order of magnitude.

4.1 Closed system generator

We begin our discussion in much the same manner as that for two-level systems in Chapter 2, where we again consider a polymer made of n coupled monomers, where each monomer i is now modeled as a three-level system. Fig. 4.1 shows an energy diagram of a 3LS unit, which is made up of, as its name suggests, three electronic states: a ground state $|g_i\rangle$ with energy $\varepsilon_{g,i}$, a singly-excited state $|e_i\rangle$ with energy $\varepsilon_{e,i}$ and doubly-excited state $|f_i\rangle$with energy $\varepsilon_{f,i}$. We represent individual site states and operators of 3LS as 3×1 column vectors and 3×3 matrices respectively and make use of second quantized notation.

Each unit can have up to 2 excitations and there are three possible transitions to consider. Similarly to the 2LS case, a single excitation on site i is represented by the creation operator $a_i^\dagger$ such that $a_i^\dagger|g_i\rangle = |e_i\rangle$. A double excitation on the same site can be represented in two different manners. If the site already contains an excitation, then the double excitation is represented by the operator $c_i^\dagger$, such that $c_i^\dagger|e_i\rangle = |f_i\rangle$. Otherwise, if the site is initially in its ground state and therefore has no excitation, the double excitation is represented by the operator $b_i^\dagger$, such that $b_i^\dagger|g_i\rangle = |f_i\rangle$. The matrix form of each operator is

$$a_i^\dagger = \begin{pmatrix} 0 & 0 & 0 \\ 1 & 0 & 0 \\ 0 & 0 & 0 \end{pmatrix}, \; b_i^\dagger = \begin{pmatrix} 0 & 0 & 0 \\ 0 & 0 & 0 \\ 1 & 0 & 0 \end{pmatrix}, \; c_i^\dagger = \begin{pmatrix} 0 & 0 & 0 \\ 0 & 0 & 0 \\ 0 & 1 & 0 \end{pmatrix}. \tag{4.1}$$

with the de-excitation (removal of an excitation) on site i are represented by the Hermitian conjugate of the creation operators,

$$a_i = \begin{pmatrix} 0 & 1 & 0 \\ 0 & 0 & 0 \\ 0 & 0 & 0 \end{pmatrix}, \; b_i = \begin{pmatrix} 0 & 0 & 1 \\ 0 & 0 & 0 \\ 0 & 0 & 0 \end{pmatrix}, \; c_i = \begin{pmatrix} 0 & 0 & 0 \\ 0 & 0 & 1 \\ 0 & 0 & 0 \end{pmatrix} \tag{4.2}$$

For example, a doubly-excited site $|f_i\rangle$ can be de-excited to its ground state by the action of $b_i|f_i\rangle = |g_i\rangle$, or to its singly-excited state by the action of $c_i|f_i\rangle = |e_i\rangle$. A site Hamiltonian is, setting $\varepsilon_{g,i} = 0$,

$$H_i = \begin{pmatrix} 0 & 0 & 0 \\ 0 & \varepsilon_{e,i} & 0 \\ 0 & 0 & \varepsilon_{f,i} \end{pmatrix} = \varepsilon_{e,i} a_i^\dagger a_i + \varepsilon_{f,i} c_i^\dagger c_i. \tag{4.3}$$

We include inter-unit electronic coupling of the same nature as seen in Chapter 2, with constants J_{ij}, K_{ij} and L_{ij}, corresponding to 1-exciton, 2-exciton and 3-exciton coupling constants respectively. The coupling of a singly-excited site i to a ground state site j is $J_{ij} a_i^\dagger a_j$, and its Hermitian conjugate $J_{ji} a_i a_j^\dagger$. This 1-exciton coupling is of the same form as the only electronic coupling for 2LSs. Biexciton (or 2-exciton) coupling, which is the coupling of two singly-excited sites i and j, is given by $K_{ij} c_i^\dagger a_j$ and $K_{ji} a_i c_j^\dagger$. We ignore biexciton coupling from a doubly-excited site

and a ground state site, which would correspond to $M_{ij}c_i a_j^\dagger$. Finally, the 3-exciton coupling is given by $L_{ij}c_i c_j^\dagger$ and $L_{ij}c_i^\dagger c_j$. Taking a polymer of arbitrary size, and taking three states $|\alpha\rangle = |g_i...e_j\rangle$,$|\beta\rangle = |e_i...e_j\rangle$and $|\Gamma\rangle = |f_i...e_j\rangle$. The state $|\alpha\rangle$ correponds to having a single exciton on site j with all other sites being in the ground state, meaning a total of 1 exciton in the polymer; the state $|\beta\rangle$ represents a state with two excitons, one each on site i and j ; finally, the state $|\Gamma\rangle$ correponds to two excitons on site i and one exciton on site j. Thus, the 1-exciton coupling $J_{ij}a_i^\dagger a_j$ on state $|\alpha\rangle$ is

$$J_{ij}a_i^\dagger a_j|\alpha\rangle = J_{ij}|e_i...g_j\rangle.$$

The 1-exciton coupling couples states of the form $|g_i...e_j\rangle$ to states of form $|e_i...g_j\rangle$, with energy J_{ij}. Similarly, the 2-exciton coupling $K_{ij}c_i^\dagger a_j$ on state $|\beta\rangle$ is

$$K_{ij}c_i^\dagger a_j|\beta\rangle = K_{ij}|f_i...g_j\rangle,$$

meaning the 2-exciton coupling couples states of form $|e_i...e_j\rangle$ to states of form $|f_i...g_j\rangle$. Finally, the 3-exciton coupling $L_{ij}c_i c_j^\dagger$ on state $|\Gamma\rangle$ is

$$L_{ij}c_i c_j^\dagger|\Gamma\rangle = L_{ij}|e_i...f_j\rangle,$$

coupling states $|f_i...e_j\rangle$ to states $|e_i...f_j\rangle$.

The form of the couplings leads to the natural interpretation of an exchange of excitation from one site to another. We may for example consider a dimer of 3LS, where the biexciton coupling between site 1 and 2 is $K_{12}c_1^\dagger a_2$, both sites are in a singly-excited state and the eigenstate for the system is written as $|e_1e_2\rangle = |e_1\rangle \otimes |e_2\rangle$. The action of the $K_{12}c_1^\dagger a_2$ on the state $|e_1e_2\rangle$ creates a second excitation on site 1 from the operator $c_1^\dagger$ and a de-excitation on site 2 from the operator a_2. Thus, the final state we are left with in this case is then $|f_1g_2\rangle$. The two excitons have combined to create a doubly-exicted state on one site and ground state on the second site. If the system is coupled to a bath (see Sec. 4.2 below for details about system-bath coupling of 3LS), the state $|f_1g_2\rangle$ can subsequently relax to a state $|e_1g_2\rangle$. This particular process of two excitons first combining to create a doubly-excited state and then relaxing to a singly-excited state is exciton-exciton annihilation and cannot be modeled using solely 2LSs.

Given we have n sites, the electronic Hamiltonian is

$$H_{el} = \sum_{i=1}^{n}\left(\varepsilon_{e,i}a_i^\dagger a_i + \varepsilon_{f,i}c_i^\dagger c_i\right) + \sum_{j=i+1}^{n}\sum_{i=1}^{n}\left(J_{ij}a_i^\dagger a_j + K_{ij}c_i^\dagger a_j + L_{ij}c_i c_j^\dagger + h.c.\right). \tag{4.4}$$

We note that Eq. 4.4 above does not show for conciseness the various identity operators that are inserted in order for H_{el} to be expressed in the full system's Hilbert space $\mathcal{H}$. For a trimer of 3LS, setting all J_{ij} and L_{ij} to be 0, we

would have for example

$$\begin{aligned} H_{el,trimer} = &\left(\varepsilon_{e,1}a_1^\dagger a_1 + \varepsilon_{f,1}c_1^\dagger c_1\right)\otimes I_2 \otimes I_3 + I_1 \otimes \left(\varepsilon_{e,2}a_2^\dagger a_2 + \varepsilon_{f,2}c_2^\dagger c_2\right)\otimes I_3 + I_1 \otimes I_2 \otimes \left(\varepsilon_{e,3}a_3^\dagger a_3 + \varepsilon_{f,3}c_3^\dagger c_3\right) \\ &+ K_{12}c_1^\dagger \otimes a_2 \otimes I_3 + K_{13}c_1^\dagger \otimes I_2 \otimes a_3 + K_{23}I_1 \otimes c_2^\dagger \otimes a_3 \\ &+ K_{21}a_1 \otimes c_2^\dagger \otimes I_3 + K_{31}a_1 \otimes I_2 \otimes c_3^\dagger + K_{32}I_1 \otimes a_2 \otimes c_3^\dagger, \end{aligned} \tag{4.5}$$

where I_n are 3×3 identity matrices.

Just as for the systems in Chapter 2, the goal is to use this polymer model and simulate spectroscopic experiments, meaning we must define for each unit a transition dipole operator describing the light-matter interaction. For each site i, we define a transition dipole

$$\boldsymbol{\mu}_i = \boldsymbol{\mu}_{eg,i} + \boldsymbol{\mu}_{fe,i} + \boldsymbol{\mu}_{fg,i}, \tag{4.6}$$

where $\boldsymbol{\mu}_i$ is a Cartesian vector with x, y and z components and each dipole making up $\boldsymbol{\mu}_i$ represents one of the three possible transition that a 3LS can undergo when interacting with an incident electric field. The first term in Eq. 4.6, $\boldsymbol{\mu}_{eg,i}$, describes the $g_i \to e_i$ transition (and the opposite $e_i \to g_i$ transition), the $\boldsymbol{\mu}_{fe,i}$ term describes the $e_i \to f_i$ transition and the $\boldsymbol{\mu}_{fg,i}$ term the $g_i \to f_i$ transition. The three terms are respectively, in each possible x, y, z direction,

$$\mu_{eg,\alpha,i} = f_{\alpha,i}a_i^\dagger + f_{\alpha,i}^* a_i; \;\; \alpha = x, y, z, \; f_{\alpha,i} \in \mathbb{R},$$

$$\mu_{fe,\alpha,i} = h_{\alpha,i}c_i^\dagger + h_{\alpha,i}^* c_i; \;\; \alpha = x, y, z, \; h_{\alpha,i} \in \mathbb{R},$$

$$\mu_{fg,\alpha,i} = k_{\alpha,i}b_i^\dagger + k_{\alpha,i}^* b_i; \;\; \alpha = x, y, z, \; k_{\alpha,i} \in \mathbb{R},$$

where the constants $f_{\alpha,i}, h_{\alpha,i}$ and $k_{\alpha,i}$ and their complex conjugates are the amplitudes of each transition. We note that $f_{\alpha,i}$ with two subscripts is a dipole transition amplitude, not to be confused with the double excitation on sites, f_i. The full system's dipole for the n sites is then

$$\boldsymbol{\mu} = \boldsymbol{\mu}_{eg} + \boldsymbol{\mu}_{fe} + \boldsymbol{\mu}_{fg}, \tag{4.7}$$

where for example we have

$$\boldsymbol{\mu}_{eg} = \boldsymbol{\mu}_{eg,1} \otimes I_2 \otimes ... \otimes I_n + I_1 \otimes \boldsymbol{\mu}_{eg,2} \otimes ... \otimes I_n + I_1 \otimes I_2 \otimes ... \otimes \boldsymbol{\mu}_{eg,n}, \tag{4.8}$$

with similar expressions for $\boldsymbol{\mu}_{fe}$ and $\boldsymbol{\mu}_{fg}$.

Having now all the necessary mathematical expressions to characterize our polymer model, we describe how in practice H_{el} and $\boldsymbol{\mu}$ are computationally generated with the HLG for future use in spectroscopic calculations. For

closed systems, only three user inputs are necessary for creating both operators. The first input is a list of lists of the singly- and doubly-excited state energies $\varepsilon_{e,i}$ and $\varepsilon_{f,i}$ for each site of the n sites,

$$[[\varepsilon_{e,1}, \varepsilon_{f,1}], [\varepsilon_{e,2}, \varepsilon_{f,2}], ...[\varepsilon_{e,n}, \varepsilon_{f,n}]] \,.$$

The second input is another list of lists of the different coupling constants J, K and L,

$$[[J_{12}, J_{13}, ...J_{1n}, J_{23}, J_{24}, ...J_{n-1,n}], [K_{12}, K_{13}, ...K_{1n}, K_{23}, K_{24}, ...K_{n-1,n}], [L_{12}, L_{13}, ...L_{1n}, L_{23}, L_{24}, ...L_{n-1,n}]] \,.$$

The third and final input is a list of the dipole transition amplitudes $f_{\alpha,i}, h_{\alpha,i}$ and $k_{\alpha,i}$ for each Cartesian component,

$$\big[[[f_{x,1}, h_{x,1}, k_{x,1}], [f_{y,1}, h_{y,1}, k_{y,1}], [f_{z,1}, h_{z,1}, k_{z,1}]] \,,$$

$$[[f_{x,2}, h_{x,2}, k_{x,2}], [f_{y,2}, h_{y,2}, k_{y,2}], [f_{z,2}, h_{z,2}, k_{z,2}]] \,, ...$$

$$[[f_{x,n}, h_{x,n}, k_{x,n}], [f_{y,n}, h_{y,n}, k_{y,n}], [f_{z,n}, h_{z,n}, k_{z,n}]]\big] .$$

With these three inputs, the Hamiltonian generator part of the HLG will construct the full system operators in Eqs. 4.4 and 4.7. Shown below is Python code illustrating how to give the HLG the necessary input to create a dimer of 3LS in the closed case.

```
site_energies = [[1,2.2],[1,2.2]]
site_couplings = [[0.2],[0.1],[0.05]]
dipoles = [[[1,1,0],[0,0,0],[0,0,0]],
           [[1,1,0],[0,0,0],[0,0,0]]]
params = {'site_energies':site_energies,
          'site_couplings':site_couplings,
          'dipoles':dipoles}
```

The HLG will first create the individual site operators, including H_i, from the lists of site energies, and all creation and annihilation operators, again for each site. From the H_i and the three different couplings lists, it will then generate the full H_{el} in Eq. 4.4, inserting the identity operators I_n and Kronecker products $\otimes$ where necessary. Then, from the different creation operators and the lists of transition dipole amplitudes, it will generate $\boldsymbol{\mu}_{eg}, \boldsymbol{\mu}_{fe}$ and $\boldsymbol{\mu}_{fg}$, again inserting the identities and Kronecker product where needed and from those three dipoles, produce the full system's dipole in Eq. 4.7. All generated outputs are then saved into a file, which can be sent to one of the spectroscopic calculation modules of UFSS.

4.2 Open system generator

With the electronic Hamiltonian of Eq. 4.4 and the transition dipole of Eq. 4.7, we have all the necessary ingredients to perform simulations of nonlinear optical spectroscopies for a closed system, using the tools provided by UFSS. However, should we wish to instead study open system dynamics of polymers of 3LS, we must describe the system by its Liouvillian $\mathcal{L}_0$ rather than its Hamiltonian. Obtaining a Liouvillian thus involves having a Liouvillian generator for 3LSs, which is described in detail below.

We begin by defining the Liouvillian for an open system

$$\mathcal{L}_0 = -\frac{i}{\hbar} H_0 \otimes I_S + \frac{i}{\hbar} I_S \otimes H_0^T + i\hbar D, \tag{4.9}$$

The Liouvillian is an operator acting on the vector space $\mathcal{V}$ of linear operators acting on the Hilbert space $\mathcal{H}$ of H_0, with $\mathcal{L}_0$ generating the time evolution for the sytem's density matrix $\rho \in \mathcal{V}$. Here, H_0 is the system's Hamiltonian, which we generally assume has been outputed by the closed system generator beforehand. However, H_0 need not necessarily be outputed by the Hamiltonian generator described above; a user could instead generate a Hamiltonian using a different software and only use the tools of the HLG to treat the open system part of it, which is entirely encompassed in the dissipation superoperator D. So long as the necessary inputs are provided in the form expected by the HLG (the Hamiltonian, both its eigenvectors and eigenvalues, and the transition dipole $\boldsymbol{\mu}$ in the energy eigenbasis of H_0), the Liouvillian generator will be able to yield an expression for D.

As in Chapter 2, we seek a form of D arising from Redfield theory [16–18] (see Chapter 2 for a general discussion of such a form of D). Intra-manifold relaxation due to the coupling of an singly-excited site i to the bath is the same as that for a 2LS, given by the Redfield tensor

$$R_{SES} = R(a_i^\dagger a_i). \tag{4.10}$$

We must also include the coupling of the doubly-excited site, which is

$$R_{DES} = R(c_i^\dagger c_i). \tag{4.11}$$

Inter-manifold relaxation of a site i relaxing from a singly-excited state to its ground state is again

$$R_{1\to 0} = R(a_i^\dagger + a_i). \tag{4.12}$$

Since a three-level system can now also be in a doubly-excited state, there are two additional relaxation pathways to consider : the doubly-excited state to singly-excited state relaxation ($2 \to 1$), and the doubly-excited to ground

state relaxation ($2 \rightarrow 0$), which are given respectively by

$$R_{2\rightarrow 1} = R(c_i^\dagger + c_i), \tag{4.13}$$

$$R_{2\rightarrow 0} = R(b_i^\dagger + b_i). \tag{4.14}$$

The full dissipation operator D is thus

$$D = -\sum_i \left[R(a_i^\dagger a_i) + R(c_i^\dagger c_i) + R(a_i^\dagger + a_i) + R(c_i^\dagger + c_i) + R(b_i^\dagger + b_i)\right]. \tag{4.15}$$

In order to create D from Eq. 4.15 and subsequently $\mathcal{L}_0$ from Eq. 4.9, some inputs characterizing the bath must be given to the HLG, in addition to the site energies, couplings and transition dipoles necessary for the closed system generator. Below is a second example of how this procedure is implemented in Python code to create a dimer of 3LS with a Redfield system-bath interaction.

```
site_energies = [[1,2.2],[1,2.2]]
site_couplings = [[0.2],[0.1],[0.05]]
dipoles = np.array([[[1,1,0],[0,0,0],[0,0,0]],
                    [[1,1,0],[0,0,0],[0,0,0]]])
dipoles = dipoles.tolist()
# all site_baths should have 0 coupling ; there are no vibrations either
site_bath = {'cutoff_frequency':0.025,
             'coupling':0,
             'temperature':0.0,
             'cutoff_function':'lorentz-drude',
             'spectrum_type':'ohmic'}
vibration_bath = site_bath # add another site_bath for double excitation (ohmic lorentz-drude
site_bath2 = site_bath
# for 1-> 0 relaxation
relax_bath10 = {'relaxation_rate':kMtilde,
                'temperature':0.0,
                'spectrum_type':'white-noise'}
# for 2->1 relaxation
relax_bath21 = {'relaxation_rate':kM,
                'temperature':0.0,
                'spectrum_type':'white-noise'}
```

```
# no relaxation bath for 2 -> 0
Redfield_bath = {'secular':True,
                 'site_bath':site_bath,
                                'site_bath2':site_bath2
                 'vibration_bath': vibration_bath,
                 'site_internal_conversion_bath':relax_bath10,
                 'site_internal_conversion_bath21':relax_bath21}
params = {'site_energies':site_energies,
          'site_couplings':site_couplings,
          'dipoles':dipoles,
          'bath':Redfield_bath,
          'truncation_size':1,
          'vibrations':[]}
```

The code above illustrates how to use the novel features implemented in the HLG. After defining the closed system parameters as in the previous example for a closed system, we additionally specify the parameters for the bath. The dictionaries `site_bath` and `site_bath2` contain all the information necessary for the HLG to construct the Redfield tensors from Eqs. 4.10 and 4.11 describing intra-manifold relaxation processes. Next, we define the parameters for the $1 \rightarrow 0$ and $2 \rightarrow 1$ relaxations processes (contained in the "site_internal_conversion_bath" and "site_internal_conversion_bath21" dictionaries), which will be used to construct the tensors in Eqs 4.12 and 4.13, not including $2 \rightarrow 0$ relaxation in this system. We now have all the terms in Eq. 4.15 and we can thus generate the system's Liouvillian $\mathcal{L}_0$.

Choosing the numerical values in the code above, we may reproduce the Liouvillian for a pair of identical monomers of 3LS from Ref. [32]. This dimer model was initially manually replicated to be used in conjunction with UF^2 to study exciton-exciton interaction 2D in both the impulsive and finite pulse regime [27]. Using the HLG, we recreate the Liouvillian for this system, and compare the eigenvalues of this automatically generated $\mathcal{L}_{0,HLG}$ to the eigenvalues of the manually created $\mathcal{L}_{0,man}$, with the result shown in Fig. 4.2 below.

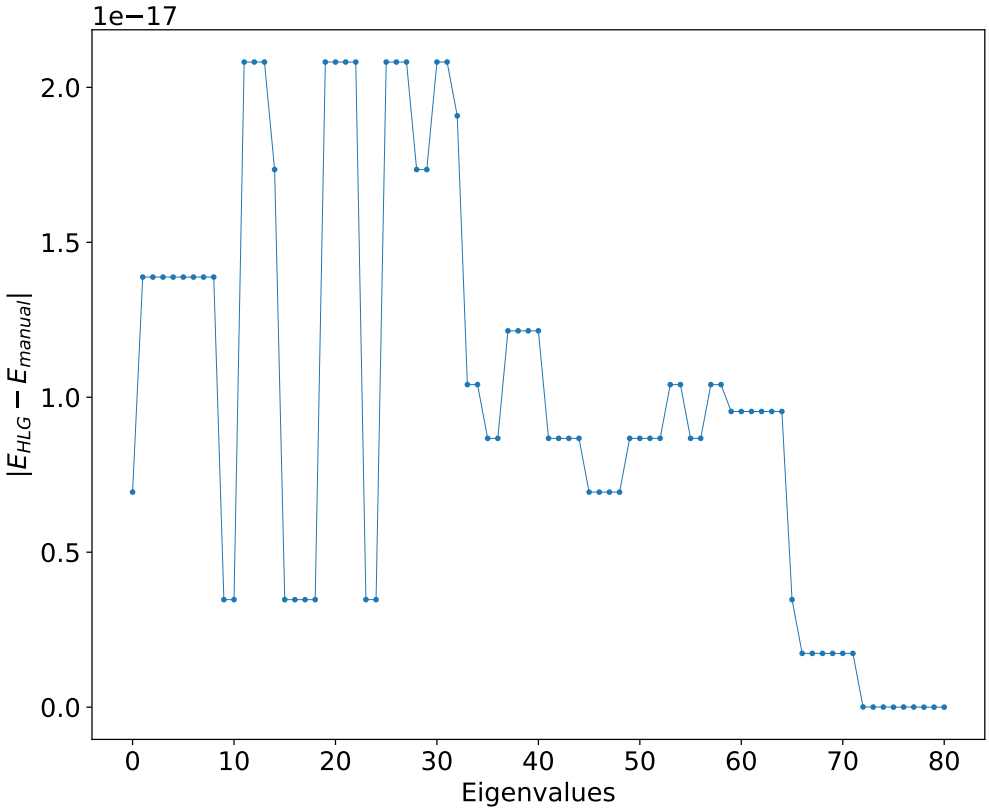

Figure 4.2: Absolute difference of automatically versus manually generated Liouvillians' eigenvalues for a dimer of 3LS. For 2 three-level systems, the dimensions of the Hamiltonian are $3^2 \times 3^2$ and is thus represented as a 9×9 matrix. The Liouvillian of this system is then of dimension $9^2 \times 9^2$ and can thus be represented by an 81×81 matrix (or equivalently as a $9 \times 9 \times 9 \times 9$ rank 4 tensor), hence the 81 eigenvalues on the x-axis. Note that the absolute differences in eigenvalues all fall within a range from 0 to $\approx 2 \times 10^{-17}$, meaning that those differences are smaller than the machine precision, indicating that we have correctly reproduced the system with the automated procedure.

The benefit of using the HLG to generate the dimer, or in fact any larger system, is two-fold : convenience and scalability. The convenience comes from the mathematical manipulations that are all automatically carried out when creating the operators necessary for calculations by the computer, such as inserting all identities and Kronecker products in Eqs. 4.5 or 4.8. In contrast, in the manual procedure, the creation operators $a^\dagger$ and $c^\dagger$ (and annihilation operators a and c), each monomer's Hamiltonian and transition dipoles must all be defined in their matrix form, along with the electronic coupling constants J, K, L. The next step involves inserting one by one the identity operators $I_{3\times3}$ and Kronecker product $\otimes$ where necessary to obtain the Hamiltonian H_0 and dipole $\boldsymbol{\mu}$ in the dimer's Hilbert space $\mathcal{H}$ using Eqs. 4.4 and 4.7. From there, the closed system's Liouvillian $\mathcal{L}_{closed} = -\frac{i}{\hbar}[H_0, I_S]$

can be generated. To treat the open system dynamics, the dissipation operator D must also be created by hand. In the case of this particular model, no intra-manifold relaxation occurs and thus only inter-manifold relaxation for the monomers is considered. Defining relaxation rates k_M and $\tilde{k}_M$ for the $f \rightarrow e$ and $e \rightarrow g$ processes respectively, D can be produced using Redfield formalism and subsequently added to $\mathcal{L}_{closed}$ to obtain the full system's Liouvillian $\mathcal{L}_0$. This manual generating procedure is involved, requiring that attention be paid not only to input parameter values but also to the definition of the different operators. In contrast, using the HLG solely requires the user to input parameter values in the format required, with all operators necessary for calculations being generated automatically. In practice, going from 2LS to 3LS only involves defining a handful of extra parameters.

The scalability advantage comes about when we wish to model larger systems. For a polymer of n 3LS monomers, there are up to $3\begin{pmatrix} n \\ 2 \end{pmatrix}$ electronic coupling terms in Eq. 4.4 and up to $9\begin{pmatrix} n \\ 2 \end{pmatrix}$ possible terms in Eq. 4.7. Procedurally inserting as many identitties in their proper position can pose a significant challenge. Furthermore, there are up $5n$ terms in Eq. 4.15 if all possible relaxation processes described by Eqs. 4.10 to 4.14 are included in the model and if each term is different. Overall, generating such a large number of individual terms is better handled via an automated process such as the one outlined above, which represents the main advantage of using the 3LS generator in its current form.

The three-level system generator has found its primary and so far only use in the simulations of spectroscopies. However, just as the two-level systems counterpart originally implemented in the HLG [22], the 3LS generator can be used independently of the other modules of UFSS.

Chapter 5

Explaining High-Order Transient Absorption Studies of a Squaraine Copolymer

The three-level system generator described in Chapter 4, while remaining a general purpose tool, was initially conceived with the goal of replicating a theoretical model used to describe squaraine-based copolymers [8], with the chemical structure of the particular molecules being modeled shown in Fig. 5.1 below. The objective is to use the 3LS model to explore experimental data posing a puzzle. These data were taken by Pavel Maly at Wurzburg University as part of [8], where studying a squaraine copolymer made of 38 monomers revealed a surprising and so far unobserved phenomenon in the high-order transient absorption signals, which was not discussed in Ref. [8].

Squaraine (SQ) dyes have recently garnered attention for their potential applications across different fields, ranging from materials in electronics to use in the biomedical realm. For photovoltaic applications, SQs can be used as light sensitizers in dye-sensitized solar cells [33, 34], electron donors in organic solar cells [35–40] and hole transporting materials or interfacial materials in perovskite solar cells [41–44]. In the case of biomedical applications, squaraines and SQ-based molecules have demontrated their usefulness as biosensors for sensing factors such as temperature, pH, ions and biomolecules [45–48], as biological imaging reagents [49, 50] or as photodynamic therapy reagents [51] and photothermal therapy reagents [52, 53]. The wide range of applications of squaraines naturally leads to a necessity of characterizing for example exciton transport or charge transfer processes occuring in molecules belonging to that class. Nonlinear spectroscopies are among the possible tools that can be used to probe the dynamical properties of such molecular systems.

The first section of this Chapter gives a theoretical description of the copolymer model from Ref. [8] in a form compatible with the three-level system generator of the previous chapter. The second section shows experimental

and simulated high-order TA spectra of copolymers of varying length, showing the surprising phenoemena of an average increase in signal amplitude as a function of nonlinear spectroscopy order in the ESA region, for short pump-probe delay times, with the increase disappearing at longer delay times. The last section provides a possible explanation for this phenomenon based on the properties of the electronic structure of the SQ copolymers.

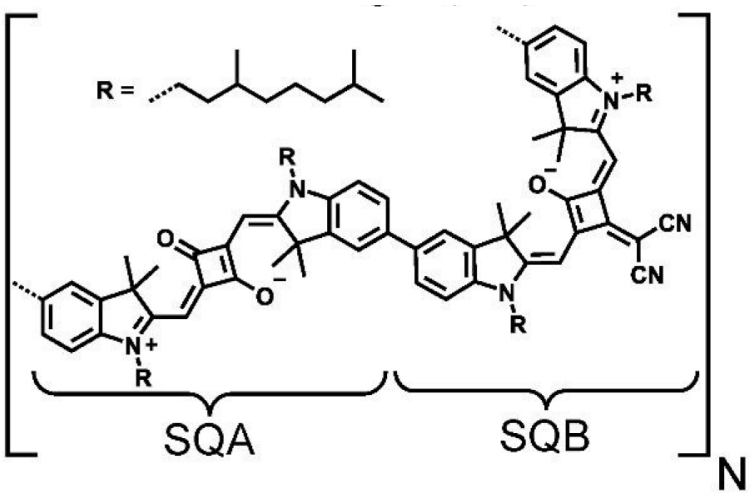

Figure 5.1: SQA-SQB copolymer chemical structure, taken from SI of Ref. [8]. The squaraines are uniquely characterized by and derive their name from the four carbon atoms approximately arranged in the shape of a square, forming a so-called squaric acid at the center of the molecule [ref]. The dashed lines at the bottom left and top right of the figure are the positions at which one SQ monomer will bond with a different SQ monomer. An SQB monomer will bond with an SQA monomer at the bottom left dashed line, while the opposite bonding process will occur between an SQA and SQB monomer at the top right dashed line.

5.1 Theoretical copolymer model

The theoretical model for the SQA-SQB copolymer was first described in the SI of [8] and was used in simulations of 5^{th}-order EEI2D spectroscopy rather than TA spectroscopy. We provide a shortened description of the main features of the model necessary for our own simulations.

Each copolymer unit is composed of a pair of two different monomer sub-units, which are simply named SQA and SQB respectively. As illustrated in Fig. 5.1, multiple copolymers bond to form an elongated chain of alternating SQA-SQB sub-units. A single copolymer is denoted as $P1$, two copolymers as $P2$ and so on, where PN corresponds in general to the number N of SQA-SQB pairs, meaning there are $2N$ monomers in total. The odd-numbered sites i are SQA monomers while the even-numbered sites are SQB monomers.

Each of the SQA and SQB monomers is modeled as a three-level electronic system, with differing singly- and doubly-excited state energies, denoted $\varepsilon_{e,A}, \varepsilon_{f,A}$ for SQA and $\varepsilon_{e,B}, \varepsilon_{f,B}$ for SQB, with Fig. 5.2 below showing an energy level diagram of a SQA-SQB dimer . Transition dipole moments from ground to singly-excited state for

each sub-unit are $\mu_A = \mu_{eg,A}$ and $\mu_B = \mu_{eg,B}$ respectively, and transition dipoles from singly-excited state to doubly-excited state are $\mu_A^f = \mu_{fe,A}$ and $\mu_B^f = \mu_{fe,B}$. 1-exciton coupling is given by J_{AB}, 2-exciton coupling is given by K_{AB} and there is no 3-exciton coupling L_{AB}. We consider only nearest neighbour coupling, such that $J_{ij}, K_{ij} = 0$ for $i - j > 1$.

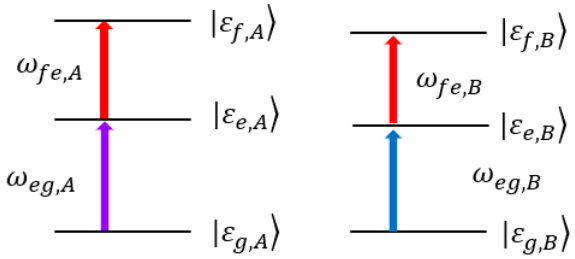

Figure 5.2: Scaled energy level diagram of an SQA-SQB copolymer. The red arrows, representing the transition energies from the singly- to the doubly-excited state on either one of the monomer, are the same, since the $\omega_{fe,A} = \varepsilon_{f,A} - \varepsilon_{e,A}$ and $\omega_{fe,B} = \varepsilon_{f,B} - \varepsilon_{e,B}$ transition energies are the same in this model. The purple arrow represents the transition from ground state to singly-excited state on the SQA monomer, with energy $\omega_{eg,A} = \varepsilon_{e,A} - \varepsilon_{g,A}$, while the blue arrow represents the same transition on the SQB monomer, with energy $\omega_{eg,B} = \varepsilon_{e,B} - \varepsilon_{g,B}$.

The authors of Ref. [8] treat the bath using Redfield theory. Intra-manifold relaxation due to the eletronic site-bath couplings is characterized using a spectral density of the form

$$J_i^O(\omega) = \nu_i^O \left(2\lambda\Lambda \frac{\omega}{\omega^2 + \Lambda^2} + \frac{2S\Omega^3\omega\gamma}{(\Omega^2 - \omega^2)^2 + \omega^2\gamma^2} \right), \quad i = 1, .., 2N, \; O = e, f. \tag{5.1}$$

The ν_i^O is a bath scaling factor. The SQA and SQB have different bath coupling factors for singly-excited state coupling (denoted ν_A^e and ν_B^e) and doubly-excited state coupling (denoted ν_A^f and ν_B^f), meaning each monomer couples differently to the environment. The first term in the parentheses is the Ohmic term with a Lorentz-Drude cutoff of the same kind seen in Chapters 2 and 4. The second term in parentheses represents the coupling of a single underdamped vibrational mode with frequency Ω, which is included in the bath instead of being treated explicitly as part of the system. There are no other modes of vibrations included explicitly. λ is the so-called reorganization energy, Λ is the inverse correlation time, S is the Huang-Rhys factor of the coupling to the singly strongly coupled vibrational mode of the system and γ is the damping of that vibrational mode. Inter-manifold relaxation considers a flat spectral density of the form seen in Chapter 2, with relaxation times for $2 \to 1$ and $1 \to 0$ transitions τ_{IC} and τ_R respectively. The values for all parameters of the model, which are used both in Ref. [8] and in this thesis as a baseline description of the copolymers, are shown in Table 5.1 below.

Variable	Value
$\varepsilon_{e,A}$,$\varepsilon_{f,A}$	14700 cm^{-1},26900 cm^{-1}
$\varepsilon_{e,B}$,$\varepsilon_{f,B}$	13500 cm^{-1},25700 cm^{-1}
J_{AB}	-420 cm^{-1}
K_{AB}	-840 cm^{-1}
μ_A,μ_A^f	1.2; 0.4
μ_B,μ_B^f	1; 0.33
ν_A^e, ν_A^f	1; 4
ν_B^e, ν_B^f	1.66; 6.64
λ	180 cm^{-1}
Λ	300 cm^{-1}
Ω	1280 cm^{-1}
γ	10cm^{-1}
S	0.18
τ_{IC}	30 fs
τ_R	$(1710,2-61.9N)$ ps

Table 5.1: Parameters used for copolymer model simulations, from Ref. [8]

We note a few key characteristics of the model. The singly to doubly-excited state transition energies for both the SQA and SQB are the same at 12200cm^{-1}, meaning this transition is red-shifted with respect to the ground to singly-excited state transition energy for each monomer. This in turn implies that in the energy eigenbasis of the system, one doubly-excited state will in general have lower energy than multiple singly-excited states. The transition dipoles for the $1 \rightarrow 2$ transition, μ_A^f and μ_B^f, are 3 times smaller than the $1 \rightarrow 0$ transitions, μ_A and μ_B, meaning the former transitions are much weaker than the latter. In the same vein, the doubly-excited states site-bath couplings scaling factors $\nu_{A,B}^f$ are 4 times larger than singly-excited states scaling factors $\nu_{A,B}^e$, causing the peaks in a TA spectrum associated with the $1 \rightarrow 2$ transitions to have broad lineshapes. Lastly, we note the different time scales on which the inter-manifold relaxation processes occur. The $2 \rightarrow 1$ relaxation described by the relaxation time τ_{IC} occurs on the 10s of femtoseconds scale, while the $1 \rightarrow 0$ relaxation process, described by the relaxation time τ_R (which is dependent on the number N of SQA-SQB pairs), occurs on the nanosecond scale, meaning there are roughly 6 orders of magnitude separating the two relaxation pathways. This illustrates the fact that in this model, exciton-exciton annihilation takes place at early times, whereas single excitons are long-lived and diffuse over the entire length of the polymer.

To include inhomogeneous broadening of the signals caused by the slightly different environment surrounding each monomer, we convolve the signals in frequency-domain with a Gaussian distribution of standard deviation

$\sigma_{IB} = \frac{\omega_0}{9}$, with $f_0 = \frac{\omega_0}{2\pi} = 1\text{eV}$, chosen such that the simulated spectra match, by eye, the experimental spectra of Fig. 5.3.

All values in Table 5.1 were chosen by the authors of Ref. [8] and subsequently used for the simulations in Sec. 5.2. The values for the parameters related to the singly-excited state (the energies $\varepsilon_{e,A}$,$\varepsilon_{e,B}$, transition dipole moments μ_A and μ_B, the site-bath coupling parameters λ, Λ, Ω,etc.) were taken from a study on SQA-SQB dimers [54] and slighty adjusted to better fit the experimental data, except for the one-exciton coupling J_{AB}, which was taken from a different study on squaraine copolymers [55],[56]. The parameters related to the doubly-excited states (the energies $\varepsilon_{f,A}$,$\varepsilon_{f,B}$, transition dipole moments μ_A^f and μ_B^f, the site-bath coupling parameters) were chosen to be similar to the singly-excited states parameters. The $\varepsilon_{f,A}$,$\varepsilon_{f,B}$ energies were derived from a linear absorption spectrum, shown in the SI of Ref. [8], as is the internal conversion time τ_{IC} characterizing exciton-exciton annihilation.

5.2 Experimental and simulation results

Experimental TA spectra of various nonlinear orders were obtained by the authors of [8] (though the results shown below were not part of Ref. [8]) for a P19 copolymer (a copolymer made of 19 SQA-SQB pairs, for a total of 38 monomers), using ultrafast 14 fs pump and probe laser pulses, with the results displayed in Fig. 5.3. The signals measured were of 3^{rd}- up to 13^{th}-order in perturbation theory (see Sec. 3.5 for a brief overview of higher order transient absorption spectroscopies), denoted $PP^{(3)}$ through $PP^{(13)}$, for delay times T from 0 fs to 5 ps and averaged over different time ranges to study both short- and long-time behaviour of the system.

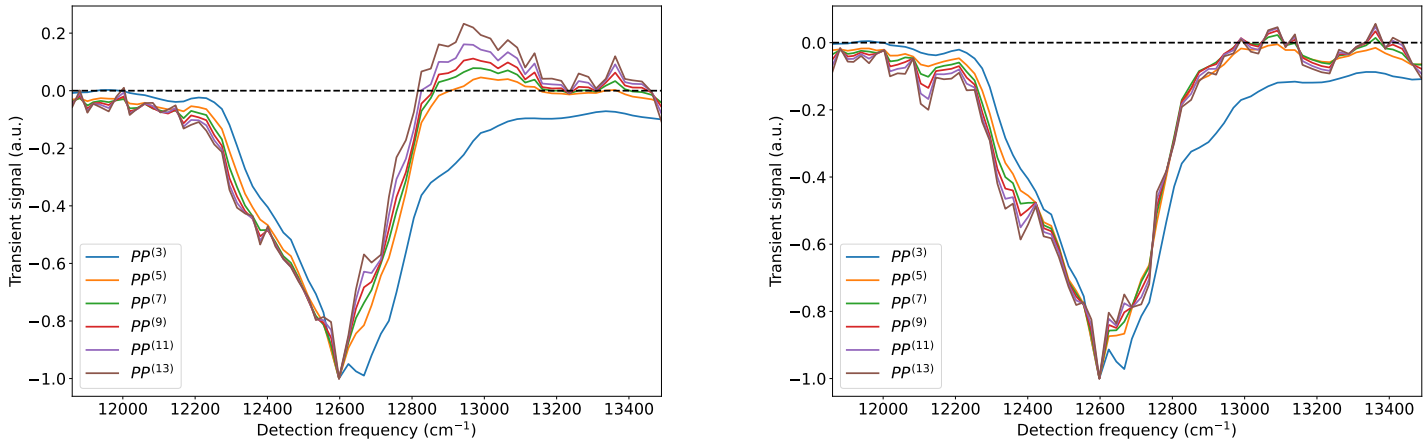

Figure 5.3: Normalized experimental high-order TA spectra for P19 copolymer. The signals are averaged over (a) all delay times (0 to 5 ps), and (b) over later delay times (2 to 5 ps), after exciton-exciton annihilation is completed. At every order, the TA signal is normalized with respect to the ground-state bleach signal, such that the GSB's amplitude is -1. Panel (a), which accounts for times where exciton-exciton pairs are still present in the system, shows that the ESA signal's amplitude increases with respect to the GSB peak as a function of the TA order. At later delay times, when exciton-exciton annihilation has occured and only single exciton states remain, the higher-order signals are almost identical.

The positive signals around 12600 cm are the ESA signals; we note that the 3$^{\text{rd}}$-order signal is always negative when normalizing the spectra with respect to the ground state bleach peak around $-0.01\,\omega_0$. The unnormalized signals are shown in Fig. 5.4 below, where we can observe that the signals reduce in magnitude as the order increases and also alternate in sign. The left panel of Fig. 5.3 shows that 1) the positive ESA signals increase linearly in amplitude as a function of the nonlinear TA order, starting from 5$^{\text{th}}$-order and 2) that the ESA peaks are redshifted, again as a function of signal order. The right panel of Fig. 5.3 shows that at later times, the high-order signals are roughly on top of each other. These phenomena have not been previously observed and thus necessitate an explanation. The first goal is therefore to replicate the early-time ESA signal amplitude increase and redshift with TA order and the later-time signal collapse in a simulation using the copolymer model parameters. The second goal is to provide a physically-backed explanation for the long-time part of this behaviour where the high-order signals roughly lie on top of each other.

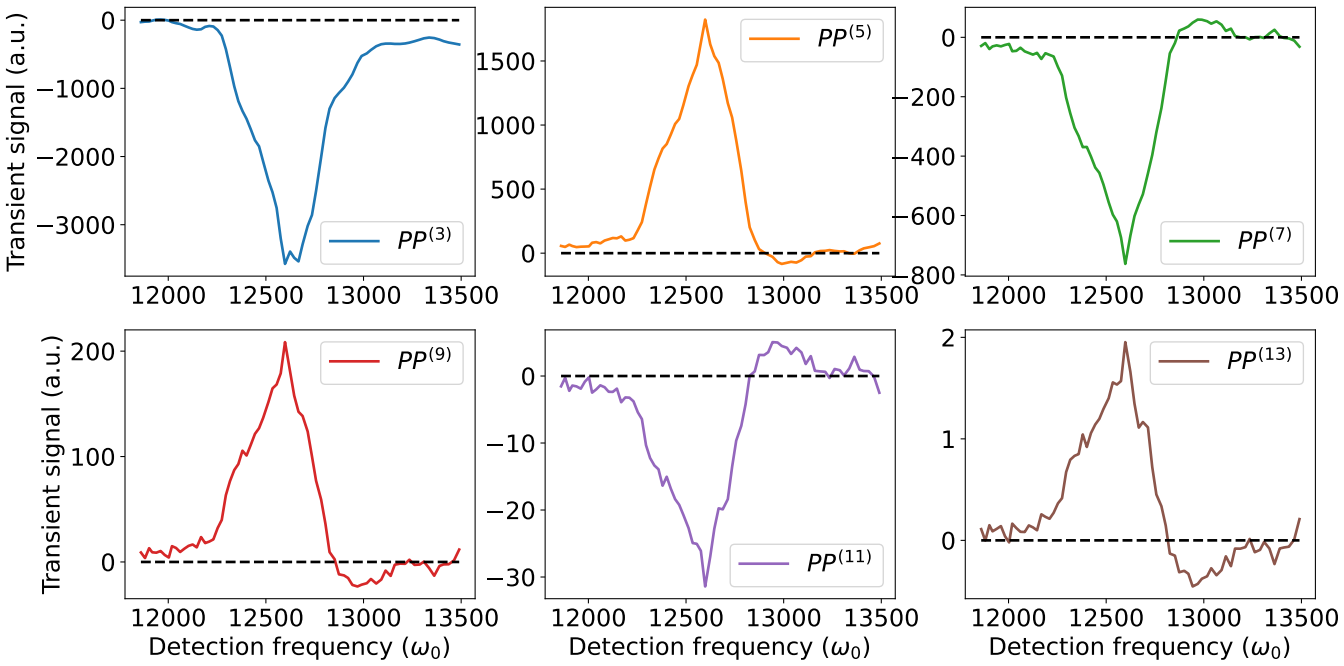

Figure 5.4: Unnormalized experimental high-order TA spectra for P19 copolymer. The signal at each order is the average of all signals at that order over 5 ps, as in Fig. 5.3 (a), except that there is no normalization with respect to the negative GSB peak. The 3$^{\text{rd}}$-, 7$^{\text{th}}$- and 11$^{\text{th}}$-order signals have a negative peak at $-0.01\,\omega_0$ (which is the peak associated with the GSB signal in Fig. 5.3), while the 5$^{\text{th}}$-, 9$^{\text{th}}$- and 13$^{\text{th}}$-order signals have a positive peak at this frequency. The magnitude of the signal diminishes as the TA order increases, as can be noted by the scale of the y-axes for the different panels.

Using our three-level system generator, we are able to reproduce the copolymer model, albeit for a smaller number of dimer pairs than for the experimental result, due to the memory cost of simulating a 38-unit long polymer, with the cost on the order of $\sim$ 1000 TB. The user is free to specify how many copolymer pairs are simulated by changing a single parameter, with the only limitation being available memory. All parameters in Table 5.1 are given as inputs in a Python script, which generates all the necessary inputs that the HLG requires to create the copolymer model's Liouvillian $\mathcal{L}_0$ and transition dipole $\boldsymbol{\mu}$ needed for spectroscopy calculations. All the HLG's generated output are then sent to UFSS's signal calculation algorithm UF^2 to obtain high-order TA signals.

Figure 5.5 below shows simulated high-order TA spectra (from 3$^{\text{rd}}$- to up 13$^{\text{th}}$-order for smaller systems) averaged over delay times of 0 to 1 picosecond, for P1 to P4 copolymers, obtained with UF^2 and using impulsive pulses rather than 14 fs pulses, as the impulsive pulses well approximate 14 fs pulses for these systems.

To understand why this is the case, we can compare the time scales over which system dynamics occur compared to the duration of the pulse, using the parameters in Table 5.1. Looking for example at the J_{AB} and K_{AB} constants,

which dictate how quickly excitons move from one site to another, those phenomena correspond to times of roughly 80 fs and 40 fs respectively, which is between 3 to 6 times longer than a 14 fs pulse. Similarly, looking at the $2 \rightarrow 1$ relaxation time τ_{IC}, we see that it is 30 fs, over twice as long as the pulses, while the $1 \rightarrow 0$ relaxation time is 6 orders of magnitude larger. The dephasing parameters λ, Λ, γ and Ω correspond to time scales between 26 fs and 3335 fs, which are again longer times than the pulse duration. Since the 14 fs pulses used are already short enough to resolve all dynamics present in the model, we may assume that they are well approximated as impulsive pulses when compared to the time scales over which said dynamics occur. Using finite yet ultrashort pulses would thus result in no substantial change in the resulting spectra, while drastically increasing calculation time, and we thus resort to using only impulsive pulses.

Since all systems simulated in this chapter are much smaller than the real system, we do not expect the spectra for P1-P4 to look exactly the same as the spectra for P19, as is indeed the case when comparing Fig. 5.5 and Fig. 5.7 to Fig. 5.3 . The first objective is to be able to reproduce the phenomenon of increasing ESA signal amplitude as a function of TA order and the collapse of higher-order signals at longer delay times, rather than exactly reproducing the spectra themselves. If this rise at early times, before EEA has completed, and the collapse at longer timers, after EEA has occured, are both observed in the simulations despite the shorted polymers, we are still able to use the current model to study the phenomena.

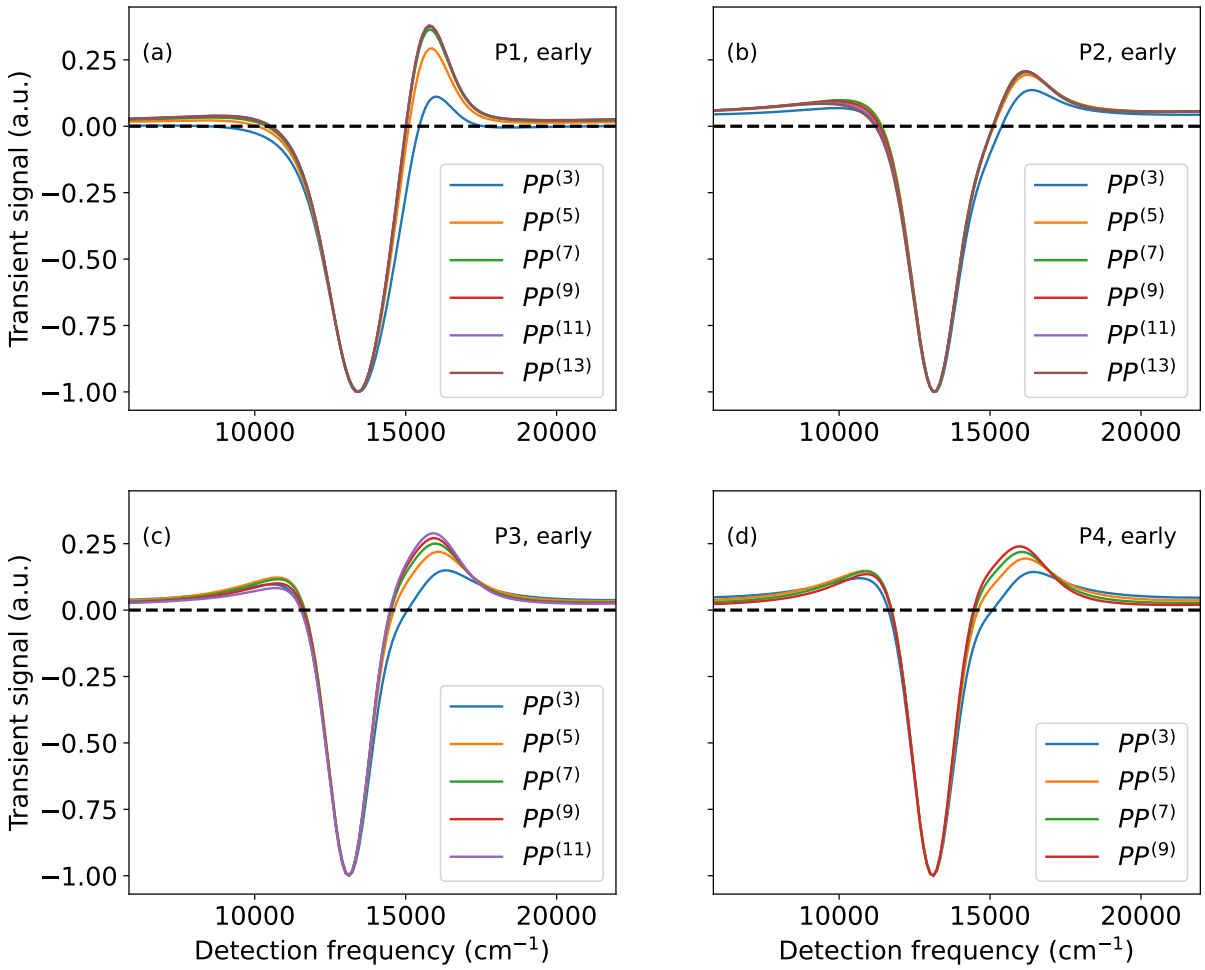

Figure 5.5: Simulated high-order TA spectra for (a) P1 (b) P2 (c) P3 and (d) P4 squaraine copolymers, using the model parameters from Table 5.1. The simulations were done at delay times T ranging from 0 to 5 ps, with steps of 250 fs, with the spectra above being averaged from 0 to 1 ps at all orders and normalized such that the largest negative peak corresponding to the GSB signal has amplitude -1, as in the experimental spectra of Fig. 5.3. The signals were obtained after a convolution with a Gaussian distribution of standard deviation $\sigma_{IB} = \frac{\omega_0}{9}$. We note that for the two largest systems, P3 and P4, the highest order of TA signal obtained is limited to the 11^{th}-order and 9^{th}-order signal respectively, due to computational cost of simulating higher order spectroscopies for larger systems.

The four spectra in Fig. 5.5 show that at early delay times, when exciton-exciton pairs are still present, simulations with the copolymer model are able to reproduce the ESA peak amplitude increase as a function of TA order, for different system sizes. Although the separation of the different nonlinear orders becomes more apparent as the size of the polymer increases, all systems exhibit the phenomenon to various degrees, further validating the fact that this effect is a generic feature of the model, rather than a special case that only occurs for larger systems.

As previously mentioned, contrary to the spectra of Fig. 5.3(a), which are obtained after averaging signals over all T from 0 picoseconds to 5 picoseconds, all spectra in Fig. 5.5 are obtained after averaging the signals over the first picosecond only. Due to the systems being simulated having a much smaller size compared to the experimetal

system, EEA occurs on shorter time scale, since the P1 to P4 squaraines are shorter than the P19, causing exciton pairs to meet and annihilate more quickly. This faster average annihilation time in turn causes the higher-order signals in the simulation to collapse on each other at shorter times than what is observed in the experiment. Figure 5.6 below shows the difference between averaging the signals over the first ps and averaging over all delay times, for P1 and P4 copolymers. For both systems, the averaging over all delay times results in all higher-order signals being nearly identical to the 3rd-order signal, meaning the multi-exciton phenomena have vanished faster than for the larger P19 system, justifying our different choice for the averaging range.

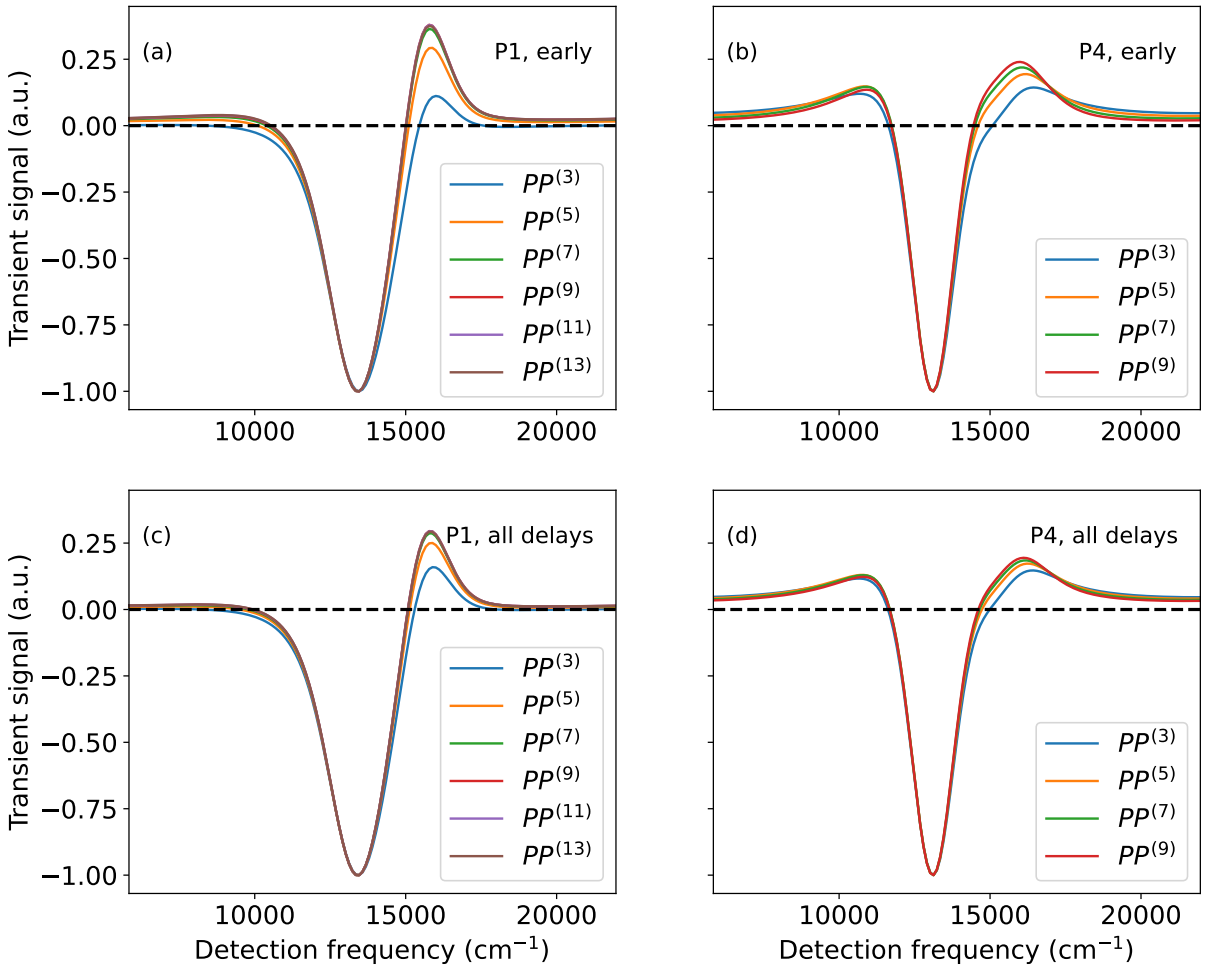

Figure 5.6: Simulated high-order TA spectra for P1 (panels (a) and (c)) and P4 (panels (b) and (d)). Both panels (a) and (b) are reproduced from Fig. 5.5(a) and (d) respectively, with the signals being averaged over delay times up to 1 ps. The two bottoms panels, (c) and (d), show the signals averaged over all delay times, from 0 ps to 5 ps. In the second case case, since exciton-exciton annihilation has been completed within the first picosecond, the high-order signals are nearly identical at all order after that delay time. This in turn causes the averaged signals to also look nearly identical over the full range of delay times.

If we now average the signals over later delay times, from 2 ps to 5 ps, as in Fig. 5.3(b), we want that signals at all orders to lie on top of each other and be similar, for all system sizes, which is precisely what is observed in Fig. 5.7 below. For all copolymers from P1 to P4, the 5$^{\text{th}}$-order and above TA signals are the same as the 3$^{\text{rd}}$-order signal, meaning all spectroscopies report on the same dynamics of the system at longer delay times.

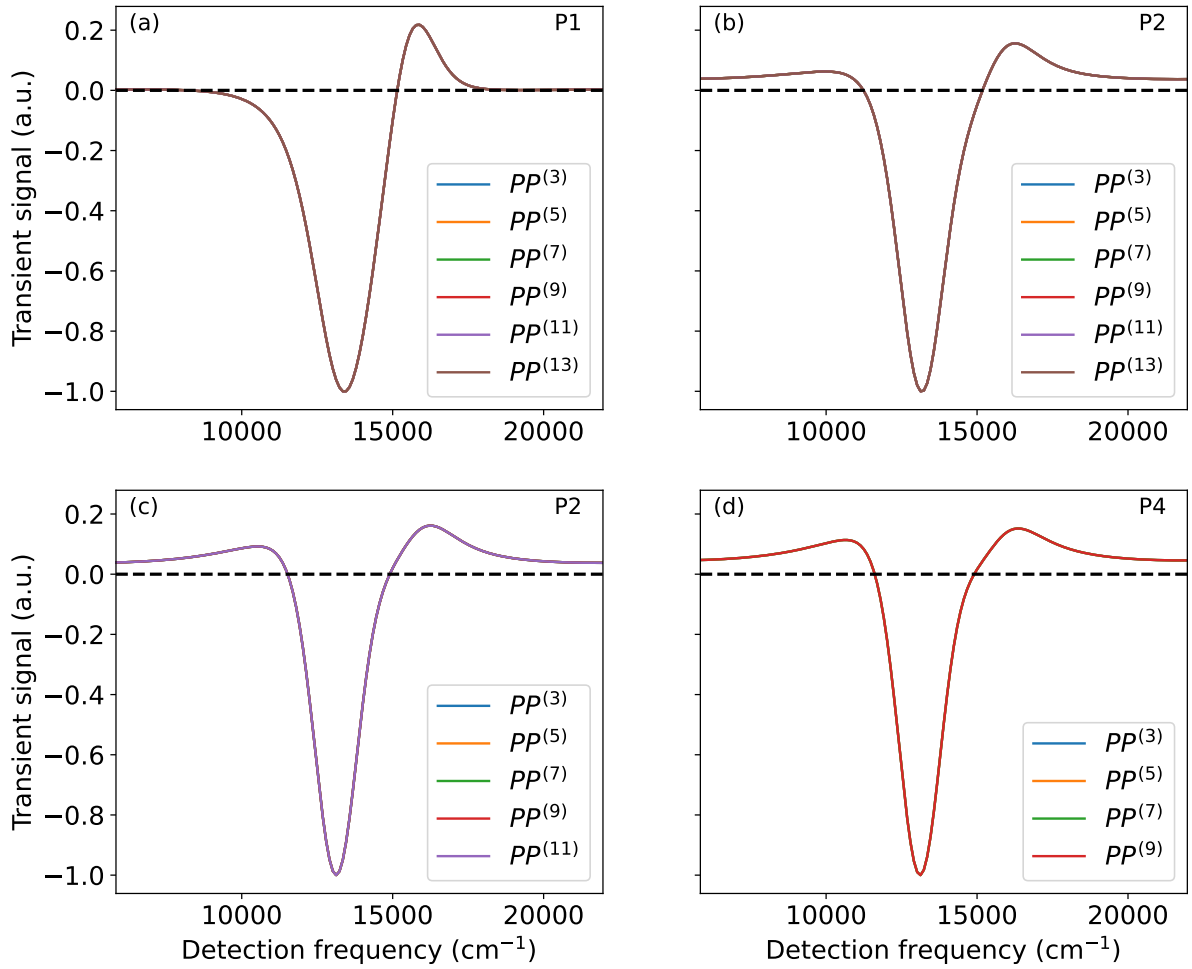

Figure 5.7: Late-time simulated high-order TA spectra averaged over delay times from 2 ps to 5 ps for (a) P1 (b) P2 (c) P3 and (d) P4 squaraine copolymers. The simulations were done at delay times T ranging from 0 to 5 ps, with steps of 250 fs and averaged over the last 3 ps, from 2 ps to 5 ps, similarly to the spectrum of Fig. 5.3(b).

We may look at the signals for the P3 copolymer at various single delay times rather than an average of the signals and study the time scale over which exciton-exciton annihilation occurs. Figure 5.8 below shows three TA spectra at delay times of 0, 0.1 ps and 0.2 ps. The left panel shows that at 0 delay time, the ESA signals are well separated from each other and increase at all orders. The middle panel shows that at $T = 0.1$ ps, exciton-exciton annihilation has not yet finished since there is still separation of the signals, with the right panel showing that at 0.2 ps the spectra are identical to the middle panel. From this, we may infer that on average, all exciton-exciton pairs will annihilate within the first 200 fs for this smaller system.

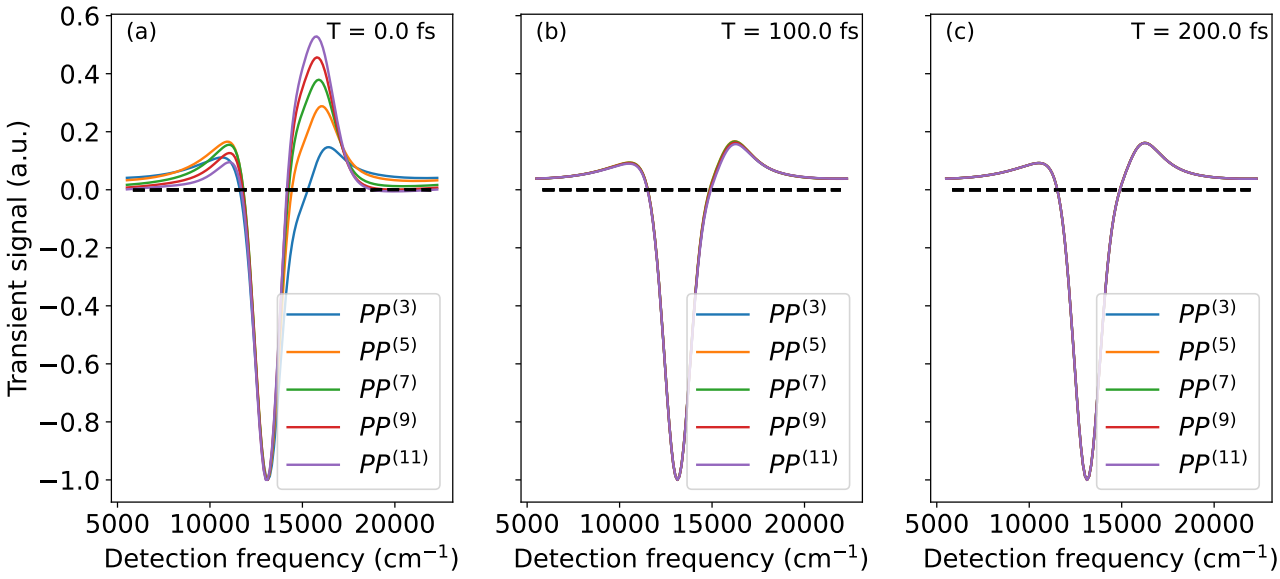

Figure 5.8: Simulated high-order TA spectra for P3 copolymer at delay times T of (a) 0 ps (b) 0.1 ps and (c) 0.2 ps. At $T = 0$, the signals are all separated from each other at all orders. At $T = 0.2$ ps, all signals have collapsed on each other , meaning EEA has completed within 0.1 ps and 0.2 ps.

Taking the P3 model as an example, we have successfully reproduced the experimental observations of short-term ESA peak enhancement and redshift, as can be seen when comparing panel (a) of Fig. 5.8 to panel (a) of Fig. 5.3. All TA signals, including the 3$^{\text{rd}}$-order one, are seperated from each other, with the signal amplitude increasing as a function of spectroscopy order. Also visible is the redshift of the ESA peaks as a function of the frequency ω_0, again as a function of nonlinear order.

At later delay times, we have managed to reproduce the experimental results where the signals at all orders are similar (where for P1 through P4, they are in fact all identical, as can be seen from Fig. 5.7).

Having reproduced all 3 phenomena in our simulations for different sizes of polymers, we provide, in the following section, an explanation of the origins of the signal collapse at later times.

5.3 ESA signal collapse : a matter of relaxation

Having been able to reproduce the rise in the ESA signal's amplitude as a function of TA order at early times and the subsequent collapsing of the signals at later times, we must now provide a physical picture related to the paramaters of the model presented in Sec. 5.1 that is capable of explaining the collapse of the orders at large T.

In order to understand what causes the higher-order ESA signals to look identical to the 3$^{\text{rd}}$-order ESA signal after a short delay time with the original set of parameters from Table 5.1 and why this collapsing is related to the energies and dipole transition amplitudes of the doubly-excited states of the squaraines A and B, we must study the

character of the states at the bottom of each excitation manifold after the interaction of the system with the pump pulse but before the arrival of the probe pulse, which are occupied after the intra-manifold relaxation time. The reason we focus on the intra-manifold relaxation processes is that in this model, they occur on a short timescale, within 20 fs to 100 fs. This can be seen in Fig. 5.9 for a simulation of a P3 copolymer, where the signals at different orders look similar between $T = 20$ fs and $T = 100$ fs, indicating that intra-manifold relaxation has completed within that time interval, before EEA has completed, which happens at around 200 fs as shown in Fig. 5.8.

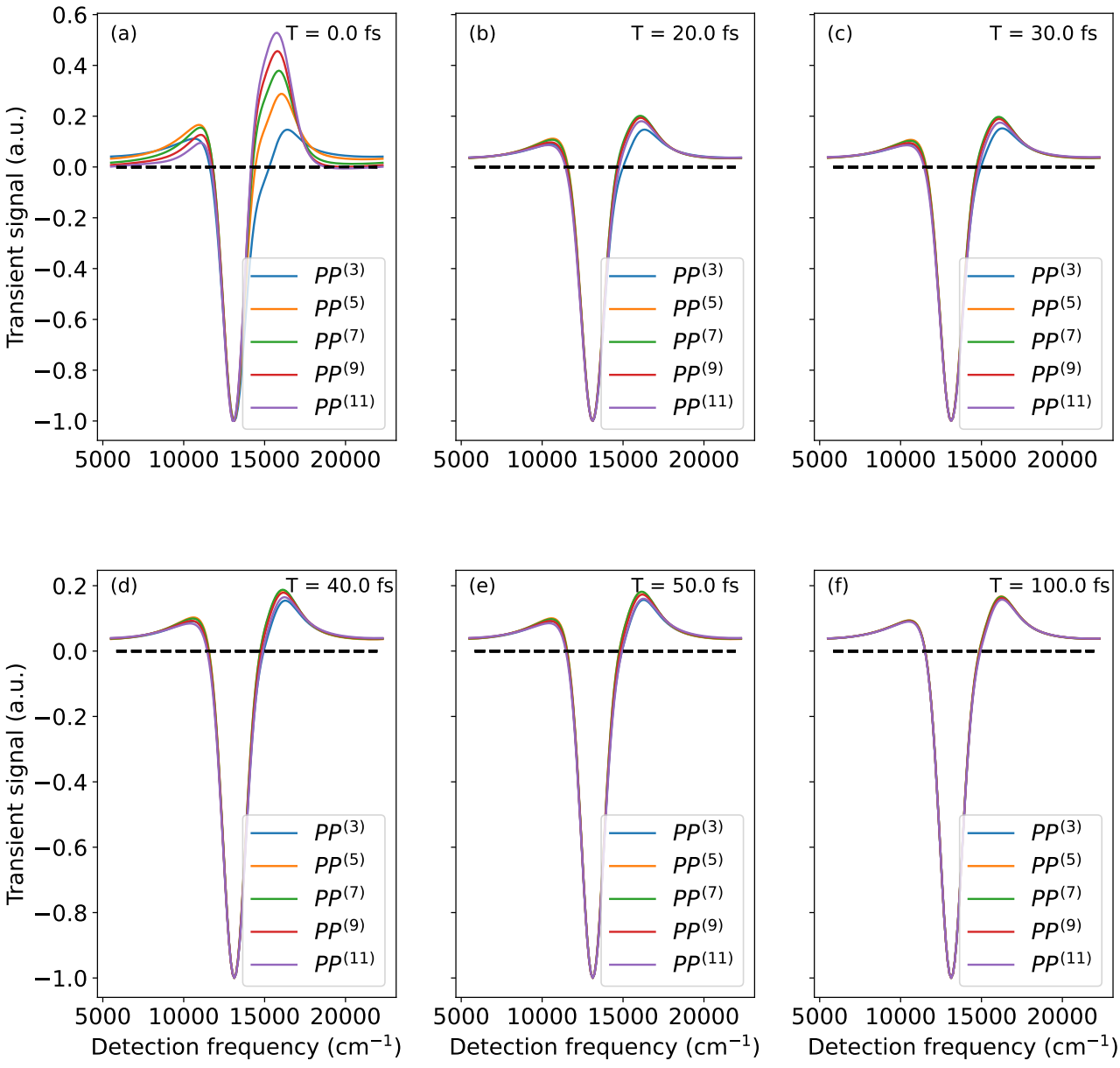

Figure 5.9: Simulated high-order TA spectra for P3 copolymer at delay times T of (a) 0 fs (b) 20 fs (c) 30 fs (d) 40 fs (e) 50 fs and (f) 100 fs. Within the first 20 fs, the intra-manifold relaxation processes have cause the higher-order signals to collapse roughly on top of each other.

To further ensure that the two processes of EEA and intra-manifold relaxation are not competing with each other on that time scale, we rerun the same simulation for P3, this time setting the τ_{IC} relaxation time to a larger value of 300 fs, which dictates the rate at which EEA occurs. Again, we see that the high-order signals have mostly collapsed on each other, even before EEA has had a chance to complete.

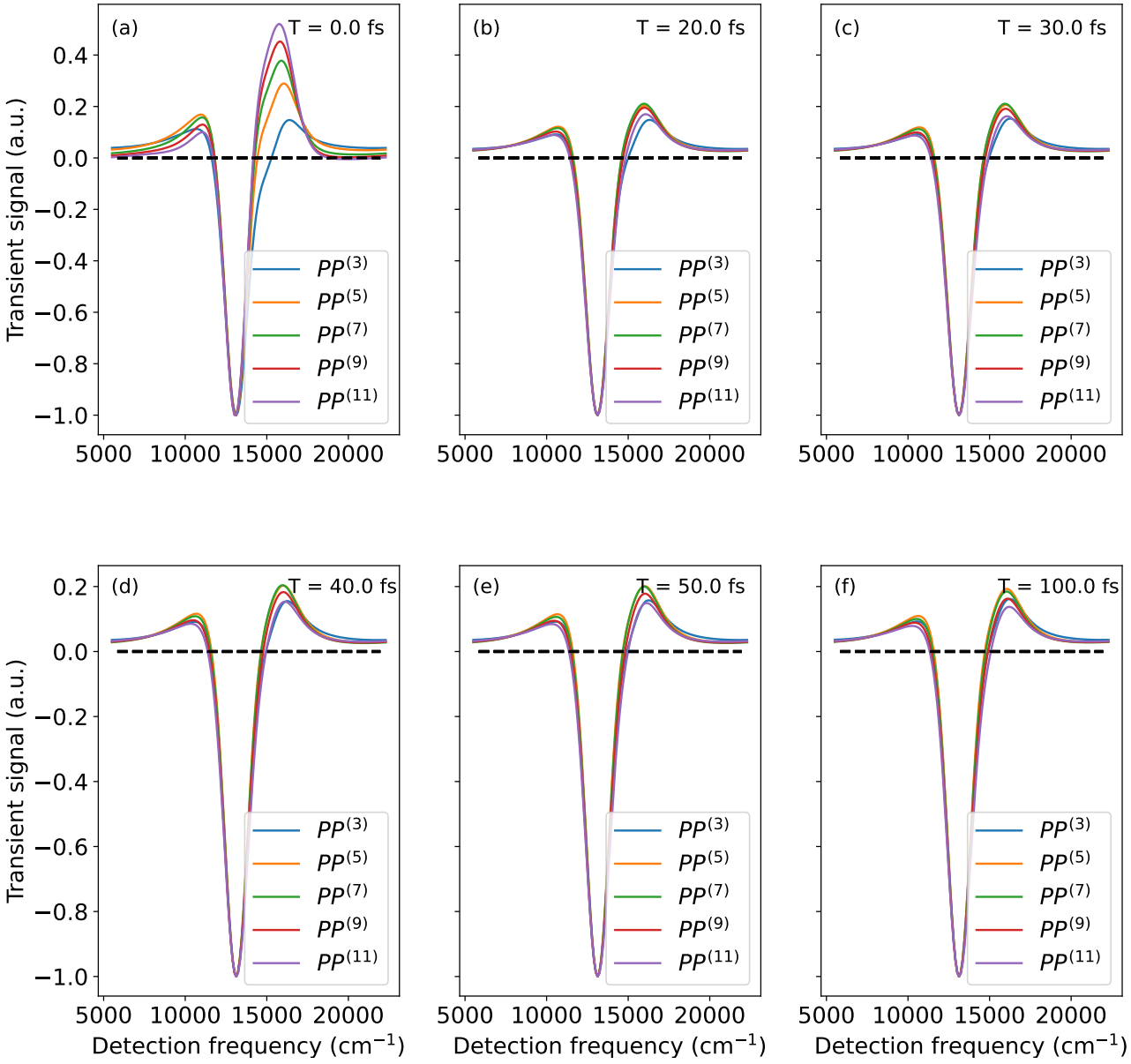

Figure 5.10: Simulated high-order TA spectra for P3 copolymer at delay times T of (a) 0 fs (b) 20 fs (c) 30 fs (d) 40 fs (e) 50 fs and (f) 100 fs. The parameters are the same as those in Table 5.1, except for $\tau_{IC} = 300$ fs. This implies that on average, exciton-exciton pairs will annihilate at a later time than the scale on which intra-manifold relaxation occurs.

In the first case with the initial parameters, for both squaraines, the $e \rightarrow f$ transition has lower energy than the

$g \to e$ transition, meaning that states of the form $|ee\rangle$, where two different sites have a single exciton, have higher energy than states of the form $|fg\rangle$, where one site has a double exciton; note that we avoid writing the states as $|g_1 g_2 ... e_i ... e_j ... g_n\rangle$ or $|g_1 g_2 ... f_i ... g_j ... g_n\rangle$ and so on for both conciseness and clarity.

The redshift of the $e \to f$ transition energies with respect to the $g \to e$ transition energies causes the states within an excitation manifold higher than the singly-excitation manifold (SEM) to relax, after intra-manifold relaxation, occupying the lower-energy states with $|f\rangle$ character rather than the higher-energy states with $|e\rangle$ character. To understand what is meant by character in this context, we may look at the first few manifolds (ground, singly-excited, etc. up to quadruply-excited manifold, QEM) after intra-manifold relaxation. In the ground-state manifold (GSM), no relaxation occurs and there is only a single state of the form $|gg\rangle$ where all sites are unexcited. In the SEM, we have states of the form $|eg\rangle$. These are single-exciton states, which are thus states with $|e\rangle$ character. In the DEM, we have two excitons, where after intra-manifold relaxation but before EEA, the lowest energy states have both excitons on a single site, and we have that the lowest energy states have amplitude (and therefore probabilities) mostly in the $|fg\rangle$ states. States of this form are thus said to have mostly $|f\rangle$ character. In the triply-excited manifold (TEM), again after intra-manifold relaxation, the lowest energy states $|fe\rangle$ states have the largest amplitude, and finally, in the QEM, states of the form $|ff\rangle$ are occupied with the highest probability. Figure 5.11 belows shows a visual representation of the first few energy levels that are occupied after intra-manifold relaxation for the DEM, TEM and QEM for a P3 copolymer, and the probabilities for the bottom level to be in the different states presented above are also given.

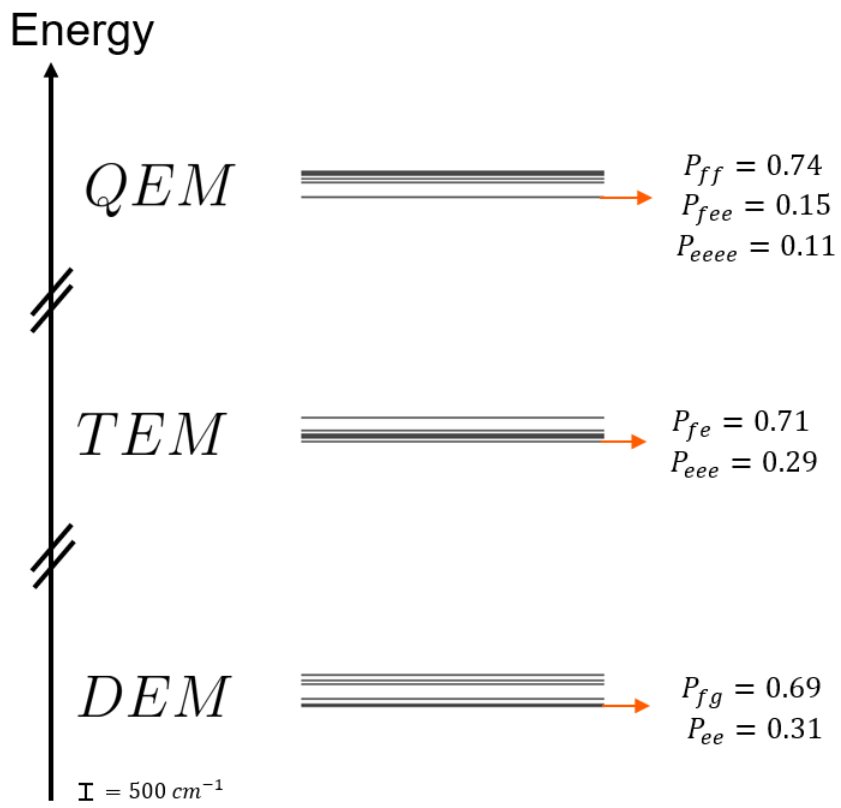

Figure 5.11: Energies of the lowest six states in each of the DEM, TEM and SEM manifolds with the original set of parameters for a P3 copolymer. These states are the most likely to be occupied after intra-manifold relaxation. The probabilities that the lowest energy level in each manifold has various excitation characters are shown. With the original parameters, the lowest-energy states are much more likely to have f-type character than ee-type character.

With the experimentally determined model parameters, the transition dipole amplitudes μ_A^f and μ_B^f are small compared to the μ_A and μ_B transition amplitudes, the $e \to f$ (and $f \to e$) transitions are much weaker than the $g \to e$ (and $e \to g$) transitions. Those weaker transitions in turn imply that for states in the SEM, transitions of the form $|eg\rangle \to |ee\rangle$ are stronger than those of form $|eg\rangle \to |fg\rangle$. For states in the DEM, transitions of the form $|fg\rangle \to |fe\rangle$ are stronger than those of the form $|fg\rangle \to |eg\rangle$, meaning that signals emitted from probing the states in the DEM will mimic the signals from probed states in the GSM, since $|fg\rangle \to |fe\rangle$ and $|gg\rangle \to |eg\rangle$ are similar transitions, occuring at the same frequencies and with the same transition dipoles. In the TEM (now taking into account more than just two sites), transitions of the form $|feg\rangle \to |fee\rangle$ are stronger than those of form $|feg\rangle \to |ffg\rangle$, meaning that the transitions from the fully relaxed states in the TEM have similar frequencies and amplitudes to transitions from the fully relaxed states in the SEM. Therefore, those transitions in the TEM mimic the transitions occuring to states in the SEM. Similarly, in the QEM, the stronger transitions are of the form $|ffg\rangle \to |ffe\rangle$, mimicking transitions from states in the DEM and therefore transitions from states in the GSM. Overall, the higher-excited manifolds reached by the higher-order interactions from the pump pulse will replicate

the signals from states in either the GSM or the SEM, which are the only manifolds that can be probe with 3rd-order TA spectroscopy. Figure 5.12 is a visual representation of possible transitions from the bottom energy state in the SEM to states in the DEM and transitions from the bottom energy in the TEM to states in the QEM.

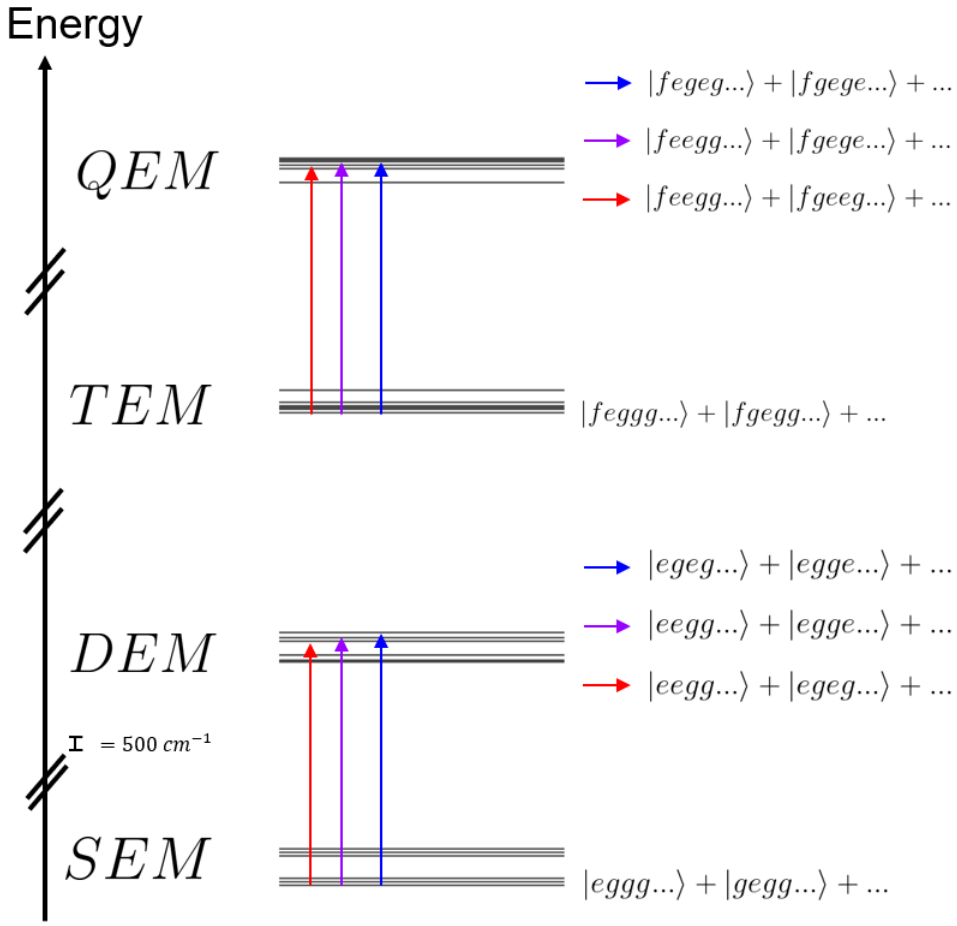

Figure 5.12: Possible transitions from the bottom energy state in the SEM to different states in the DEM and from the bottom energy state in the TEM to different states QEM, after intra-manifold relaxation, for a P3 copolymer with initial parameters. The coloured arrows represent the transition from the bottom state to the state identified by an arrow of the same colour. For example, the red transition from state $|eggg...\rangle + |gegg...\rangle$ is associated to the $|eegg...\rangle + |egeg...\rangle$ state next to the red arrow in the DEM. With the initial parameters, transtions from the bottom of the SEM to the DEM are similar to transitions from the bottom of the TEM to the QEM, as the $e \rightarrow f$ transitions are heavily suppressed in this case.

In contrast, with the set of modified parameters, where the $e \rightarrow f$ transition energies are now blueshifted with respect to the $g \rightarrow e$ transition energies, states of the form $|fg\rangle$ are the higher energy states within each manifold, rather than states of form $|ee\rangle$ as with the initial parameter set. Thus, between the interaction from the pump pulse and the probe pulse, intra-manifold relaxation causes states within an excitation manifold to relax to states with mainly $|ee\rangle$ character instead of mainly $|fg\rangle$ character, with Fig. 5.13 below showing a representation of some

of the possible states that are occupied after intra-manifold relaxation for the DEM, TEM and QEM similarly to Fig. 5.11, with the modified parameters. Comparing for example the bottom energy levels of the QEM in Figs. 5.11 and 5.13, we see that for initial parameters, the bottom level has a probability of 0.74 to be in a state of form $|ff\rangle$, a probability of 0.15 to be in a state of form $|fee\rangle$and a probability of 0.11 to be in a state of form $|eeee\rangle$, in contrast with the lowest-energy state with the modified parameters, where the probabilities to be in states of the same form are 0.24, 0,30 and 0.46 respectively.

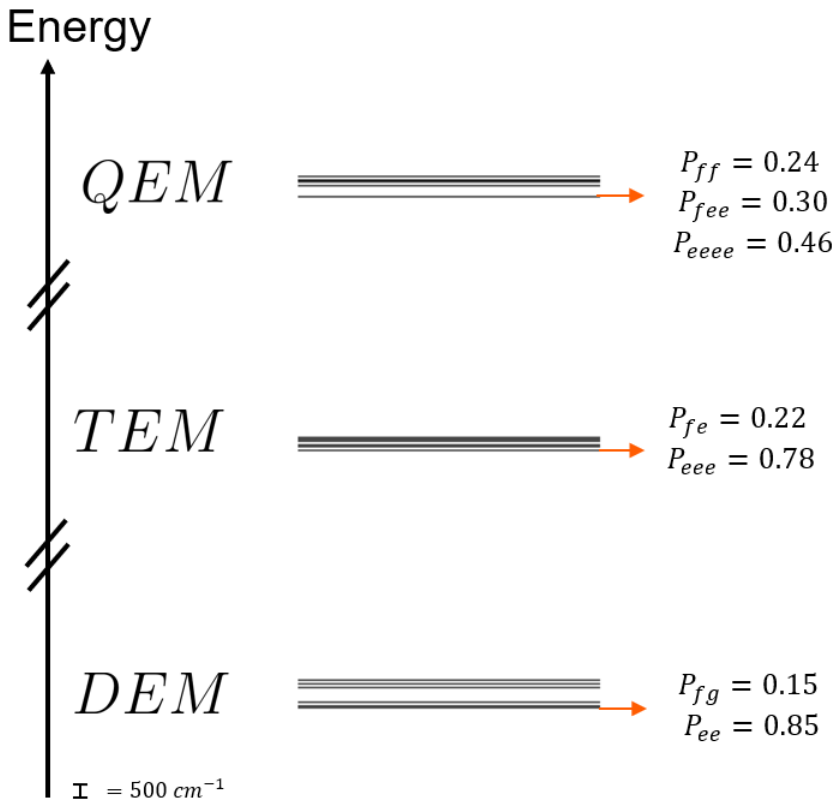

Figure 5.13: Energies of the lowest six states in each of the DEM, TEM and SEM manifolds for a P3 copolymer with the modified set of parameters. These states are the most likely to be occupied after intra-manifold relaxation. As in Fig. 5.11, the orange arrows at the bottom energy level of each manifolds point to the different probabilities of that level of being in a particular state. In contrast to Fig. 5.11, here the lowest energy states are unlikely to be found in f states.

This effect should both change the form of the spectra and reduce the EEA rate, as the excitons are more likely to stay separate with the new model. We may once again analyze which states are the lowest energy states in the manifolds and compare the possible transitions in the current scenario with those using the first set of parameters. The states in the GSM and SEM are unchanged since no double excitons or pairs of single excitons exist in either manifold. In the DEM, after intra-manifold relaxation, states of form $|ee\rangle$ are now occupied preferentially over $|fg\rangle$ states. The transition dipole amplitudes μ_A^f and μ_B^f are now equal to μ_A and μ_B transition amplitudes for

each monomer, the $e \rightarrow f$ and $g \rightarrow e$ transitions are now equal in amplitude, meaning that the transitions from $|ee\rangle \rightarrow |fe\rangle$ and $|ee\rangle \rightarrow |ge\rangle$ are equally strong and since $|ee\rangle \rightarrow |fe\rangle$ is different from $|gg\rangle \rightarrow |eg\rangle$, the signals from probed states in the DEM do not mimic those from probe states in the GSM. In the TEM, we now have mostly states of form $|eeeg\rangle$ rather than $|fegg\rangle$. Going from either $|eeeg\rangle \rightarrow |feeg\rangle$ or $|eeeg\rangle \rightarrow |eeee\rangle$ yield equally strong transitions. Since in the SEM the only occupied states have mostly $|egg\rangle$ character, the system can go from this state to $|ggg\rangle$, $|fgg\rangle$ or $|ege\rangle$ with equal amplitude. However, there are fewer transition possibilities for states in the SEM than for states in the TEM and thus the two manifolds do not mimic each other. In the QEM, the occupied states are predominantly of the form $|eeeeg\rangle$, and thus the probe pulse causes transitions to states of form $|feeeg\rangle, |geeeg\rangle, |eeeee\rangle$ and so on and, similarly to the TEM, the QEM does not in this case mimic a lower excitation manifold, leading to overall different signals at different orders, given that higher-order spectroscopies probe higher manifolds.

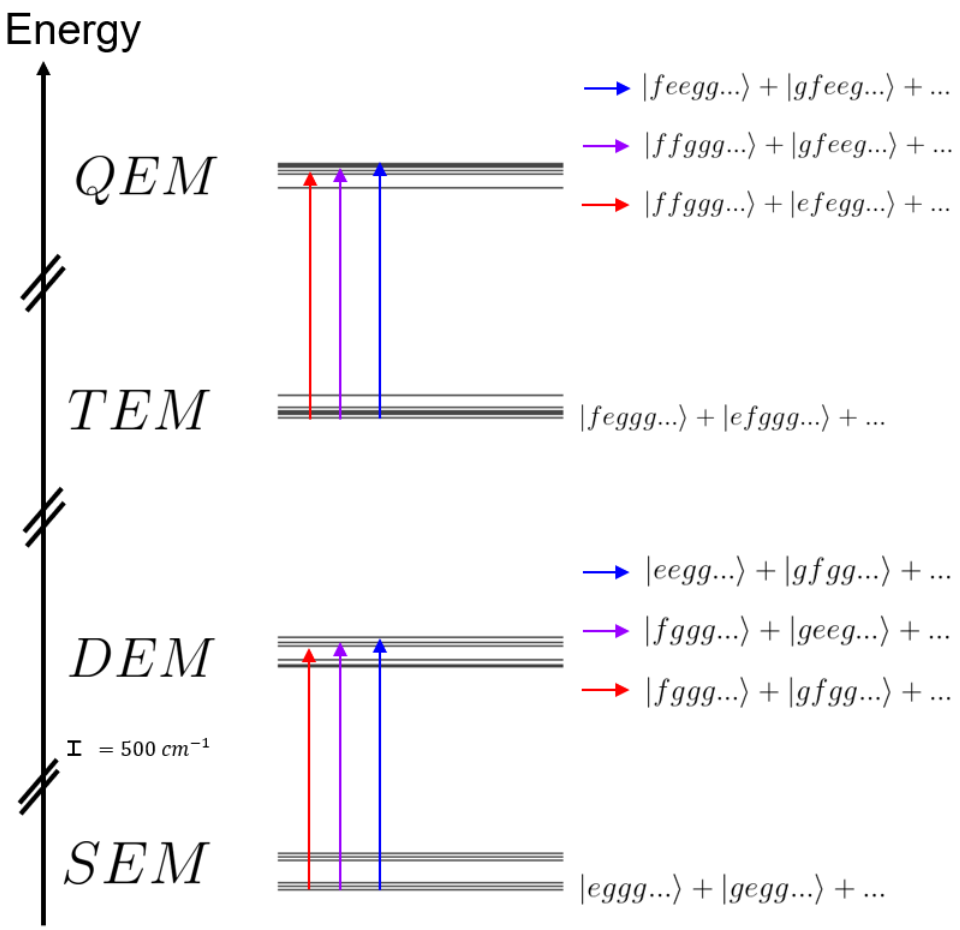

Figure 5.14: Possible transitions from the bottom energy state in the SEM to different states in the DEM and from the bottom energy state in the TEM to different states QEM, after intra-manifold relaxation, for a P3 copolymer with modified parameters. With the modified parameters, transitions from the bottom of the SEM to the DEM are not similar to transitions from the bottom of the TEM to the QEM, as the $e \rightarrow f$ transitions are as strong as the $g \rightarrow e$ ones, and the states with multiple single-excitons ($|ee\rangle$-type states) have significant amplitude at the bottom of a manifold.

With the theory and hypothesis in mind, we now may modify certain model parameters from Table 5.1 to observe their effect on the simulated spectra and test the validity of our hypothesis as the explanation of the cause of the phenomenon.

We set the $\varepsilon_{f,A} - \varepsilon_{e,A}$ and $\varepsilon_{f,B} - \varepsilon_{e,B}$ transition energies, originally set at 12200 cm^{-1} for both SQA and SQB monomers, to now be larger than the $\varepsilon_{e,A} - \varepsilon_{g,A}$ and $\varepsilon_{e,B} - \varepsilon_{g,B}$ transition energies, which were set at 14700 cm^{-1} and 13500 cm^{-1} respectively. We also set $\mu_A^f = \mu_A$ and $\mu_B^f = \mu_B$, rather than being three times smaller as with the original parameters.

With this new set of parameters, we simulate 3^{rd}-order to 11^{th}-order TA spectroscopy on a P3 copolymer, at the same three delay times as the spectra in Fig. 5.8, with the results shown in Fig. 5.15 below.

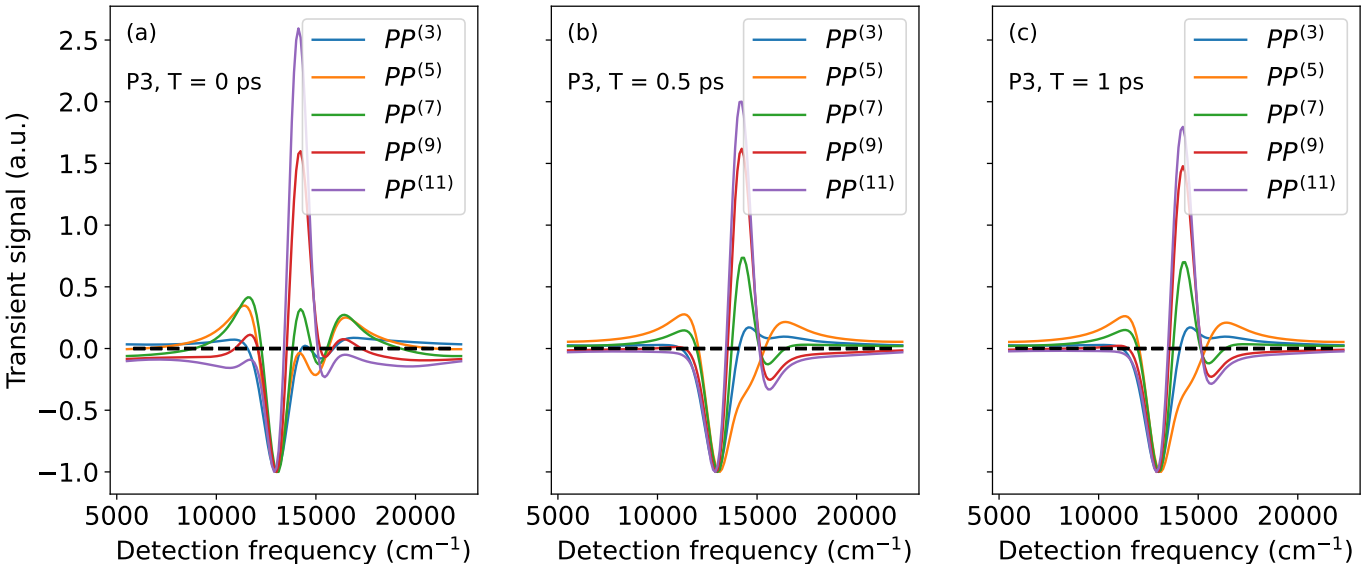

Figure 5.15: Simulated high-order TA spectra for P3 copolymer with modified parameters, at delay times T of (a) 0 ps (b) 0.5 ps and (c) 1 ps. In this particular model, the $\varepsilon_{f,A} - \varepsilon_{e,A}$ and $\varepsilon_{f,B} - \varepsilon_{e,B}$ transition energies are both blueshifted with respect to the $\varepsilon_{e,A} - \varepsilon_{g,A}$ and $\varepsilon_{e,B} - \varepsilon_{g,B}$ transition energies, and are set at 18300 cm^{-1} . The SQA and SQB transition dipole amplitudes μ_A^f and μ_B^f are set to have the same value as their μ_A and μ_B transition dipoles amplitudes, with $\mu_A = \mu_A^f = 1.2$ and $\mu_B = \mu_B^f = 1$. As before, signals at all orders are normalized such that the GSB signal has an amplitude of -1; we note that with this set of parameters, the ESA signals are stronger than the GSB signals, in contrast to the previous simulations shown in Fig. 5.8.

Comparing the three panels in Fig. 5.15 for the P3 system with modified parameters to the three panels of Fig. 5.8, we can see that at delay times of 0.5 ps and 1 ps, the ESA signals at different orders are all well separated, in stark contrast to the low- and high-order ESA signals being all identical at the same delay times when using the parameters that best describe the experiment. Looking at spectra obtained at much longer delay times, shown in Fig. 5.16, we eventually recover the signal collapsing behaviour where all 3^{rd}- to 11^{th}-order lie on top of each other. However, the phenomenon occurs on the order of $\approx$ 10 ps, compared to roughly $\approx$ 1 ps when using the initial parameters.

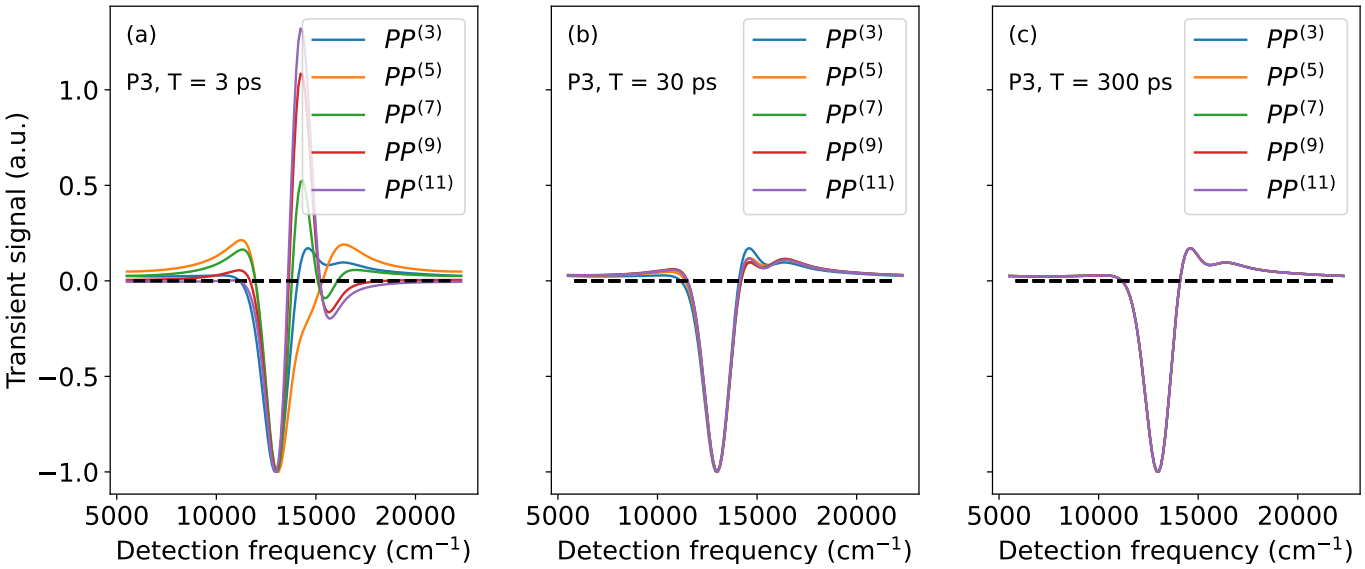

Figure 5.16: Simulated high-order TA spectra for P3 copolymer with modified parameters, at delay times T of (a) 3 ps (b) 30 ps and (c) 300 ps.

Simulations for a large P4 copolymer with modified parameters show that the same trend seen in Figs. 5.15 and 5.16 can be observed. The top three panels of Fig. 5.17 show that the 3^{rd}-,5^{th}-,7^{th}- and 9^{th}-order signals are all separated in the first picosecond, and remain separated even at a delay time of $T = 30$ ps, compared to the P3 copolymer where all signals have become identical at that time. However, like with the P3 model, the TA signals for P4 at a later delays of $T = 300$ ps are all identical. The observeration of the separation of the higher-order signals at early times for systems of different sizes (P3 and P4) when using the modified parameters indicates that the phenomenon is a generic feature of the model rather than a particular case only applicable to a unique system size.

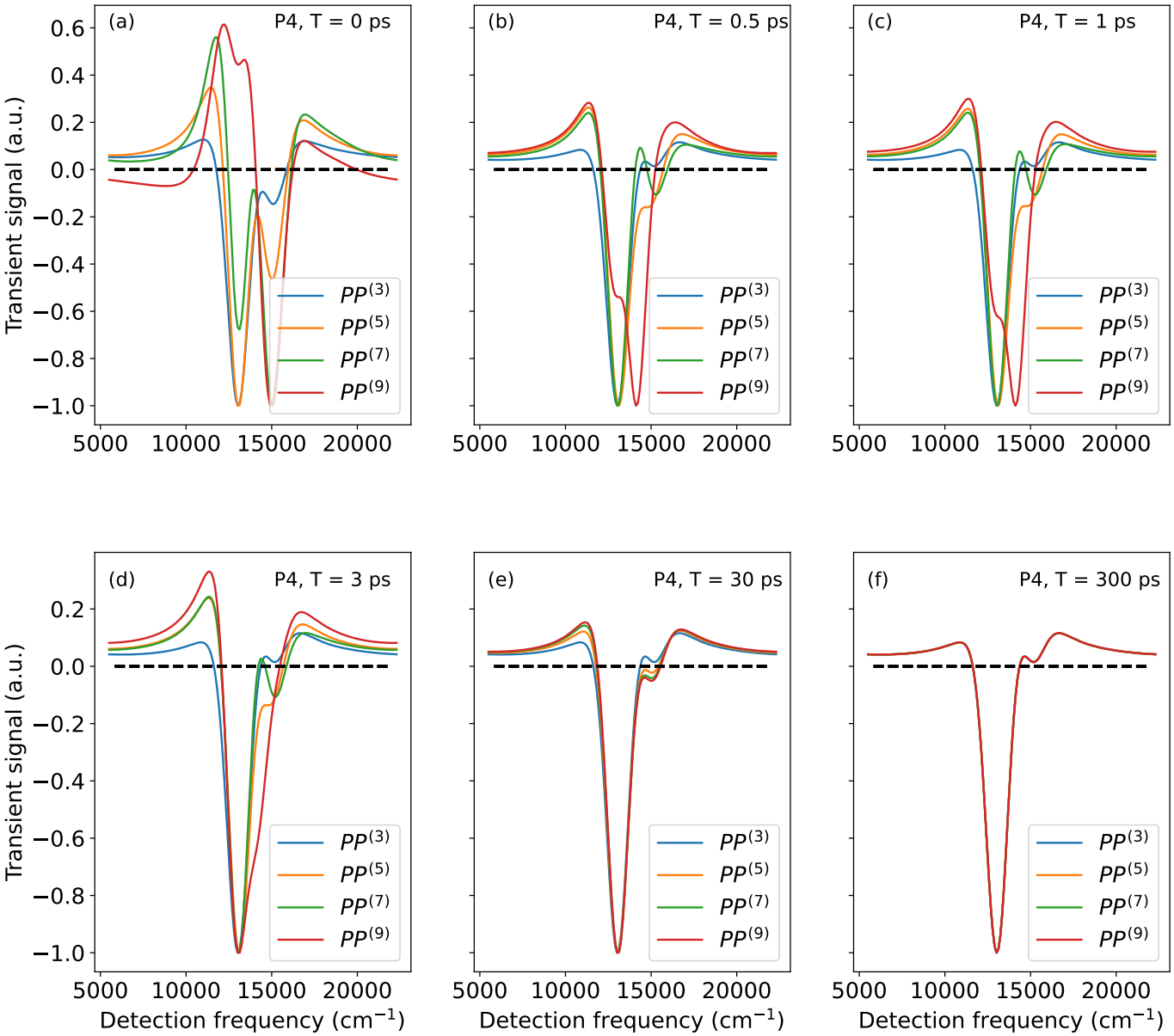

Figure 5.17: Simulated high-order TA spectra for P4 copolymer with modified parameters, at delay times T of (a) 0 ps (b) 0.5 ps and (c) 1 ps. (d) 3 ps (e) 30 ps and (f) 300 ps.

Since the experimental results shown in Fig. 5.3 do not exhibit this separation of signals at long delay times, we can conclude that the physical system is more aptly described by three-level systems with the parameters from Table 5.1 rather than the modified set of parameters with redshifted doubly-excited states. More importantly, we have an understanding of the physical cause of the high-order signals collapse, which is the presence of a favorable energetic pathway towards having two excitons on the same site instead of separated excitons on different sites.

This chapter has presented how the 3LS generator described in Chapter 4 can be utilized to first simulate an arbitrary number of squaraine dimer pairs. Using the newly added tools of the 3LSG submodule of the Hamilto-

nian/Liouvillian module of UFSS, we can use all the parameters found in Table 5.1 as inputs for the 3LSG. The $\varepsilon_{e,A}$,$\varepsilon_{f,A}$ and $\varepsilon_{e,B}$,$\varepsilon_{f,B}$ monomer energies, the J_{AB} and K_{AB} unit couplings and the unit dipoles, $\mu_A, \mu_A^f, \mu_B, \mu_B^f$ are given as lists of inputs to the closed system generator part of the 3LSG, similarly to the example shown in section 4.1, which generate the matrices describing the electronic Hamiltonian of the system, H_{el} and its dipole operator $\boldsymbol{\mu}$ according to the procedure outlined in the previous chapter. The parameters $\nu_A^e, \nu_A^f \nu_B^e, \nu_B^f, \lambda, \Lambda, \Omega, \gamma$ and S, defining the spectral density in Eq. 5.1 are given as inputs to the open system generator part of the 3LSG, along with the inter-manifold relaxation times τ_R and τ_{IC}, which generates the superoperator D describing intra- and inter-manifold relaxation processes, from which the system's Liouvillian $\mathcal{L}_0$ is subsequently generated. Users are free to specify how many dimer pairs they wish to simulate by changing a single parameter. Appendix B shows an example of Python code used to generate the squaraine copolymer systems simulated in this chapter.

This copolymer model generator is used, in conjunction with the UF^2 algorithm (see Appendix B for yet another Python code example of this), to simulate high-order TA spectra on squaraine copolymers to study multi-exciton phenomena, replicating an experimentally observed separation and then collapse of ESA signals at different nonlinear spectroscopy orders while also providing a physically-backed explanation for this phenomenon.

Chapter 6

Conclusion

This thesis presents the development of a set of computational tools capable of automatically generating Hamiltonians or Liouvillians for arbitrary sized polymers made of three-level systems. We have also shown how these generated models can be used to both reproduce and provide explanations of exprimental observations of high-order transient absorption (TA) spectroscopies.

Chapter 4 outlines the new three-level system generator (3LSG), which is now fully integrated in the larger Hamiltonian/Liouvillian Generator (HLG), itself part of the Ultrafast Spectroscopy Suite (UFSS, also outlined in Chapter 4). This chapter presents the inner workings of the 3LSG and what sort of models can be simulated with the generator for both closed systems and open quantum systems. Also showcased in Chapter 4 are examples of Python code used to generate the Hamiltonian of a simple dimer of 3LS for a closed system, and the Liouvillian of an open system which includes relaxation effects.

Chapter 5 describes how the three-level system generator, in conjunction with the spectroscopic calculation algorithm UF^2 (a module of UFSS) for perturbative nonlinear spectroscopies, can be used to reproduce experimental spectra of 3$^{\text{rd}}$- to 13$^{\text{th}}$-order transient absorption spectroscopies for copolymers which are modeled as 3LS. We also use the 3LSG and the copolymer model outlined in Sec. 5.1 to provide a physically motivated explanation for the previously unobserved long-time behaviour of the excited-state absorption (ESA) peaks in the experimental higher-order TA spectra.

Altogether, the three-level system generator represents the most general contribution of this thesis. It can be used together with the available tools of UFSS to study experimental phenomena in nonlinear spectroscopies, as is done in Chapter 5 for the explanation of the ESA peak collapse. Alternatively, the 3LSG can also be used as a standalone tool to generate either the closed system Hamiltonian or the open system Liouvillian of polymers of three-level systems of any size, where the only restriction on the size of the system being simulated is the available memory of the computer used.

Appendix A

We here justify the use of the rotating-wave approximation (RWA) for both closed and open systems calculations in Sec. 3.3. We start with Eq. 3.38 for the perturbed 1$^{\text{st}}$-order wavefunction,

$$|\psi^{(1)}(t)\rangle = \frac{i}{\hbar}U_0(t,0)e^{i(\mathbf{k}_p\cdot\mathbf{r}+\phi_p)}\left(\int_0^\infty A_p(t-t')e^{-i\omega_p(t-t')}U_0^{-1}(t-t',0)\mu|\psi^{(0)}(t-t')\rangle dt'\right) + \frac{i}{\hbar}U_0(t,0)e^{i(\mathbf{k}_p\cdot\mathbf{r}+\phi_p)}\left(\int_0^\infty A_p(t-t')e^{i\omega_p(t-t')}U_0^{-1}(t-t',0)\mu|\psi^{(0)}(t-t')\rangle dt'\right). \tag{6.1}$$

We define the unpertubed wavefunction $|\psi^{(0)}\rangle$ in the system's Hamiltonian (H_0) eigenbasis, which is

$$|\psi^{(0)}\rangle = \sum_i c_i|i\rangle,$$

where $|i\rangle$ are the eigenstates of H_0, with occupation probabilities c_i. The action of the dipole operator μ with elements μ_{ki} on $|\psi^{(0)}\rangle$ is then

$$\begin{aligned}\mu|\psi^{(0)}\rangle &= \mu\sum_i c_i|i\rangle \\ &= \sum_{k,i}\mu_{ki}c_i|i\rangle.\end{aligned}$$

Thus, we have

$$U_0^{-1}(t-t',0)\mu|\psi^{(0)}(t-t')\rangle = \sum_{k,i}\mu_{ki}c_i e^{i(\omega_k-\omega_i)(t-t')}|i\rangle,$$

leading to the first and second term in Eq. 6.1 above to be respectively

$$A_p(t-t')e^{-i\omega_p(t-t')}U_0^{-1}(t-t',0)\mu|\psi^{(0)}(t-t')\rangle = A_j(t-t')\sum_{k,i}\mu_{ki}c_i e^{i(\omega_k-\omega_i-\omega_p)(t-t')}|i\rangle, \tag{6.2}$$

and

$$A_p(t-t')e^{i\omega_p(t-t')}U_0^{-1}(t-t',0)\mu|\psi^{(0)}(t-t')\rangle = A_j(t-t')\sum_{k,i}\mu_{ki}c_i e^{i(\omega_k-\omega_i+\omega_p)(t-t')}|i\rangle. \tag{6.3}$$

Assuming that the optical pulses used have a carrier frequency ω_p similar to the optical gaps of the system under study, which is generally the case, we then have $\omega_p \approx \omega_k - \omega_i$ and therefore $\omega_p - (\omega_k - \omega_i) \approx \omega_s \ll \omega_p$, $\omega_p + (\omega_k - \omega_i) \approx \omega_f \approx 2\omega_p$ and $\omega_s \ll \omega_f$. Equations 6.2 and 6.3 are then respectively well approximated by

$$A_j(t-t') \sum_{k,i} \mu_{ki} c_i e^{i(\omega_k - \omega_i - \omega_p)(t-t')} |i\rangle \approx A_j(t-t') \sum_{k,i} \mu_{ki} c_i e^{i\omega_s (t-t')} |i\rangle,$$

and

$$A_j(t-t') \sum_{k,i} \mu_{ki} c_i e^{i(\omega_k - \omega_i + \omega_p)(t-t')} |i\rangle \approx A_j(t-t') \sum_{k,i} \mu_{ki} c_i e^{i\omega_f (t-t')} |i\rangle.$$

The second term above, which approximates the second integrand in Eq. 6.1, oscillates many more times in the integration region considered than the first term above, which approximates the first integrand of Eq. 6.1. Therefore, the first term contributes significantly to $|\psi^{(1)}(t)\rangle$, while the second term can be safely neglected and we finally obtain

$$|\psi^{(1)}(t)\rangle \approx \frac{i}{\hbar} U_0(t,0) e^{i(\mathbf{k}_p \cdot \mathbf{r} + \phi_p)} \left(\int_0^\infty A_p(t-t') e^{-i\omega_p (t-t')} U_0^{-1}(t-t',0) \mu |\psi^{(0)}(t-t')\rangle dt' \right),$$

which is the result we arrived at for closed systems.

The derivation of RWA for open systems is essentially the same. Starting from the first-order pertubed density matrix

$$|\rho^{(1)}(t)\rangle\rangle = \frac{i}{\hbar} \mathcal{T}_0(t,0) \int_0^\infty \mathcal{T}_0^{-1}(t-t',0) \left(\varepsilon_p(t-t') \left(\mu^K |\rho^{(0)}(t)\rangle\rangle - \mu^B |\rho^{(0)}\rangle\rangle \right) dt' - \varepsilon_p^*(t-t') \left(\mu^K |\rho^{(0)}(t)\rangle\rangle - \mu^B |\rho^{(0)}\rangle\rangle \right) \right) dt',$$

where we define the 0^{th}-order density matrix $|\rho^{(0)}\rangle\rangle$ in the eigenbasis of H_0 as

$$|\rho^{(0)}\rangle\rangle = \sum_i a_i |i\rangle\langle i|$$

with occupation probabilities a_i for each eigenstate $|i\rangle$. We have

$$\mu^K |\rho^{(0)}\rangle\rangle = \sum_{i,k} \mu_{ki} a_i |k\rangle\langle i|,$$

and

$$\mu^B |\rho^{(0)}\rangle\rangle = \sum_{i,k} \mu_{ik} a_i |i\rangle\langle k|.$$

Thus,

$$\mathcal{T}_0^{-1}(t-t',0) \mu^K |\rho^{(0)}(t-t')\rangle\rangle = \sum_{i,k} \mu_{ki} a_i e^{i(\omega_k - \omega_i)(t-t')} |k\rangle\langle i|,$$

and

$$\mathcal{T}_0^{-1}(t-t',0)\mu^B|\rho^{(0)}(t-t')\rangle\rangle = \sum_{i,k}\mu_{ik}a_i e^{i(\omega_i-\omega_k)(t-t')}|i\rangle\langle k|.$$

We then obtain, first considering the rotating terms with a factor of ε_p, and using the full expression for ε_p,

$$A_p(t-t')e^{-i\omega_p(t-t')}\mathcal{T}_0^{-1}(t-t',0)\mu^K|\rho^{(0)}\rangle\rangle = A_j(t-t')\sum_{k,i}\mu_{ki}c_i e^{i(\omega_k-\omega_i-\omega_p)(t-t')}|k\rangle\langle i|,$$

$$A_p(t-t')e^{-i\omega_p(t-t')}\mathcal{T}_0^{-1}(t-t',0)\mu^B|\rho^{(0)}\rangle\rangle = A_j(t-t')\sum_{k,i}\mu_{ki}c_i e^{i(\omega_i-\omega_k-\omega_p)(t-t')}|i\rangle\langle k|.$$

Again, we have that $\omega_p \approx \omega_k - \omega_i$ and therefore, the two equations above can be approximated by

$$A_p(t-t')e^{-i\omega_p(t-t')}\mathcal{T}_0^{-1}(t-t',0)\mu^K|\rho^{(0)}\rangle\rangle \approx A_j(t-t')\sum_{k,i}\mu_{ki}c_i e^{i\omega_s(t-t')}|k\rangle\langle i|,$$

and

$$A_p(t-t')e^{-i\omega_p(t-t')}\mathcal{T}_0^{-1}(t-t',0)\mu^B|\rho^{(0)}\rangle\rangle \approx A_j(t-t')\sum_{k,i}\mu_{ki}c_i e^{i\omega_f(t-t')}|i\rangle\langle k|.$$

The $\varepsilon_p\mu^B|\rho^{(0)}\rangle\rangle$ term in the integral for $|\rho^{(1)}(t)\rangle\rangle$ oscillates at a frequency ω_f much higher than the $\varepsilon_p\mu^K|\rho^{(0)}\rangle\rangle$ term, which oscillates at frequency $\omega_s \ll \omega_f$ and can then be neglected. Inversely, the two counter-rotating terms with factor ε_p^* in the integral can be approximated by

$$A_p(t-t')e^{i\omega_p(t-t')}\mathcal{T}_0^{-1}(t-t',0)\mu^K|\rho^{(0)}\rangle\rangle \approx A_j(t-t')\sum_{k,i}\mu_{ki}c_i e^{i\omega_f(t-t')}|k\rangle\langle i|,$$

and

$$A_p(t-t')e^{i\omega_p(t-t')}\mathcal{T}_0^{-1}(t-t',0)\mu^B|\rho^{(0)}\rangle\rangle \approx A_j(t-t')\sum_{k,i}\mu_{ki}c_i e^{i\omega_s(t-t')}|k\rangle\langle i|,$$

in which case the $\varepsilon_p^*\mu^K|\rho^{(0)}\rangle\rangle$ term can be neglected and the $\varepsilon_p^*\mu^B|\rho^{(0)}\rangle\rangle$ is kept. We finally arrive at our reduced expression for the 1$^{\text{st}}$-order density matrix

$$|\rho^{(1)}(t)\rangle\rangle \approx \frac{i}{\hbar}\mathcal{T}_0(t,0)\int_0^\infty \mathcal{T}_0^{-1}(t-t',0)\left(\varepsilon_p(t-t')\left(\mu^K|\rho^{(0)}\rangle\rangle\right)dt' + \varepsilon_p^*(t-t')\left(\mu^B|\rho^{(0)}\rangle\rangle\right)\right)dt'.$$

Appendix B

Below is an example of Python code used to simulate the squaraine copolymers of the kind seen in Chapter 5. Users are free to specify how many dimer pairs they wish to simulate. Additionally, while the parameters defined in the code are those found in Table 5.1, users are also free to change them as well, should that be desirable.

```
import ufss
def setup_params_folder(params_folder_Pn,num_pairs, maximum_manifold):
        # 2 -> 1 relaxation
        tau_ic = 30
        k_ic = 1/tau_ic
    k_ic = k_ic * 1000 / ev_to_THz / (2*np.pi)  # in eV radians the *1000 factor;
                                                # comes from transforming fs^-1 in THz
    ### Making closed system parameters ###
    os.makedirs(params_folder_Pn,exist_ok=True)
    num_sites = 2*num_pairs # total number of sites
    site_energies = []
    for i in range(num_pairs):
                # site energies e_a and f_a for SQA monomer
                energies_a = [e_a, f_a]
                site_energies.append(energies_a)
                # site energies e_b and f_b for SQB monomer
                energies_b = [e_b, f_b]
                site_energies.append(energies_b)
        J_list = []
                K_list = []
                L_list = []
    for i in range(num_sites):
                for j in range(i+1,num_sites):
```

```
                # there's only coupling of adjacent units ; if i and j differ by more than 1
                # (i.e. if for J_i,j we have j-i>1,)
                        if j-i > 1:
                                J = 0
                                K = 0
                                J_list.append(J)
                                K_list.append(K)
                        else :
                                J = J_AB
                                J_list.append(J)
                                K = K_AB
                                K_list.append(K)
                                L_list.append(0)
        site_couplings = [J_list,K_list,L_list]


        dipoles = np.zeros((num_sites,3,3))
# identical dipoles for all sites
        dipoles[0,0,0] = mu_a
        dipoles[0,1,0] = mu_af
        dipoles[0,2,0] = 0 # 0 -> 2 transition is 0
        dipoles[1,0,0] = mu_b
        dipoles[1,1,0] = mu_bf
        dipoles[1,2,0] = 0 # 0 -> 2 transition is 0
    for i in range(2,num_sites-1,2):
        # dipole operator for SQA unit
        dipoles[i,...] = dipoles[0,...]
        # dipole operator for SQB unit
    dipoles[i+1,...] = dipoles[1,...]
    dipoles_list = dipoles.tolist()

    ### open system parameters ###
    # e -> g relaxation rate
        tau_r = (1710.2 - 69.1*num_pairs) # in ps
    k_r = 1/tau_r  # in ps^-1
```

```
k_r = k_r/ ev_to_THz / (2*np.pi) # in eV radians
kT = 0.025  # assuming room temperature
# site-bath coupling of singly-excited state, A-type monomer
    site_bath_a = {'cutoff_frequency':gamma,
                                'coupling': lam,
                                'temperature':kT,
                                'cutoff_function':'brownian',
                                'S': S,
                                'Gamma' : Gamma,
                                'Omega' : Omega,
                                'nu': nu_a,
                                'spectrum_type':'ohmic'}
# site-bath coupling of singly-excited states, B-type monomer
    site_bath_b = {'cutoff_frequency':gamma,
                                'coupling': lam,
                                'temperature':kT,
                                'cutoff_function':'brownian',
                                'S': S,
                                'Gamma' : Gamma,
                                'Omega' : Omega,
                                'nu': nu_b,
                                'spectrum_type':'ohmic'}
# site-bath coupling of doubly-excited state, A-type monomer
    site_bath2_a = {'cutoff_frequency':gamma,
                                 'coupling':lam ,
                                 'temperature':kT,
                                 'cutoff_function':'brownian',
                                 'S': S,
                                 'Gamma' : Gamma,
                                 'Omega' : Omega,
                                 'nu': nu_af,
                                 'spectrum_type':'ohmic'}
# site-bath coupling of doubly-excited state, B-type monomer
    site_bath2_b = {'cutoff_frequency':gamma,
```

```
                                    'coupling':lam ,
                                        'temperature':kT,
                                        'cutoff_function':'brownian',
                                        'S': S,
                                        'Gamma' : Gamma,
                                        'Omega' : Omega,
                                        'nu': nu_bf,
                                        'spectrum_type':'ohmic'}
# relaxation bath for 1->0 processes
    relax_bath = {'dephasing_rate':0.01,
                'relaxation_rate':k_r,
                                'temperature':kT,
                'spectrum_type':'white-noise'}
# add another relax bath for 2->1 process of white-noise type
relax_bath2 = {'dephasing_rate':0.01,
                'relaxation_rate':k_ic,
                'temperature':kT,
                'spectrum_type':'white-noise'}
Redfield_bath = {'secular':True,
                                'site_bath':[site_bath_a,site_bath_b],
                                 'site_bath_option' : [0,1]*num_pairs,
                                'vibration_bath':site_bath_a,
                                 'site_bath2':[site_bath2_a, site_bath2_b],
                        'site_bath2_option' : [0,1]*num_pairs,
                        'site_internal_conversion_bath':relax_bath,
                       'site_internal_conversion_bath21':relax_bath2}
params_Pn = {'site_energies':site_energies,
                                 'site_couplings':site_couplings,
                        'dipoles':dipoles_list,
                       'bath':Redfield_bath,
                        'maximum_manifold':maximum_manifold,
                      # the following two lines mean no vibrations
                      'truncation_size':1,
                     'vibrations':[]}
```

```
        with open(os.path.join(params_folder_Pn,'simple_params.yaml'),'w+') as new_file:
            yaml.dump(params_Pn,new_file)
    ufss.HLG.run(params_folder_Pn, conserve_memory = True)
        return None
```

With the system generator set up with the above code, we can now use UF^2, the spectroscopic calculation module of UFSS, to perform HOTA spectroscopy calculations. The following code is used to produce panel a) of Fig. 5.5.

```
### Setting units for the simulations
f0 = 8065.54429 # in cm^-1, corresponds to 1 eV
omega0 = 2*np.pi*f0 # in radians-cm^-1
time_unit = 1/omega0 # in cm/rad
time_unit *= 1/(3E10) #in s/rad
time_unit *= 1E15 #in fs/rad
pulse_shape = ufss.efield_shapes.gaussian
c = 1.72338
tau_ic = 30 # in fs #
tau_ic = 30/(time_unit)
tau_ic = 150/(time_unit)
gamma_ic = 1/tau_ic

### Setting P1
params_folder_1 = 'P{}'.format(1, tau_1)
setup_params_folder(params_folder_1,num_pairs = 1, maximum_manifold = 7)
open_calc_folder_1 = os.path.join(params_folder_1,'open')

### Setting pulses
delay_times = np.arange(0,5500,250)/time_unit
center = c highest_order = 13
gamma = 0.03 # T = np.array([1E-6])
T = delay_times.copy()
dt = 1

### Running calculations
ta1 = ufss.signals.TransientAbsorption(open_calc_folder_1,
```

```
                include_linear=True,
                conserve_memory = True)
ta1.set_impulsive_pulses(center)
ta1.set_hightest_order(13)
ta1.set_t(gamma = 0.03,dt=3)
ta1.set_pulse_delays([T])
ta1.calculate_signal_all_delays()
ta1.calc.calculation_time
```

Bibliography

[1] Boyd, R. W. *Nonlinear optics* (Academic press, 2020).

[2] Mukamel, S. *Principles of Nonlinear Optical Spectroscopy*. Oxford Series in Optical and Imaging Sciences (Oxford University Press, Oxford, New York, 1999).

[3] Born, M. & Wolf, E. *Principles of Optics: Electromagnetic Theory of Propagation, Interference and Diffraction of Light* (Cambridge University Press, Cambridge, 1999), 7 edn. URL https://www.cambridge.org/core/books/principles-of-optics/D12868B8AE26B83D6D3C2193E94FFC32.

[4] Bruschi, M., Bolzonello, L., Gallina, F. & Fresch, B. Unifying Nonlinear Response and Incoherent Mixing in Action-2D Electronic Spectroscopy. *The Journal of Physical Chemistry Letters* **14**, 6872–6879 (2023). URL https://doi.org/10.1021/acs.jpclett.3c01670. Publisher: American Chemical Society.

[5] Malý, P. & Mančal, T. Signatures of Exciton Delocalization and Exciton-Exciton Annihilation in Fluorescence-Detected Two-Dimensional Coherent Spectroscopy. *The Journal of Physical Chemistry Letters* **9**, 5654–5659 (2018). URL https://doi.org/10.1021/acs.jpclett.8b02271. Publisher: American Chemical Society.

[6] Kalaee, A. A. S., Damtie, F. & Karki, K. J. Differentiation of True Nonlinear and Incoherent Mixing of Linear Signals in Action-Detected 2D Spectroscopy. *The Journal of Physical Chemistry A* **123**, 4119–4124 (2019). URL https://doi.org/10.1021/acs.jpca.9b01129. Publisher: American Chemical Society.

[7] Rose, P. A. *Algorithms for Efficient Calculation of Nonlinear Optical Spectra: Ultrafast Spectroscopy Suite and its Applications*. Thesis, Université d'Ottawa / University of Ottawa (2022). URL http://ruor.uottawa.ca/handle/10393/43428. Accepted: 2022-03-31T18:54:53Z.

[8] Malý, P. *et al.* From wavelike to sub-diffusive motion: exciton dynamics and interaction in squaraine copolymers of varying length. *Chemical Science* **11**, 456–466 (2020). URL https://pubs.rsc.org/en/content/articlelanding/2020/sc/c9sc04367e. Publisher: The Royal Society of Chemistry.

[9] Garand, E. *et al.* Infrared Spectroscopy of Hydrated Bicarbonate Anion Clusters: $HCO_3^-(H_2O)_{1\text{-}10}$. *Journal of the American Chemical Society* **132**, 849–856 (2010). URL https://pubs.acs.org/doi/10.1021/ja9093132.

[10] Kriete, B. *et al.* Interplay between structural hierarchy and exciton diffusion in artificial light harvesting. *Nature Communications* **10**, 4615 (2019). URL https://www.nature.com/articles/s41467-019-12345-9. Publisher: Nature Publishing Group.

[11] Dostál, J. *et al.* Direct observation of exciton-exciton interactions. *Nature Communications* **9**, 2466 (2018). URL https://www.nature.com/articles/s41467-018-04884-4. Publisher: Nature Publishing Group.

[12] Abbe, E. Beiträge zur Theorie des Mikroskops und der mikroskopischen Wahrnehmung. *Archiv für Mikroskopische Anatomie* **9**, 413–468 (1873). URL http://link.springer.com/10.1007/BF02956173.

[13] Consani, C., Auböck, G., Bräm, O., van Mourik, F. & Chergui, M. A cascade through spin states in the ultrafast haem relaxation of met-myoglobin. *The Journal of Chemical Physics* **140**, 025103 (2014). URL https://doi.org/10.1063/1.4861467.

[14] Narra, S. *et al.* Femtosecond Transient Absorption Spectra and Dynamics of Carrier Relaxation of Tin Perovskites in the Absence and Presence of Additives. *The Journal of Physical Chemistry Letters* **11**, 5699–5704 (2020). URL https://doi.org/10.1021/acs.jpclett.0c01589. Publisher: American Chemical Society.

[15] Yuen-Zhou, J., Krich, J. J., Kassal, I., Johnson, A. S. & Aspuru-Guzik, A. *Ultrafast Spectroscopy: Quantum information and wavepackets* (IOP Publishing, 2014).

[16] Breuer, H.-P. & Petruccione, F. *The Theory of Open Quantum Systems* (Oxford University Press, 2002).

[17] May, V. & Kühn, O. *Charge and Energy Transfer Dynamics in Molecular Systems* (John Wiley & Sons, 2011).

[18] Redfield, A. G. On the Theory of Relaxation Processes. *IBM Journal of Research and Development* **1**, 19–31 (1957). URL http://ieeexplore.ieee.org/lpdocs/epic03/wrapper.htm?arnumber=5392713.

[19] Brüggemann, B. & May, V. Exciton exciton annihilation dynamics in chromophore complexes. II. Intensity dependent transient absorption of the LH2 antenna system. *The Journal of Chemical Physics* **120**, 2325–2336 (2004). URL https://aip.scitation.org/doi/10.1063/1.1637585. Publisher: American Institute of Physics.

[20] Brüggemann, B. & May, V. Exciton exciton annihilation dynamics in chromophore complexes. I. Multiexciton density matrix formulation. *The Journal of Chemical Physics* **118**, 746–759 (2003). URL https://aip.scitation.org/doi/10.1063/1.1523392. Publisher: American Institute of Physics.

[21] Manzano, D. A short introduction to the Lindblad master equation. *AIP Advances* **10**, 025106 (2020). URL https://aip.scitation.org/doi/10.1063/1.5115323. Publisher: American Institute of Physics.

[22] Rose, P. & Krich, J. Efficient numerical method for predicting nonlinear optical spectroscopies of open systems. *The Journal of Chemical Physics* **154** (2020).

[23] Tekavec, P. F., Lott, G. A. & Marcus, A. H. Fluorescence-detected two-dimensional electronic coherence spectroscopy by acousto-optic phase modulation. *The Journal of Chemical Physics* **127**, 214307 (2007). URL https://doi.org/10.1063/1.2800560.

[24] Bakulin, A. A., Silva, C. & Vella, E. Ultrafast Spectroscopy with Photocurrent Detection: Watching Excitonic Optoelectronic Systems at Work. *The Journal of Physical Chemistry Letters* **7**, 250–258 (2016). URL https://doi.org/10.1021/acs.jpclett.5b01955. Publisher: American Chemical Society.

[25] Lüttig, J., Mueller, S., Malý, P., Krich, J. J. & Brixner, T. Higher-Order Multidimensional and Pump-Probe Spectroscopies. *The Journal of Physical Chemistry Letters* **14**, 7556–7573 (2023). URL https://doi.org/10.1021/acs.jpclett.3c01694. Publisher: American Chemical Society.

[26] Lüttig, J. *et al.* High-order pump-probe and high-order two-dimensional electronic spectroscopy on the example of squaraine oligomers. *The Journal of Chemical Physics* **158**, 234201 (2023). URL https://doi.org/10.1063/5.0139090.

[27] Rose, P. & Krich, J. Automatic Feynman diagram generation for nonlinear optical spectroscopies and application to fifth-order spectroscopy with pulse overlaps. *The Journal of Chemical Physics* **154**, 034109 (2021).

[28] Malý, P. *et al.* Separating single- from multi-particle dynamics in nonlinear spectroscopy. *Nature* 1–8 (2023). URL https://www.nature.com/articles/s41586-023-05846-7. Publisher: Nature Publishing Group.

[29] Tan, H.-S. Theory and phase-cycling scheme selection principles of collinear phase coherent multi-dimensional optical spectroscopy. *The Journal of Chemical Physics* **129**, 124501 (2008). URL https://doi.org/10.1063/1.2978381.

[30] Rose, P. & Krich, J. Numerical method for nonlinear optical spectroscopies: Ultrafast ultrafast spectroscopy. *The Journal of Chemical Physics* **150**, 214105 (2019).

[31] Lüttig, J., Brixner, T. & Malý, P. Anisotropy in fifth-order exciton-exciton-interaction two-dimensional spectroscopy. *The Journal of Chemical Physics* **154**, 154202 (2021). URL https://aip.scitation.org/doi/full/10.1063/5.0046894. Publisher: American Institute of Physics.

[32] Süβ, J., Wehner, J., Dostál, J., Brixner, T. & Engel, V. Mapping of exciton-exciton annihilation in a molecular dimer via fifth-order femtosecond two-dimensional spectroscopy. *The Journal of Chemical Physics* **150**, 104304 (2019). URL https://aip.scitation.org/doi/10.1063/1.5086151. Publisher: American Institute of Physics.

[33] Yum, J.-H. *et al.* Efficient Far Red Sensitization of Nanocrystalline TiO2 Films by an Unsymmetrical Squaraine Dye. *Journal of the American Chemical Society* **129**, 10320–10321 (2007). URL https://doi.org/10.1021/ja0731470. Publisher: American Chemical Society.

[34] Park, J. *et al.* Symmetric vs. asymmetric squaraines as photosensitisers in mesoscopic injection solar cells: a structure-property relationship study. *Chemical Communications* **48**, 2782–2784 (2012). URL https://pubs.rsc.org/en/content/articlelanding/2012/cc/c2cc17187b. Publisher: The Royal Society of Chemistry.

[35] Merritt, V. Y. & Hovel, H. J. Organic solar cells of hydroxy squarylium. *Applied Physics Letters* **29**, 414–415 (1976). URL https://aip.scitation.org/doi/10.1063/1.89101. Publisher: American Institute of Physics.

[36] Silvestri, F. *et al.* Efficient Squaraine-Based Solution Processable Bulk-Heterojunction Solar Cells. *Journal of the American Chemical Society* **130**, 17640–17641 (2008). URL https://doi.org/10.1021/ja8067879. Publisher: American Chemical Society.

[37] Bagnis, D. *et al.* Marked Alkyl- vs Alkenyl-Substitutent Effects on Squaraine Dye Solid-State Structure, Carrier Mobility, and Bulk-Heterojunction Solar Cell Efficiency. *Journal of the American Chemical Society* **132**, 4074–4075 (2010). URL https://doi.org/10.1021/ja100520q. Publisher: American Chemical Society.

[38] Mayerhöffer, U. *et al.* Outstanding short-circuit currents in BHJ solar cells based on NIR-absorbing acceptor-substituted squaraines. *Angewandte Chemie (International Ed. in English)* **48**, 8776–8779 (2009).

[39] Deing, K. C., Mayerhöffer, U., Würthner, F. & Meerholz, K. Aggregation-dependent photovoltaic properties of squaraine/PC61BM bulk heterojunctions. *Physical Chemistry Chemical Physics* **14**, 8328–8334 (2012). URL https://pubs.rsc.org/en/content/articlelanding/2012/cp/c2cp40789b. Publisher: The Royal Society of Chemistry.

[40] Collison, C. J. *et al.* Theory and assignment of intermolecular charge transfer states in squaraines and their impact on efficiency in bulk heterojunction solar cells (Presentation Recording). In *Organic Photovoltaics XVI*, vol. 9567, 62–62 (SPIE, 2015). URL https://www.spiedigitallibrary.org/conference-proceedings-of-spie/9567/95670R/Theory-and-assignment-of-intermolecular-charge-transfer-states-in-squaraines/10.1117/12.2188850.full.

[41] Paek, S. *et al.* A dual-functional asymmetric squaraine-based low band gap hole transporting material for efficient perovskite solar cells. *Nanoscale* **8**, 6335–6340 (2016). URL https://pubs.rsc.org/en/content/articlelanding/2016/nr/c5nr05697g. Publisher: The Royal Society of Chemistry.

[42] Xiao, Q. *et al.* A pseudo-two-dimensional conjugated polysquaraine: an efficient p-type polymer semiconductor for organic photovoltaics and perovskite solar cells. *Journal of Materials Chemistry A* **6**, 13644–13651 (2018). URL https://pubs.rsc.org/en/content/articlelanding/2018/ta/c8ta05026k. Publisher: The Royal Society of Chemistry.

[43] Xiao, Q. *et al.* Dopant-Free Squaraine-Based Polymeric Hole-Transporting Materials with Comprehensive Passivation Effects for Efficient All-Inorganic Perovskite Solar Cells. *Angewandte Chemie* **58**, 17724–17730 (2019). URL https://doi.org/10.1002/anie.201907331.

[44] Kim, G.-W., Min, J., Park, T. & Petrozza, A. Defect Passivation through (α-Methylguanido)acetic Acid in Perovskite Solar Cell for High Operational Stability. *ACS Applied Materials & Interfaces* **14**, 20848–20855 (2022). URL https://doi.org/10.1021/acsami.2c00231. Publisher: American Chemical Society.

[45] Sou, K., Chan, L. Y., Arai, S. & Lee, C.-L. K. Highly cooperative fluorescence switching of self-assembled squaraine dye at tunable threshold temperatures using thermosensitive nanovesicles for optical sensing and imaging. *Scientific Reports* **9**, 17991 (2019). URL https://www.nature.com/articles/s41598-019-54418-1. Publisher: Nature Publishing Group.

[46] Sklavounos, A. A., Pefkianakis, E. K., Toubanaki, D. K., Vougioukalakis, G. C. & Calokerinos, A. C. A Squaraine Derivative for Cost-Effective, Quick, and Highly Sensitive Determination of Mercury and Thiols and pH Sensing. *ChemPlusChem* **81**, 913–916 (2016). URL https://onlinelibrary.wiley.com/doi/abs/10.1002/cplu.201600316.

[47] Liu, T. *et al.* Far-Red-Emitting TEG-Substituted Squaraine Dye: Synthesis, Optical Properties, and Selective Detection of Cyanide in Aqueous Solution. *European Journal of Organic Chemistry* **2017**, 3957–3964 (2017). URL https://onlinelibrary.wiley.com/doi/abs/10.1002/ejoc.201700649.

[48] Grande, V. *et al.* Selective parallel G-quadruplex recognition by a NIR-to-NIR two-photon squaraine. *Chemical Science* **9**, 8375–8381 (2018). URL https://pubs.rsc.org/en/content/articlelanding/2018/sc/c8sc02882f. Publisher: Royal Society of Chemistry.

[49] Karpenko, I. A. *et al.* Fluorogenic Squaraine Dimers with Polarity-Sensitive Folding As Bright Far-Red Probes for Background-Free Bioimaging. *Journal of the American Chemical Society* **137**, 405–412 (2015). URL https://doi.org/10.1021/ja5111267. Publisher: American Chemical Society.

[50] Qiao, W. *et al.* Squaraine-based AIEgens for reversible mechanochromism, sensitive and selective hypochlorite detection and photostable far-red fluorescence cell imaging. *Materials Chemistry Frontiers* **4**, 2688–2696 (2020). URL https://pubs.rsc.org/en/content/articlelanding/2020/qm/d0qm00357c. Publisher: The Royal Society of Chemistry.

[51] Saneesh Babu, P. S. *et al.* Bis(3,5-diiodo-2,4,6-trihydroxyphenyl)squaraine photodynamic therapy disrupts redox homeostasis and induce mitochondria-mediated apoptosis in human breast cancer cells. *Scientific reports* **7**, 42126 (2017). URL https://europepmc.org/articles/PMC5294812.

[52] Yao, D. *et al.* Molecular Engineered Squaraine Nanoprobe for NIR-II/Photoacoustic Imaging and Photothermal Therapy of Metastatic Breast Cancer. *ACS Applied Materials & Interfaces* **12**, 4276–4284 (2020). URL https://doi.org/10.1021/acsami.9b20147. Publisher: American Chemical Society.

[53] Sun, P. *et al.* J-Aggregate squaraine nanoparticles with bright NIR-II fluorescence for imaging guided photothermal therapy. *Chemical Communications* **54**, 13395–13398 (2018). URL https://pubs.rsc.org/en/content/articlelanding/2018/cc/c8cc08096h. Publisher: The Royal Society of Chemistry.

[54] Merle I. S. Röhr *et al.* Exciton Dynamics from Strong to Weak Coupling Limit Illustrated on a Series of Squaraine Dimers. *Journal of physical chemistry* **122**, 8082–8093 (2018).

[55] Völker, S. F. *et al.* Singlet-Singlet Exciton Annihilation in an Exciton-Coupled Squaraine-Squaraine Copolymer: A Model toward Hetero-J-Aggregates. *The Journal of Physical Chemistry C* **118**, 17467–17482 (2014). URL https://doi.org/10.1021/jp5055809. Publisher: American Chemical Society.

[56] Hader, K., May, V., Lambert, C. & Engel, V. Identification of effective exciton-exciton annihilation in squaraine-squaraine copolymers. *Physical Chemistry Chemical Physics* **18**, 13368–13374 (2016). URL https://pubs.rsc.org/en/content/articlelanding/2016/cp/c6cp01780k. Publisher: The Royal Society of Chemistry.